Structural and functional properties of a borate efflux transporter from barley

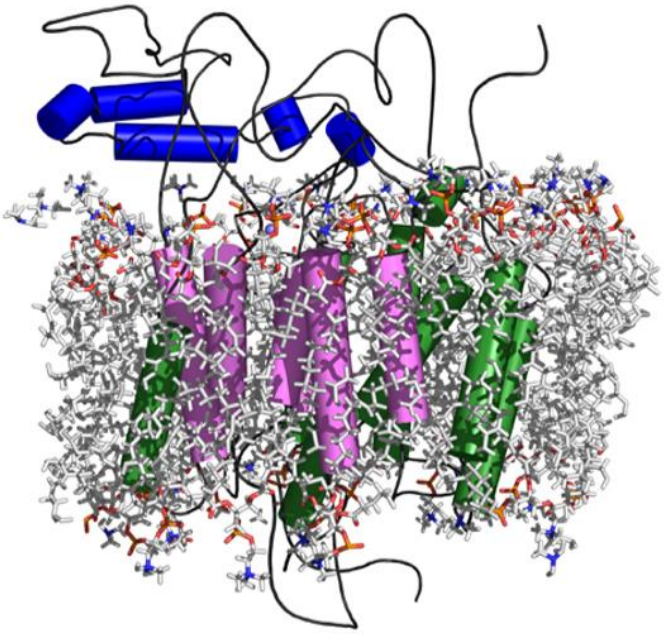

by

Yagnesh Nagarajan

A dissertation submitted to the University of Adelaide in accordance with the requirements of the degree of PhD in the Faculty of Science, School of Agriculture, Food and Wine

May 2015

DECLARATION

I certify that this work contains no material which has been accepted for the award of any other degree or diploma in my name, in any university or other tertiary institution and, to the best of my knowledge and belief, contains no material previously published or written by another person, except where due reference has been made in the text. In addition, I certify that no part of this work will, in the future, be used in a submission in my name, for any other degree or diploma in any university or other tertiary institution without the prior approval of the University of Adelaide and where applicable, any partner institution responsible for the joint-award of this degree.

I give consent to this copy of my thesis when deposited in the University Library, being made available for loan and photocopying, subject to the provisions of the Copyright Act 1968. The author acknowledges that copyright of published works contained within this thesis resides with the copyright holder(s) of those works.

I also give permission for the digital version of my thesis to be made available on the web, via the University's digital research repository, the Library Search and also through web search engines, unless permission has been granted by the University to restrict access for a period of time.

Signed:

Date: 19/12/14

ACKNOWLEDGEMENTS

I am using this opportunity to express my gratitude to everyone who supported me throughout my PhD. I am thankful to my supervisors Professor Maria Hrmova and Dr. Tim Sutton for their aspiring guidance, invaluable constructive criticism and friendly advice throughout my PhD. The monthly meetings throughout my studies really helped and kept me focussed for successful completion. I am sincerely grateful to them for sharing their truthful and illuminating views on a number of issues related to the project.

I would like to specially thank Professor Maria Hrmova for keeping me motivated during stressful times. Her words "It is the journey that counts" really helped me.

I thank my advisors Professor Steve Tyerman and Dr. Matthew Gilliham for their valuable support.

My sincere thanks go to Mr. Nadim Shadiac for his expert technical assistance and advice. A special thanks to all my lab members Pradeep, Shane, Jaeb and Jay and collaborators from University of South Australia and Flinders University for their constant support.

I would like to thank all my friends Amritha, Shyam, Murtaza, Garima, Lenin, Surya, Aniket, Vicky, Ramneet and Mahima for their patience and encouragement.

I would like to thank my fiancé Agalya for her continuous support during stressful times and supporting me throughout the journey.

Finally, I would like to thank all my family members for their support and motivation. I would like to thank my parents for giving me the opportunity to study abroad. My parent's constant prayer in my tough times gave me lot of strength.

My research was financially supported by Australian Centre For Plant Functional Genomics and University of Adelaide.

ABBREVIATIONS

AE	Anion Exchanger
AFM	Atomic Force Microscopy
AQP	Aquaporin
ATP	Adenosine triphosphate
B	Boron element or boron as a shorthand for boron-containing compounds
BA	Boric Acid
BCECF	Biscarboxyfluorescein
BMGY	Buffered glycerol-complex medium
BMMY	Buffered methanol-complex medium
BTP	Bis-Tris Propane
CECF	Continuous-Exchange Cell Free
CF	Cell-Free
cRNA	Capped RNA
Da	Dalton
DIDS	4'-Diisothiocyano-2,2'-stilbenedisulfonic acid
DOPC	Dioleoylphosphocholine
DMPC	1, 2-Dimyristoyl-sn-glycero-3-phosphocholine
EIS	Electrochemical Impedance Spectroscopy
ESI	Electrospray Ionisation
FM	Feeding Mixture
GFP	Green Fluorescent Protein
GUV	Giant Unilamellar Vesicles
IMP	Integral Membrane Protein
MD	Molecular Dynamics
MIP	Major Intrinsic Protein
MP	Membrane Protein
NIP	Nodulin Intrinsic Membrane Protein
NMR	Nuclear Magnetic Resonance
Osmol	Osmolarity
PAGE	Polyacrylamide Gel Electrophoresis
PIP	Plasma Membrane Intrinsic Protein
PCR	Polymerase Chain Reaction

PD	Potential Difference
P_o	Open probability of channel
POPC	1-Palmitoyl-2-oleoyl-s*n*-glycero-3-phosphocholine
POPE	1-Palmitoyl-2-oleoyl-s*n*-glycero-3-phosphoethanolamine
POPG	1-Palmitoyl-2-oleoyl-sn-glycero-3-phospho-1'-rac-glycerol
QTL	Quantitative Trait Locus
RM	Reaction Mixture
SAXS	Small-Angle X-ray Scattering
SDS	Sodium Dodecyl Sulphate
SMA	Styrene Maleic Anhydride
3D	Three-Dimensional
tBLM	tethered Bilayer Lipid Membrane
TEV	Tobacco Etch Virus
TEVC	Two-Electrode Voltage Clamp
TLC	Thin-Layer Chromatography
TIP	Tonoplast Intrinsic Protein
WG	Wheat Germ
WIB	Western Immuno-Blot

TABLE OF CONTENTS

Chapter 1 - Literature review

This chapter is a preface to the following four chapters of the PhD thesis and offers a compilation of available literature. Chapter 1 is sub-divided into three sections pertaining to the role of boron (a shorthand for boron-containing compounds) and known transport mechanisms in plants, plant anion channels, and cell-free synthesis methods for plant protein production.

1.1 Boron

Boron (B) as an element has a complex chemistry. Although it is placed under Group 13 in the Periodic Table of the Elements, the chemical properties of B are very different from other elements of the group, such as aluminium and gallium. B is a metalloid sharing the properties of both metals and non-metals. Two stable isotopes of B exist, with atomic numbers 10 and 11, which occur naturally in a percentage ratio of approximately 20:80, giving an average atomic mass of B of 10.81 (Power and Woods, 1997).

1.2 Boron existence under physiological conditions

B dissolves readily in water to form boric acid (BA), H_3BO_3, which is a weak Lewis acid, accepting OH^- groups at alkaline pH to form the borate ion, $[B(OH)_4]^-$ leaving a proton H^+ in solution (Figure 1).

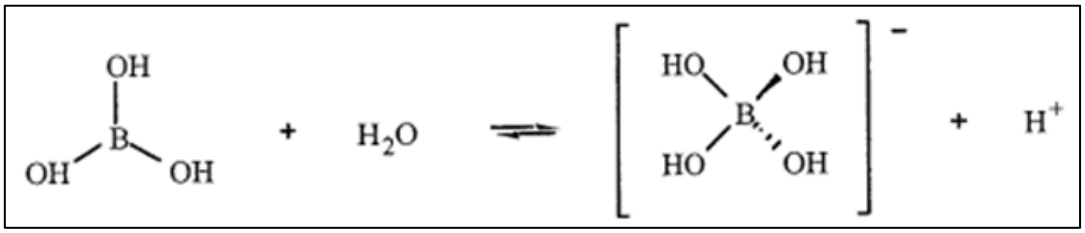

Figure 1. The BA-borate equilibrium (Loomis and Durst, 1992).

B is a planar triangle with bond angles of 120°, whereas the borate ion is tetrahedral with bond angles of 109° (Loomis and Durst, 1992). In dilute solutions, B consists of only H_3BO_3 and $[B(OH)_4]^-$. Since the pKa value of H_3BO_3 in pure water is 9.25 (Dean 1979), the majority of free H_3BO_3 exists in the form of un-dissociated acid, while plants take up readily this form of B.

1.3 B in soil systems

Concentrations of B vary with soil types and in some soils B concentration increases with soil depth (Figure 2). Wetter soils contain low levels of B than dryer soils and factors such as pH, organic matter, rainfall, moisture content and texture, all affect the equilibrium of absorbed and available B (Brennan and Adcock, 2004; Reid and Fitzpatrick, 2009). In Australia, sources of B are derived from marine sediment, tourmaline bearing rock and aeolian material from salt lakes (Power and Woods, 1997). In irrigated soil for crop production, B has a narrow range between deficiency (B content <10 mg of B kg^{-1} of soil) and toxicity (high B content 10–100 mg B kg^{-1} of soil) (Wolf 1974; Power and Woods, 1997). There have been reports of yield penalties in both wheat and barley due to B toxicity (Cartwright et al., 1984; Moody et al., 1993). Therefore crops with tolerance to B are of major economic importance (Jefferies et al., 1999) and selection of B-tolerant varieties is a priority for wheat and barley breeding programs (Paull et al., 1997)

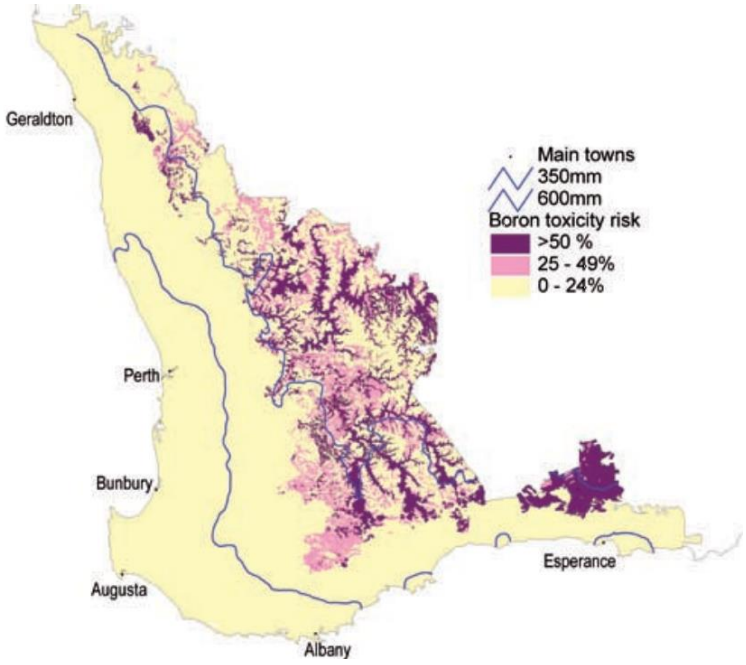

Figure 2. A map showing the proportion of soils at risk of having B-toxic subsoils in Western Australia (Department of Agriculture and Food, Government of Western Australia).

1.4 Physiological role of B

The physiological role of B in plants was first addressed about 90 years ago (Warington, 1923) and is known to be an essential micronutrient in higher plants. The primary role of B in plants is in cell wall and membrane integrity, and complex formation with sugar alcohols

(Nable et al., 1997). B is involved in stabilisation of molecules with *cis*-diol groups, by cross-linking pectic polysaccharides through B-diol bonding of two rhamnogalacturonan (RGII) molecules (Nable et al., 1997). Thus, B cross-linked RG-II complexes (Figure 3) are necessary for the normal growth and development of plants. There are several other processes, in which B is found to be involved. For example, B in the form of BA available to plants influences membrane potential and ion flux across membranes (Blasergrill et al., 1989), and affects levels of cytoskeletal proteins (Yu et al., 2001; Yu et al., 2002), metabolism of phenolics and polyamines (Camacho-Cristobal et al., 2004; Camacho-Cristobal et al., 2005) and nitrogen metabolism (Camacho-Cristobal and Gonzalez-Fontes, 1999; Camacho-Cristobal and Gonzalez-Fontes, 2007). Increasing evidence suggest that B is essential for humans (Nielsen, 2000) and it is also required for specialised nitrogen-fixing cells of prokaryotic cyanobacteria (Bonilla et al., 1990).

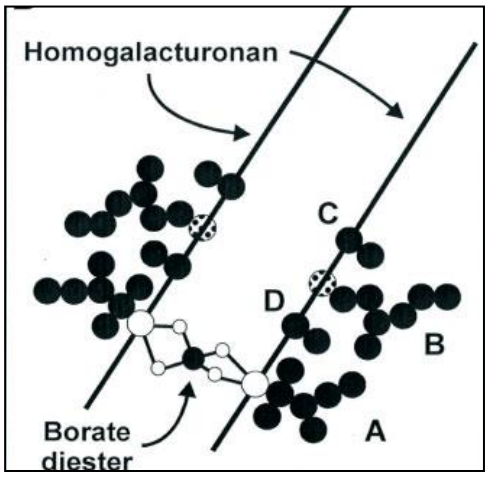

Figure 3. A schematic representation of the B-RGII dimer (Nable et al., 1997).

B-toxicity as well as deficiency, affect growth and metabolism of plants. B-deficiency in vascular plants affects root elongation, carbohydrate metabolism, nucleic acid synthesis and pollen tube growth (Goldbach and Wimmer, 2007). The effects of B-toxicity in plants are described in the following paragraph.

1.4.1 B-toxicity symptoms in plants

The characteristic symptoms of B-toxicity are reduced growth of shoots and roots in affected plants. Typical visible symptoms of B-toxicity are leaf chlorosis and/or necrosis (Roessner et al., 2006), often found at the margins and tips of older leaves creating a concentration gradient, which is the highest at leaf tip and decreasing towards the leaf base (Nable et al.,

1997). These symptoms arise as B becomes immobile, thus accumulating in tips of the oldest leaves (Figure 4). Comparatively, shoots have higher concentration of B than roots (Nable et al., 1997). These visible symptoms reflect the distribution of B in most species, with B accumulating at the end of a transpiration stream. The other effects of B-toxicity includes altered metabolism, reduced root cell division, decreased leaf chlorophyll content and a photosynthetic rate, and decreased levels of lignin and suberin (Nable et al., 1997; Reid, 2007). There is, however no evidence to support the fact that B-toxicity symptoms on leaves are mainly due to an osmotic stress induced by excess of B accumulation (Hayes and Reid, 2004).

Figure 4. A leaf blade of barley affected by B-toxicity (Schnurbusch et al., 2010a). a) B-sensitive variety b) B-tolerant variety.

1.5 Mechanisms of B transport in plants

BA as the major form of B is transported from soil to the roots of plants through two major mechanisms namely, passive diffusion across the plasma membrane and *via* the active transport system through ion transport proteins localised in the plasma membrane.

1.5.1 Passive diffusion of BA

B is the only element taken up as an uncharged BA molecule and not as an ion in plants (Miwa and Fujiwara, 2010). The theoretical permeability coefficient of BA in the plant plasma membranes based on the partition coefficient of BA (0.035) was found to be 8×10^{-6} cm s^{-1} (Raven, 1980). Based on this high theoretical permeability value, which is adequate to satisfy the B requirement of plants, it was proposed that the uptake of BA occurs *via* passive diffusion. However, this calculated value was not verified through experimental methods until direct measurements of membrane permeability of BA were conducted by Dordas and Brown (2000). In their study, the permeability coefficient of BA was determined in artificial systems (liposomes) and mutant lines of *Arabidopsis thaliana*, and was found to vary between 4.9×10^{-6} cm s^{-1} to 9.5×10^{-9} cm s^{-1}, based on four factors namely, membrane sterols

composition, the type of phospholipid head groups, length of fatty acyl chain and the pH of the medium.

1.5.2 Channel mediated BA transport

The permeability coefficient of BA from a squash root experiment (Dordas and Brown, 2001) was determined to be 3.9 x 10^{-7} cm s^{-1}. This low value contradicted the permeability coefficients obtained earlier by the same group (Dordas et al., 2000), suggesting the existence of non-specific channel-mediated diffusion and energy-dependent active transport of BA (Dannel et al., 2000). This has led to research being carried out in the last decade to understand the role of transport proteins involved in BA transport.

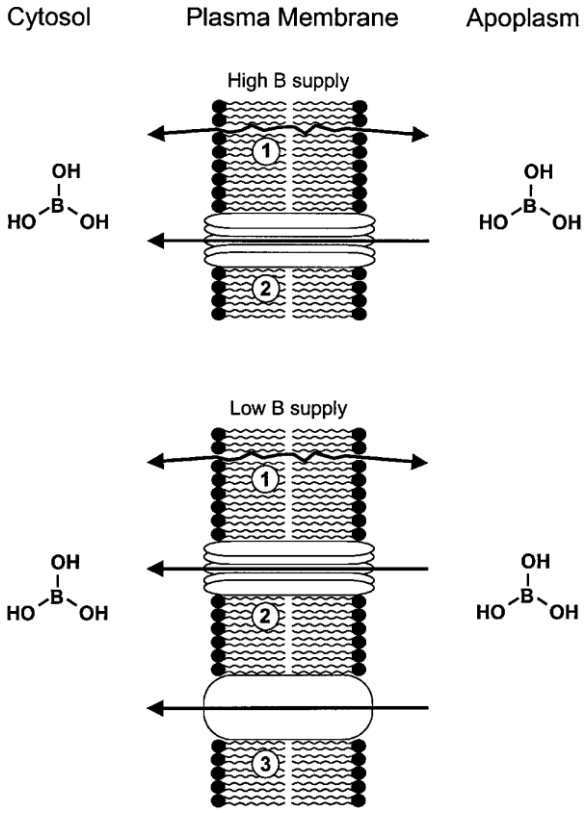

Figure 5. Mechanism of transport through membranes: 1) Passive diffusion of BA across a membrane lipid bilayer; 2) Facilitated permeation of BA through membrane intrinsic proteins (MIPs); 3) BA transport by an energy-dependent high affinity transport system under low B supply (Dannel et al., 2002).

1.5.3 Root uptake and xylem loading of BA under limited BA supply

BA distribution in plants varies widely in different tissues (Nable et al., 1997), indicating that different genes in these tissues mediate BA accumulation and tolerance. Many genes

involved in BA transport have been reported. A summary of BA transport proteins reported in the literature is listed in Table 1.

Genetic studies in *A. thaliana* identified NIP5;1 (Nodulin 26-like Intrinsic Protein) involved in an influx of BA (Takano et al., 2006). The expression of NIP5;1 in *Xenopus laevis* oocytes showed that the protein is localised to the plasma membrane. Reduction in root BA uptake and growth defects under limiting BA in a AtNIP5;1 mutant line along with increased BA uptake in *X. laevis* oocytes expressing AtNIP5;1, suggested that NIP5;1 was necessary for efficient uptake of BA into *A. thaliana* root cells. As shown in Figure 6, under BA-limited conditions, NIP5;1 was found to be up-regulated (Takano et al., 2006), thereby increasing the permeability of BA uptake into roots from soil. The activity of an *Arabidopsis thaliana* borate transporter BOR1, which exports BA out of the cells towards the xylem against the concentration gradient, was also high under BA limitation (Takano et al., 2006). Under high levels of BA supply, the expression of both *NIP5;1* and *BOR1* was down-regulated at transcriptional and post-transcriptional levels, respectively. The BOR1 protein was incorporated into endosomes and transported to the vacuole for degradation (Takano et al., 2006). Another NIP, NIP6;1 which is similar to NIP5;1 was subsequently identified in *A. thaliana* and found to be responsible for a preferential distribution of BA into young developing tissues through a xylem-phloem transfer mechanism (Tanaka et al., 2008).

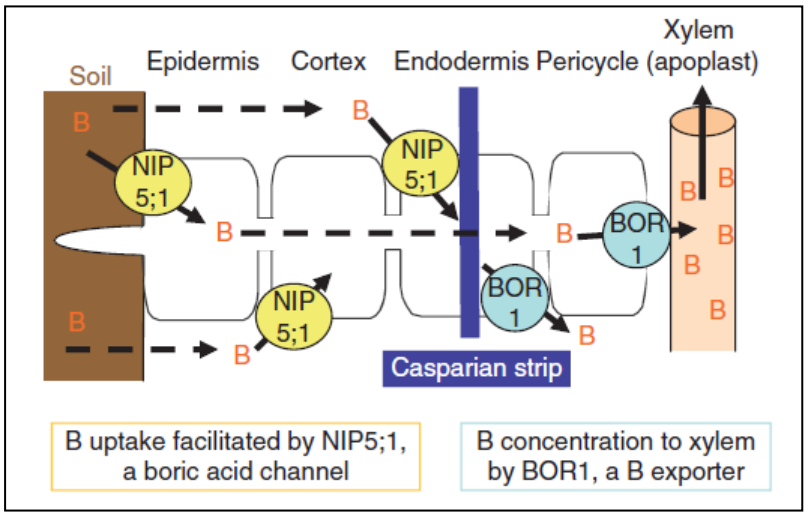

Figure 6. Schematic representation of BA (denoted as B) transport in roots of *A. thaliana* under the limited concentrations of BA (Miwa and Fujiwara, 2010).

Table 1: Summary of known B transporters in plants (Modified from Reid, 2014)

Transporter	Type	Function	Reference
OsBOR1	Effluxer	B transfer from soil to xylem	Nakagawa et al. 2007
OsBOR2	Effluxer	Unknown	Tanaka et al. 2013
OsBOR3	Effluxer	Seed development	Tanaka et al. 2013
OsBOR4	Effluxer	Pollen tube development	Tanaka et al. 2013
OsPIP2;4	Channel	Facilitates B efflux from roots	Kumar et al. 2014
OsPIP2;7		Facilitates B efflux from roots	Kumar et al. 2014
HvBot1	Effluxer or channel	B efflux into the cell wall for development, but may also be advantageous at high B	Reid, 2007 Sutton et al. 2007
HvNIP2;1	Channel	Possibly silicon transporter	Schnurbusch et al. 2010b
HvPIP1;3	Channel	Unknown	Fitzpatrick and Reid 2009
HvPIP1;4	Channel	Unknown	Fitzpatrick and Reid 2009
TaBot-D2a	Effluxer	B efflux into the cell wall for development, but may also be advantageous at high B	Pallotta et al., 2014
TaBot-D4a	Effluxer	Unknown	Pallotta et al., 2014
TaBot-A4a	Effluxer	Unknown	Pallotta et al., 2014
TaBot-B4a	Effluxer	Unknown	Pallotta et al., 2014
ZmPIP1	Channel	Unknown	Dordas and Brown 2001
AtBOR1	Effluxer	Xylem loading under low B conditions	Takano et al. 2002
AtBOR2	Effluxer	Radial B transport in roots. Aids in root cell elongation at low B	Miwa et al. 2013
AtBOR3	Effluxer	Unknown	Miwa et al. 2005
AtBOR4	Effluxer	Efflux of B from root epidermis to soil	Miwa et al. 2007
AtBOR5	Unknown	Unknown	Miwa et al. 2005
AtBOR6 AtBOR7	Unknown	Similar to OsBOR3 and OsBor4	Miwa et al. 2005
AtNIP5;1	Channel	B influx into roots under low B	Takano et al. 2006
AtNIP6;1	Channel	B distribution in shoots	Tanaka et al. 2008
AtTIP5;1	Channel	Increases permeability of tonoplast to B	Pang et al. 2010

1.5.4 BA transport under increased supply of BA

During normal growth and developmental conditions, BA is preferentially distributed to cell walls and during an elevated BA supply, excess BA is solubilised in the cytoplasm (Miwa and Fujiwara, 2010). A decreased BA concentration in roots has been correlated to BA-tolerance. Two genes have been identified in regulating transport of BA. The first is the gene encoding for the HvNIP2;1 protein, which is a member of the aquaporin (AQP) family present on chromosome 6H of barley (Jefferies et al., 1999; Schnurbusch et al., 2010b). The protein is classified as the silicon transporter HvNIP2;1 based on the putative orthologous features similar to OsLsi1 from rice (Chiba et al., 2009). It is expressed on the distal side of the epidermal and cortal cells in roots (Chiba et al., 2009). Heterologous expression of HvNIP2;1 in *S. cerevisiae* and *X. laevis* oocytes showed that the protein facilitates the transport of uncharged molecules such as silicic acid and BA (Schnurbusch et al., 2010b). Furthermore, the reduced expression of HvNIP2;1 was observed under high BA concentrations in soil resulting in a decreased passive intake of BA into roots contributing to lower shoot accumulation and thus offering high BA-tolerance in the barley Sahara variety 3771 (Sahara) (Schnurbusch et al., 2010b).

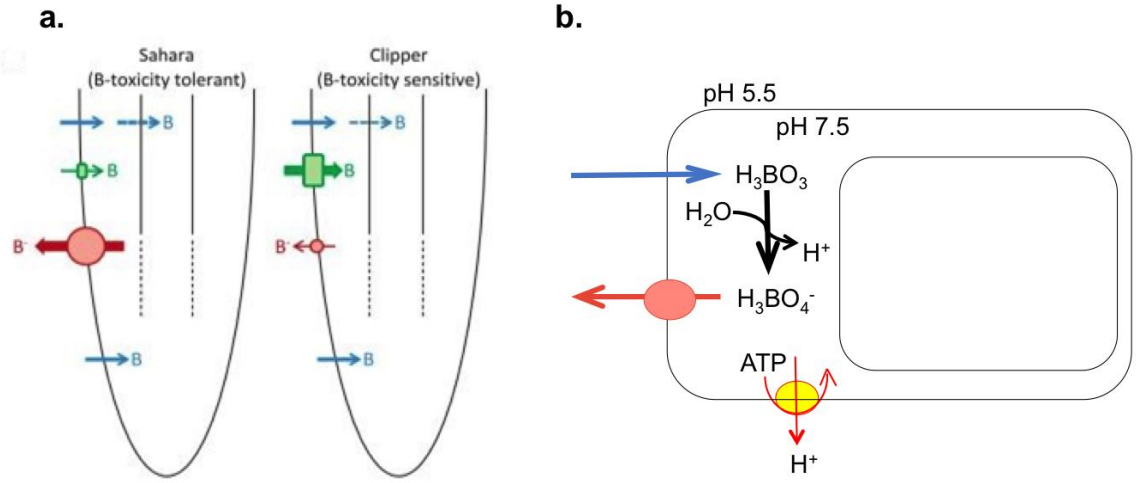

Figure 7. A BA toxicity mechanism. **a**. In a tolerant barley variety (Sahara), toxicity is mediated by reduced expression of *HvNIP2;1* and BA efflux through the HvBot1 protein. In a sensitive barley variety (Clipper), toxicity is mediated by higher expression of *HvNIP2;1* and reduced expression of *HvBot1* genes. **b**. Model of BA efflux in a tolerant barley variety (Schnurbusch et al., 2010a). Blue arrows indicate passive diffusion of B in the form of BA. Green arrows indicates BA uptake through *HvNIP2;1* and red-brown arrows indicate BA efflux through *HvBot1*, where the size of the transporter illustated is related to the level of gene expression . H^+-ATPase maintains the gradient of H^+ influx and borate efflux to prevent

the root membrane from depolarising (red arrows). The pH values of external and internal cellular environments are indicated.

Recently, in barley, variants of HvNIP2;1 with different substrate selectivity have been reported (Hayes et al., 2013). The authors altered the selectivity of the HvNIP2;1 protein by introducing mutations at Gly88Ala and Gly88Cys and found yeast (expressing HvNIP2;1) growth to be restored under high BA and germanic acid concentrations, but not in the presence of an arsenious acid. Additional mutations at Ser207Val and Ala132Thr restored the yeast growth in the presence of arsenious acid (Figure 8).

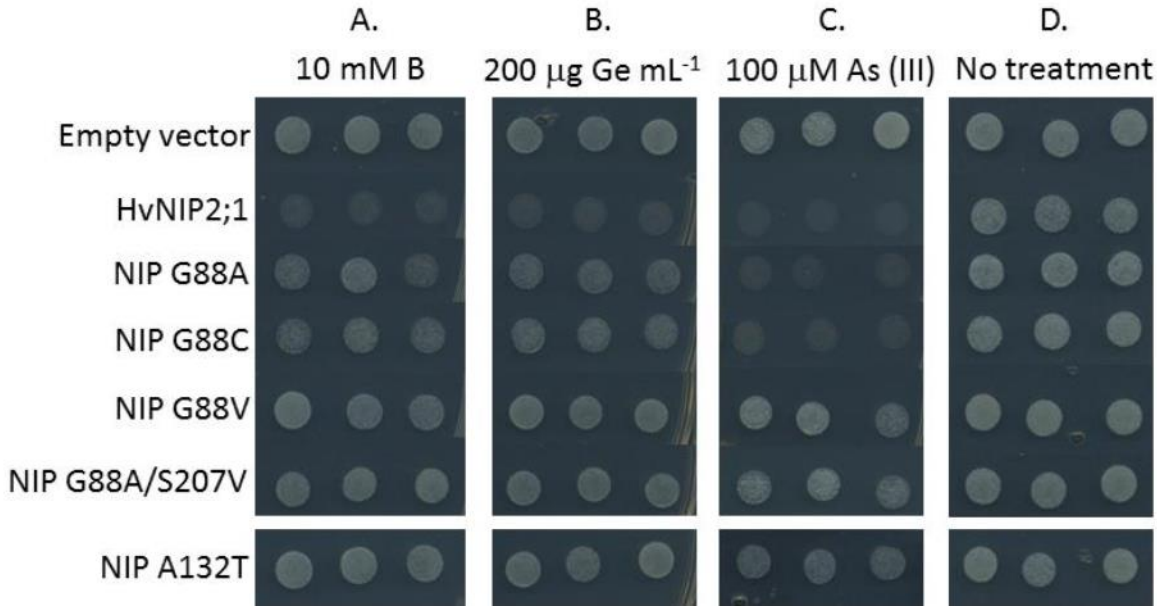

Figure 8. Yeast growth assay in the presence and absence of various concentrations of metalloids. A. BA, B. germanic acid (Ge), C. arsenious (As) acids and D. no metalloids present by wild-type and variant HvNIP2;1 with mutated residues (left-hand side) (Hayes et al., 2013).

The second gene involved in BA-toxicity tolerance in barley is the *Arabidopsis BOR1* ortholog, *HvBot1* that has been identified on 4H chromosome through Quantitative Trait Locus (QTL) mapping of Clipper and Sahara genotypes (Sutton et al., 2007). Genotypic comparison between Clipper and Sahara showed four times as many *Bot1* gene copies located at the tolerant locus in Sahara (Sutton et al., 2007). The increased copy number of the *Bot1* gene was found to be responsible for the increased production of the *Bot1* transcripts that were consistent with the role of regulating the net entry of BA into roots and disposal of

excess BA from leaves through hydathode guttation (Sutton et al., 2007). The ability of Sahara to withstand high BA concentrations was positively correlated with the active efflux of BA from the roots of barley (Reid et al., 2004).

1.6 Borate transporters in wheat

A B transporter, *TaBot-B5b*, related in sequence to *HvBot1* but not the direct orthologue, was identified in the B tolerant bread wheat variety Halberd and mapped to a position under the major 7BL QTL (Schnurbusch et al., 2007). The protein sequence (660 residues) from this wheat variety is 82% identical to that of HvBot1 (666 residues) from barley (Sutton et al., 2007). The *TaBot-B5* gene was identified by a map-based cloning approach in a population derived from a cross between Cranbrook (intolerant) x Halberd (tolerant), exploiting chromosomal gene synteny of wheat 7BL to *Brachypodium* supercontig 1 and rice chromosome 6. A B transporter identical to that of *TaBot-B5b* was found to underlie the 4A QTL in the bread wheat landrace G61450 (Pallotta et al., 2014).

Allelic variants of TaBot-B5b were identified through sequence analysis from a range of tolerant and intolerant cultivars (Pallotta et al., 2014). Based on sequence similarity, the wheat alleles were grouped into four classes, those highly similar to *TaBot-B5b* from Halberd, and to *Bot-B5a* from Chinese Spring, as well as those in which *TaBot* genes were partially (AUS10110b, Kenya Farmer) or completely (Cranbrook) deleted. Further, wheat allelic variants were found to differ in coding region sequences, for example *TaBot-B5b* and *TaBot-B5a* differ by 33 Single Nucleotide Polymorphism sites, resulting in 16 residue differences in the translated protein sequences (Pallotta et al., 2014).

An allelic form of B transporter within the Chinese Spring group was identified (TaBot-B5d) and was found to differ from that of TaBot-B5a by just two amino acid residues at positions 21 and 394. An ethyl methane sulphonate (EMS) mutant of Halberd was also isolated (TaBot-B5b-EMS405) and showed B intolerance (Pallotta et al., 2014). This mutant line contained a substitution at position 215 resulting in a valine residue in place of the wild type alanine. The BA transport activity of the full-length natural allelic variants and the induced EMS mutant was determined through the heterologous expression in *S. cerevisiae* (Figure 8) (Pallotta et al., 2014). A summary of properties of allelic forms and their transport activities point to differences in B transport between allelic forms, which differ by one or two residues

(Table 2). Also noteworthy is the observation that at amino acid residue 394 both TaBot-B5b and TaBot-B5d are identical (Arg), but variant to TaBot-B5a (Lys).

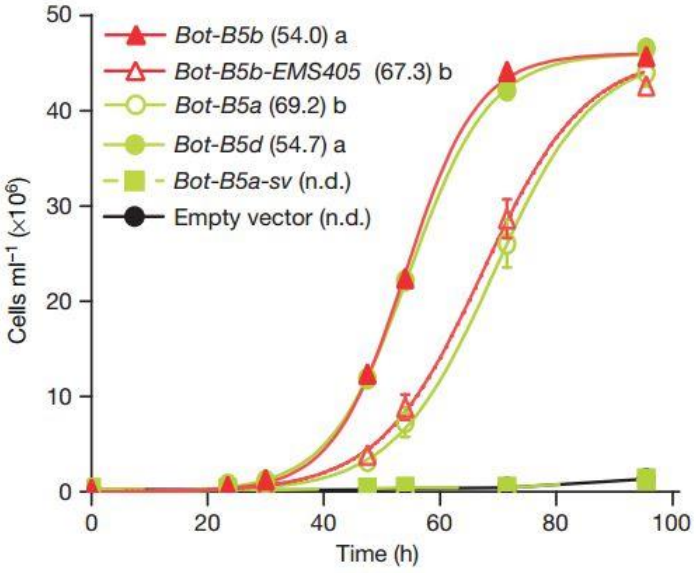

Figure 8. Yeast growth curves of TaBot-B5 variants and control vector in the presence of 15 mM BA . Half saturation life values are given after each yeast strain (Pallotta et al., 2014).

Table 2: Wheat allelic forms, differences in amino acid residues and their B transport activities relative to that of Halberd (Pallotta et al., 2014).

Allelic form	Variety	Chromosome	Differences in amino acid residues	B transport activity
TaBot-B5b	Halberd	7BL		
TaBot-B5a	Chinese spring	7BL	16	Lower than Halberd
TaBot-B5d	G61450	7BL	16	Similar to Halberd, higher than Chinese Spring
TaBot-D5b	SW58	7DL	22	Lower than Halberd
TaBot-B5b-EMS405	EMS mutant of Halberd	7BL	1	Lower than Halberd
TaBot-B5e	AUS30656	7BL	17	B transport not known

1.7 Borate transporters in yeasts and mammals

A putative B transporter designated as a non-specific anion transporter YNL275w, an orthologue of BOR1, was identified in *S. cerevisiae*. This protein was found to be responsible for transport of HCO_3^-, I^-, Br^- , NO_3^- and Cl^- (Zhao and Reithmeier, 2001; Jennings et al., 2007). Knock out studies of Bor1p showed elevated levels of BA in yeast cells confirming that the function of Bor1p is in BA exclusion (Takano et al., 2007). Besides Bor1p, the FPS1 glycerol channel and the DUR3 urea channel were also found to be involved in the transport of BA (Nozawa et al., 2006). Substitutions of specific residues in the FPS1 and DUR3 proteins altered transport of BA.

In animals, a member of SCL4 protein family was found to be responsible for BA homeostasis (Park et al., 2004). In the absence of borate, NABC1 transported Na^+, OH^- (H^+) but in the presence of borate, NABC1 behaved as a conductive electrogenic voltage-regulated Na^+-$[B(OH)_4]^-$ co-transporter (Park et al., 2004).

1.8 Anion channels in plants

Of the different transport systems involved in basic cellular functions in plant and animal cells, anion channels play a key role in many physiological functions including cell osmoregulation, cell signalling, plant nutrition and compartmentalisation of metabolites and metal tolerance (Barbier-Brygoo et al., 2000). In plants, anion channels were reportedly found in the plasma membrane, tonoplast, endoplasmic reticulum, mitochondria and chloroplast. Plasma membrane channels have been the most thoroughly characterised.

1.8.1 How do anion channels work?

Ion channels commonly work through switch mechanisms, which regulate their open and close states according to the factors that control their gating. When an ion channel is open, massive ion fluxes occur based on electrochemical gradients. Rapid development in our understanding of ion channels came into light, when the patch clamping technique was developed by Neher and Sakmann in the late 1970's. The electrophysiological properties of plant cell membranes started being extensively studied even before the genes encoding anion channels were identified. This has been evident from the first anion channel structure being determined only in 2002 (Dutzler et al., 2002).

At the plant membrane level, the highly negative membrane potential (below -100 mV) and the intracellular anion accumulation dictate anion efflux through anion channels, when they are at open states. In cases of carboxylic anions such as malate and citrate, the pH gradient, which is neutral inside and acidic outside, favours efflux of ions through the channels because of the protonation in the extracellular space leading to a steep gradient (Barbier-Brygoo et al., 2000). In tonoplasts, a marginally negative electrical gradient drives efflux of anions from the cytosol to the vascular lumen (Roberts, 2006).

The diversity of anions that need to be transported across plant cell membranes requires that anion channels serve a wide range of functions. Irrespective of anion selectivity, the opening of a channel leads to a shift of membrane electric potential towards an equilibrium potential. This causes depolarisation of a cell membrane. This cell depolarisation can lead to activation of voltage-gated channels or induce signalling events. When anion efflux through anion channels is coupled to potassium efflux, anion channels act as major players in plant cell osmotic regulation. Based on the selectivity, these channels play more specific roles. For example, chloride-selective channels may be involved in salt tolerance (Blumwald, 2000), nitrate-selective channels in nitrogen homeostasis and organic-acid-selective channels in carbon metabolism (Meyer et al., 2010).

Another important aspect of functioning of anion channels other than their selectivity is the mechanism that controls gating. A plant cell membrane cannot survive a constitutively open state as this will lead to a massive loss of ions, causing membrane depolarisation.

1.8.2 Classification of plasma membrane anion channels

Plasma membrane anion channels can be broadly classified into three classes according to their voltage dependence and kinetics: (1) depolarisation-activated anion channels, which mediate either anion efflux (R-rapid and S-slow types) or anion influx (outwardly rectifying type) (Figure 9); (2) hyperpolarisation activated anion channels, which mediate anion efflux and (3) anion channels activated by light or membrane stretch (Roberts, 2006). All these channel types are found mostly in root cells helping in maintenance of anion homeostasis, membrane stabilisation, osmoregulation, BA tolerance, and regulation of passive salt loading into the xylem vessels. Plant roots also have anion channels with unique properties that perform specialised functions. The most notable channels with such specialised function are the organic anion selective channels regulated by extracellular Al^{3+}.

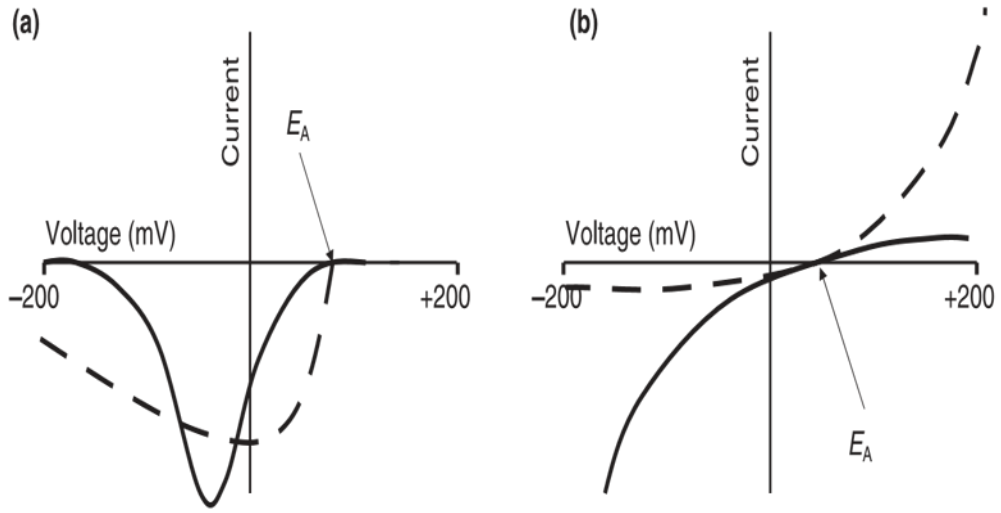

Figure 9. Current-voltage relationships of anion channels. (a) Current-voltage curve for R-type (solid line) and S-type (dashed line). In both R and S types, activation of peak current occurs at negative potentials. However in R-type channels the peak current is more negative resulting in a U- shaped curve compared to S-type channel, where the peak current is more positive. (b) Current-voltage characteristics of outward rectifying depolarised anion channel (dashed line) and inward rectifying hyperpolarised activated anion channel (solid line) (Roberts 2005).

1.8.3 Techniques for studying transport properties of ion channels

There are three major techniques that are widely used for studying ion channels. They are conventional voltage clamp, planar lipid bilayer and vesicle techniques.

1.8.3.1 Voltage clamp

When ion channels pass current, they change their membrane potential difference (PD). This change in PD will affect the currents passing through the channel and also the way ion channels behave. To measure the ion currents and record channel characteristics, the PD has to be kept constant or in an electrophysiological term, it needs to be clamped. The PD can be clamped using an electronic feedback circulatory and the currents passing through the membrane ion channels can be recorded. A central part of the method is the sealing of a cell membrane with a glass pipette. Sealing should be to such an extent that the leak resistance

around the pipette touching the membrane is greater than 1 gigaohm. Neher and Sarkmann (1976) recorded the first single channel currents of the denervated frog muscle fibres.

1.8.3.2 Planar lipid bilayers

The use of artificial lipid bilayers to incorporate ion channels is another way of studying the properties of an ion channel. Two methods can be used to study the channel properties by this technique. The first method is the use of a black lipid membrane, where a lipid bilayer is painted to a small hole between two chambers. The two chambers contain solutions of interest of study and are connected through bath electrodes to a high input impedance voltage clamp amplifier. Purified membrane fractions such as membranes from roots separated by sucrose gradient are introduced into one chamber and these membrane fractions get incorporated to the lipid bilayer. Transport properties of ion channels are then recorded. Some of examples of this technique include the studies of Ca^{2+} channels (Chu et al., 1998; Cannon et al., 2003) and H^{+}-ATPase pumps (Briskin et al., 1995). The second method is the use of a miniaturised patch clamping technique, which is a more advanced version of a conventional patch clamping technique developed by the company Nanion (Kreir et al., 2008). Purified membrane proteins reconstituted into giant unilamellar liposomes are used to form planar bilayers and transport measurements are recorded. The channel activity of a well characterised connexin channel, CX26 has been demonstrated using this technique (Gassmann et al., 2009).

1.8.3.3 Vesicle technique

Passive ion fluxes across vesicle membranes can also be assayed using fluorometric dyes sensitive to particular ions or by using tracers. The membrane potential across the vesicle membrane can be clamped using K^{+}/valinomycin or pH gradients (Allen et al., 1995). This technique is a good screening method to characterise the presence of passive ion transport (Huang et al., 1994).

1.8.4 Ion channel properties and data interpretation

This section focuses on measured properties of ion channels and how these data are interpreted.

The gating of ion channels can be studied by understanding the characteristics of their rectification. Quantification of gating is measured by the proportion of time that the channel spends in an open state. This is known as channel open probability (P_o). The channels may open at various rates and this frequency of open states can also be measured. Ion channel gating can be influenced by four parameters namely: (i) membrane PD, (ii) concentrations of transported ions or molecules involved in intracellular signalling, (iii) protein structural modifications *via* phosphorylation or oxidation *versus* reduction, and (iv) mechanical strain.

1.8.4.1 Interpretation of channel properties

The channel properties can be interpreted based on the features described below.

1.8.4.1.1 Polarities and direction of current flow

Polarities across cellular membranes are assigned on the basis of charge of the cytoplasm with respect to charge on the extracellular side or lumen of any intracellular organelle (Bustamante et al., 1995). The membrane PD across the plasma membrane is generally negative, *i.e.* the cytoplasm has more negative voltage compared to that of the external medium. The direction of current is always referred with respect to that of cytoplasm. Inward current is indicated by a negative sign and represents the current carried by a positive ion when entering the cytoplasm, or a negative ion leaving the cytoplasm. Outward current is indicated by a positive sign and represents the current carried by a negative ion entering the cytoplasm or a positive ion leaving the cytoplasm.

1.8.4.1.2 Rectification

The characteristics of ion channel depend on voltage and concentration of permeating ions leading to influx or efflux of permeating ions. Based on the direction of current, the channels can be classified as outward or inward rectifiers. When the membrane PD across the whole membrane is stepped from a level at which no current flows through the channels to one where channels allow current flow, a time-activation of current occurs (Figure 10). When the voltage is stepped back to membrane PD at which the channel does not pass any current, a transient current, known as tail current, is observed which decays over time. This phenomenon is called deactivation. It is also possible for ion channels to activate first after a change in membrane PD and then to turn off over time in spite of the membrane PD being constant. This phenomenon is called as inactivation and is observed mainly in fast guard cell anion channels (Schroeder and Keller, 1992). There are also channels that are not gated by

voltage, meaning that Po may remain constant for a large range in membrane PD. When the membrane PD is stepped to a new value the flow of current through these channels shows no time-dependence. The currents through these channels are often termed as `leaks'. The rectification properties and the shape of the current *versus* voltage curve can be used to determine the number of ions that can simultaneously occupy the pore, and the position of energy wells and barriers relative to the voltage gradient (White and Ridout, 1995).

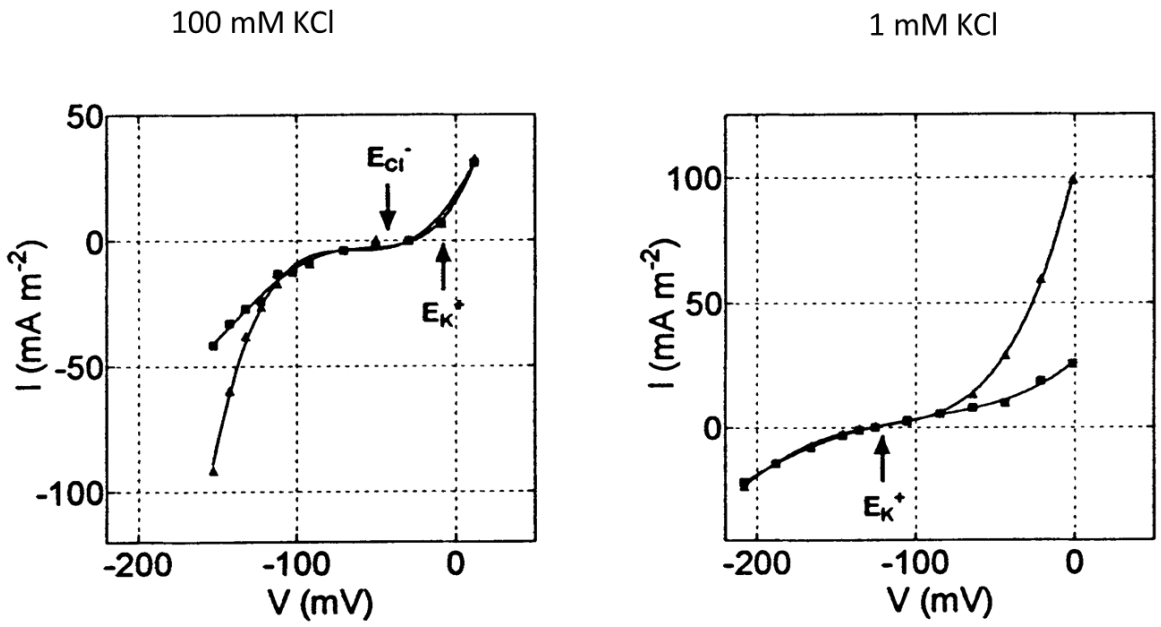

Figure 10. Inward rectifiers of the KIRC potassium channel (Tyerman et al., 1997). At high external 100 mM KCl concentration, a clear inward current is observed due to the inward rectifier property of the channel. When the external concentration is reduced to 1 mM KCl, a clear outward current is observed due to the outward rectifier property of the channel.

1.8.4.1.3 Current *versus* voltage curves

The amplitude of the open channel plotted as a function of voltage will provide details of the permeation properties of a single channel. The membrane PD, at which the direction of current flow through the channel changes direction, is called the reversal potential. The reversal potential will change with changes in the ion concentration gradients, depending on the relative permeability of a channel that permeates different ions.

1.8.4.1.4 Selectivity

The selectivity of a channel can be determined by measuring the relative magnitudes of currents with different ions or by comparing the reversal potential with different ions (White and Ridout, 1995). However the selectivity determined by either method may not be similar. This is because a channel may show high relative permeability for a particular ion but the rate of transport of that particular ion may be much lower than for other ions. This discrepancy occurs if an ion binds to specific sites within the channel during movement. This binding may result in a high relative permeability to that ion but reduced mobility of the ion through the channel.

1.9 Difficulties to study membrane transport proteins

Integral membrane proteins (IMP), such as transport proteins, receptors and membrane enzymes, represent approximately 30% of proteins in fully sequenced proteomes, but there has been an enormous delay in our understanding of structure and function relationships when compared to those of soluble proteins (Hrmova and Fincher, 2009). There are many reasons for such a lack of knowledge. The first is a relatively low natural abundance of membrane proteins available to isolate and purify for functional and structural studies. Secondly, overexpression of membrane proteins *in vivo* in heterologous expression systems, such as in *E. coli* or in yeasts (*P. pastoris* and *S. cerevisiae*) often results in low yields due to issues of cytotoxicity, aggregation or mis-folding. Another issue is related to the complex and dynamic lipid bilayer surrounding of membrane proteins, which causes complications in protein purification and subsequently limits the use of standard biophysical techniques such as Nuclear Magnetic Resonance (NMR) spectroscopy, X-ray crystallography and cryo-electron microscopy. Finally, the hydrophobic nature of membrane proteins requires appropriate native or synthetic hydrophobic environments, *e.g.* micellar or liposomal environments, to maintain membrane proteins' stability and function, once they are extracted from cellular membranes.

1.10 Cell-free synthesis as a tool for studying membrane proteins

Cell-free (CF) synthesis production systems have recently emerged as efficient and robust tools for the production of complex IMPs (Farrokhi et al., 2009; Hovijitra et al., 2009; Periasamy et al., 2013; Shadiac et al., 2013). In this system, the entire process of protein production surrounding the transcription and translation steps takes place *in vitro* (Shadiac et al., 2013). The open nature of the system allows supplementation of target-specific additives

such as stabilisers, chaperones and any other compounds at any time point of the reaction (Schwarz et al., 2008). This system also overcomes cytotoxicity problems associated with cell-based systems (Shadiac et al., 2013). Also, the ability to embed IMPs directly into artificial hydrophobic environments such as surfactants, liposomes and nanodiscs often eliminates the need for reconstitution of IMPs into lipid environments after purification (Shadiac et al., 2013). All these advantages make the CF synthesis system unique in comparison to other cell-based systems. During past twenty or so years, different extract sources have been established and various system configurations and expression modes have been developed (Katzen et al., 2008; Schwarz et al., 2008).

Three well-defined sources of CF synthesis extracts are the extracts from *E. coli*, wheat germ (WG) embryos and rabbit reticulocytes (Whittaker, 2013). The crude lysates from these extracts contain macromolecular components for transcription, translation, protein folding, and energy metabolism, *e.g.* ribosomes, aminoacyl-tRNA synthetases, translation initiation and elongation factors, ribosome release factors, nucleotide recycling enzymes, metabolic enzymes, chaperones, foldases, *etc*. Activated catalysts within the cell lysate act as a chemical factory to synthesise and fold desired protein products upon incubation with essential substrates, which include amino acids, nucleotides, DNA or mRNA template encoding the target protein, energy substrates, cofactors, and salts. After initiation of CF protein synthesis, production continues until one of the substrates (*e.g.* ATP, amino acid, *etc.*) is depleted or by-product accumulation (*e.g.* inorganic phosphate) reaches an inhibitory concentration.

1.10.1 Different modes of CF system

Three major CF reaction modes are commonly used and include a batch mode, a continuous-exchange (CECF) configuration mode and a bilayer mode. Batch systems contain only one compartment and all reaction components are added to the CF system along with the DNA or RNA templates, depending on the type of the extract used. Batch systems are useful for analytical purposes, as reactions can be carried out in micro-plates with reaction volumes of just a few microliters. The disadvantage of this configuration is a limited reaction time, as essential precursors for translation are exhausted or by-products reach inhibitory concentrations. With the second CECF system, high levels up to milligrams of membrane proteins can be obtained. Here, the reaction is divided into two compartments holding a reaction mixture (RM) and a separate feeding mixture (FM). The two compartments are

separated by a semi-permeable membrane with a molecular cut off of 10-50 kDa. The RM contains all the high molecular mass components like the CF extract, nucleic acids and enzymes. The FM contains all the low molecular mass compounds like amino acids, nucleotides and an energy source. Efficient exchange between the two compartments is achieved through shaking or stirring, and reaction time is significantly increased due to continuous supply of precursors from the FM to RM, and removal of low molecular mass inhibitory by-products from the RM. However, the setup and handling of CECF system is relatively complicated and makes it less suited for high throughput applications.

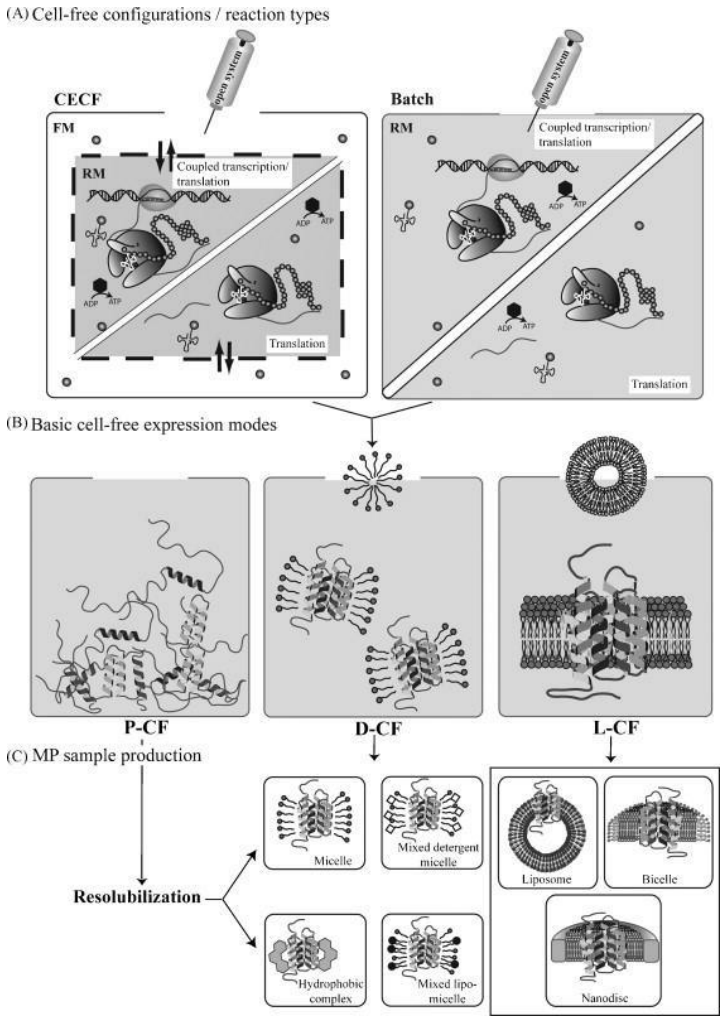

Figure 11. Modes of CF systems. (A) CF reaction configurations (CECF or batch) shown in the two types of reaction systems: coupled transcription/translation and translation only. (B) Different modes of CF expression system. The protein is either expressed without any hydrophobic environments as a precipitate and later reconstituted (P-CF mode), or in the

presence of detergents (D-CF mode) or lipids (L-CF). (C) Range of hydrophobic environments for membrane proteins (Junge et al., 2011).

A third mode, namely the bilayer mode, was proposed (Sawasaki et al., 2002) as an interesting alternative to both approaches mentioned previously. It is a simplified version of the CECF system, where RM is carefully overlaid over FM without separation by a membrane. The reaction is typically set up in micro-plates. Substances between the two layers exchange by simple diffusion and the system was found to be -10-fold more efficient, when compared to batch-mode reactions, yielding sub-milligram amounts of proteins that could be sufficient for structural and functional analyses.

1.11 Aims of the PhD project

The overall aim of this PhD project is to characterise a borate transporter HvBot1from barley *in vitro* and to describe its structural and functional properties to better understand its transport specificity and mechanism.

1.11.1 Specific goals of the PhD project are:

1. To produce recombinant HvBot1 protein through CF synthesis based on wheat-germ and to reconstitute HvBot1 into membrane-mimicking environments in a functionally active form.

2. To perform functional studies of HvBot1 by:
    i) Miniaturised patch clamping using artificial bilayers
    ii) Fluorescent-based stopped-flow light scattering spectrophotometry
    iii) Electrochemical impedance spectroscopy (EIS)

3. To carry out biophysical studies of HvBot1 using small angle x-ray scattering (SAXS) and atomic force microscopy (AFM) to characterise morphological and structural properties of HvBot1.

4. Reconcile the structural and functional properties of HvBot1 and compare them with the current state of knowledge.

1.11.2 Integration of Chapters 1-5 and their relevance to the topic of the PhD thesis

Three chapters (Chapters 2-4) of this PhD thesis are presented in a publication format, while the last chapter (Chapter 5) is written in a text format, as it is being prepared for publication. Two chapters (Chapter 2 and 4) have been published in peer reviewed journals. Chapter 2 was published in the journal *Biophysical and Biochemical Acta - Biomembranes* (Periasamy et al., 2013) and this Chapter describes CF synthesis of an integral membrane enzyme curdlan synthase (CrdS), which serves as a model IMP. The techniques that were developed in this project were utilised for the study of a barley borate transport protein HvBot1, which forms the basis of Chapter 3. Chapter 3 comprises of characterisation of CF-synthesised HvBot1 and provides an insight into the essential structural and functional transport properties of this plant transport protein. Chapter 4 has been published as a review in the journal *Molecular Membrane Biology* (Shadiac et al., 2013) and provides an overview of CF synthesis and a

variety of nanotechnology tools that can be utilised for mechanistic functional studies of membrane proteins. Chapter 5 presents the novel Electro-chemical Impedance Spectroscopy (EIS) data recorded for the HvBot1 protein prepared through *in situ* CF synthesis in a tethered lipid bilayer membrane (tBLM). This study represents a significant advancement in the field of nanotechnology as it facilitates the detailed studies of biologically relevant membrane proteins.

Chapter 2

CELL-FREE PROTEIN SYNTHESIS OF MEMBRANE (1,3)-B-D-GLUCAN (CURDLAN) SYNTHASE: CO-TRANSLATIONAL INSERTION IN LIPOSOMES AND RECONSTITUTION IN NANODISCS

Authors: Agalya Periasamy, Nadim Shadiac, Amritha Amalraj, Soňa Garajová, Yagnesh Nagarajan, Shane Waters, Haydyn D.T. Mertens, Maria Hrmova

NUMBER OF CITATIONS: 13 (as of 19/12/14)

Abstract

A membrane-embedded curdlan synthase (CrdS) from *Agrobacterium* is believed to catalyse a repetitive addition of glucosyl residues from UDP-glucose to produce the (1,3)-β-D-glucan (curdlan) polymer. We report wheat germ cell-free protein synthesis (WG-CFPS) of full-length CrdS containing a 6xHis affinity tag and either Factor Xa or Tobacco Etch Virus proteolytic sites, using a variety of hydrophobic membrane-mimicking environments. Full-length CrdS was synthesised with no variations in primary structure, following analysis of tryptic fragments by MALDI-TOF/TOF Mass Spectrometry. Preparative scale WG-CFPS in dialysis mode with Brij-58 yielded CrdS in mg/ml quantities. Analysis of structural and functional properties of CrdS during protein synthesis showed that CrdS was co translationally inserted in DMPC liposomes during WG-CFPS, and these liposomes could be purified in a single step by density gradient floatation. Incorporated CrdS exhibited a random orientation topology. Following affinity purification of CrdS, the protein was reconstituted in nanodiscs with *Escherichia coli* lipids or POPC and a membrane scaffold protein MSP1E3D1. CrdS nanodiscs were characterised by small-angle X-ray scattering using synchrotron radiation and the data obtained were consistent with insertion of CrdS into bilayers. We found CrdS synthesised in the presence of the Ac-AAAAAAD surfactant peptide or co-translationally inserted in liposomes made from *E. coli* lipids to be catalytically competent. Conversely, CrdS synthesised with only Brij-58 was inactive. Our findings pave the way for future structural studies of this industrially important catalytic membrane protein.

SIGNIFICANCE OF THE FINDINGS

This study demonstrated CF synthesis of a full-length CrdS integral membrane protein using WG-CFS, where the protein was co-translationally inserted into defined membrane mimicking environments such as detergent micelles, liposomes and nanodiscs. Avenues were developed to purify and characterise this protein, both functionally and structurally. The study revealed the importance of screening a variety of lipidic environments to obtain a functionally active membrane catalytic protein.

Statement of Authorship

Title of the paper	Cell-free protein synthesis of membrane (1,3)-β-D-glucan (curdlan) synthase: co-translational insertion in liposomes and reconstitution in nanodiscs
Publication status	Published
Publication Details	Periasamy, A., Shadiac, N., Amalraj, A., Garajová, S., Nagarajan, Y., Waters, S., Mertens, H.D.T., and Hrmova, M. (2013). Cell-free protein synthesis of membrane (1,3)-β-D-glucan (curdlan) synthase: Co-translational insertion in liposomes and reconstitution in nanodiscs. Biochimica et Biophysica Acta (BBA) - Biomembranes 1828, 743-757

Authors Contribution

By signing the Statement of Authorship, each author certifies that their stated contribution to the publication is accurate and that permission is granted for the publication to be included in the candidate's thesis

Name of Principal Author (Candidate)	Agalya Periasamy		
Contribution to the paper	Designed, performed and analysed experiments		
Signature		Date	18/12/14

Name of Co-Author	Nadim Shadiac		
Contribution to the paper	Designed, performed and analysed experiments		
Signature		Date	18/12/14

Name of Co-Author	Yagnesh Nagarajan		
Contribution to the paper	Performed and analysed experiments		
Signature		Date	18/12/14

Name of Co-Author	Amritha Amalraj		
Contribution to the paper	Assisted with experiments		
Signature		Date	18/12/14

Name of Co-Author	Soňa Garajová		
Contribution to the paper			
Signature		Date	18/12/14

Name of Co-Author	Shane Waters
Contribution to the paper	Assisted with experiments
Signature	Date 18.12.14

Name of Co-Author	Haydyn Mertens
Contribution to the paper	Designed, performed and analysed SAXS experiments
Signature	Date 18/12/14

Name of Co-Author	Maria Hrmova
Contribution to the paper	Designed, analysed and wrote paper
Signature	Date 18-12-2014

Biochimica et Biophysica Acta 1828 (2013) 743–757

Contents lists available at SciVerse ScienceDirect

Biochimica et Biophysica Acta

journal homepage: www.elsevier.com/locate/bbamem

Cell-free protein synthesis of membrane (1,3)-β-D-glucan (curdlan) synthase: Co-translational insertion in liposomes and reconstitution in nanodiscs

Agalya Periasamy [a,1], Nadim Shadiac [a,1], Amritha Amalraj [a], Soňa Garajová [a,2], Yagnesh Nagarajan [a], Shane Waters [a], Haydyn D.T. Mertens [b], Maria Hrmova [a,*]

[a] Australian Centre for Plant Functional Genomics, School of Agriculture, Food and Wine, University of Adelaide, Waite Campus, Australia
[b] Australian Synchrotron, SAXS/WAXS Beamline, 800 Blackburn Road, Victoria, Australia

ARTICLE INFO

Article history:
Received 28 April 2012
Received in revised form 25 September 2012
Accepted 4 October 2012
Available online 12 October 2012

Keywords:
Family GT2 transferase
Small-angle X-ray scattering
Surfactant
Surfactant peptide
Topology
(1,3)-β-D-Glucan

ABSTRACT

A membrane-embedded curdlan synthase (CrdS) from *Agrobacterium* is believed to catalyse a repetitive addition of glucosyl residues from UDP-glucose to produce the (1,3)-β-D-glucan (curdlan) polymer. We report wheat germ cell-free protein synthesis (WG-CFPS) of full-length CrdS containing a 6xHis affinity tag and either Factor Xa or Tobacco Etch Virus proteolytic sites, using a variety of hydrophobic membrane-mimicking environments. Full-length CrdS was synthesised with no variations in primary structure, following analysis of tryptic fragments by MALDI-TOF/TOF Mass Spectrometry. Preparative scale WG-CFPS in dialysis mode with Brij-58 yielded CrdS in mg/ml quantities. Analysis of structural and functional properties of CrdS during protein synthesis showed that CrdS was co-translationally inserted in DMPC liposomes during WG-CFPS, and these liposomes could be purified in a single step by density gradient floatation. Incorporated CrdS exhibited a random orientation topology. Following affinity purification of CrdS, the protein was reconstituted in nanodiscs with *Escherichia coli* lipids or POPC and a membrane scaffold protein MSP1E3D1. CrdS nanodiscs were characterised by small-angle X-ray scattering using synchrotron radiation and the data obtained were consistent with insertion of CrdS into bilayers. We found CrdS synthesised in the presence of the Ac-AAAAAAD surfactant peptide or co-translationally inserted in liposomes made from *E. coli* lipids to be catalytically competent. Conversely, CrdS synthesised with only Brij-58 was inactive. Our findings pave the way for future structural studies of this industrially important catalytic membrane protein.

1. Introduction

The bacterial (1,3)-β-D-glucan, also known as curdlan, is an extracellular polysaccharide that is important for cell structure and physiology of prokaryotic *Agrobacterium* sp. [1]. Curdlan has extensive practical and commercial applications in food, cosmetic, pharmaceutical and building industries as previously outlined [1–3]. However, despite the obvious significance of curdlan, the molecular mechanisms that underlie its biosynthesis have not been described at the molecular levels [2,3].

The molecular genetics of curdlan production by *Agrobacterium* sp. has been extensively studied [1–3]. Curdlan synthases (CrdS) [UDP-glucose: (1,3)-β-D-glucan 3-β-D-glucosyltransferase; EC 2.4.1.34] are confined within cell membranes. Based on the sequence homology with other

Abbreviations: β-OG, *n*-octyl-β-D-glucopyranoside; Brij-58, polyoxyethylene-(20)-cetyl-ether (C16/20); CAZy, Carbohydrate-Active enZymes; CF, cell-free; CFPS, cell-free protein synthesis; CHAPS, 3-[(3-cholamidopropyl)dimethylammonio]-1-propansulfonate; CM, catalytic module; CMC, critical micellar concentration; CrdS, curdlan synthase; DDM, *n*-dodecyl-β-D-maltoside; DM, *n*-decyl-β-D-maltoside; DMPC, 1,2-dimyristoyl-*sn*-glycero-3-phosphocholine; DOPC, 1,2-dioleoyl-*sn*-glycero-3-phosphocholine; DOPG, 1,2-dioleoyl-*sn*-glycero-3-phospho-(1′-*rac*-glycerol); DOTAP, 1,2-dioleoyl-3-trimethylammonium-propane; DTT, dithiothreitol; EC, Enzyme Commission; EDTA, ethylenediaminetetraacetic acid; GT, glycoside transferase(s); IMAC, Immobilized Metal Affinity Chromatography; IFT, indirect Fourier transformation; MALDI-TOF, Matrix-Assisted Laser Desorption Ionization-Time of Flight; MS, Mass Spectrometry (spectra); M_r, relative molecular mass; MSP, membrane scaffold protein; NP 40, nonylphenyl-polyethylene-glycol; PDB, Protein Data Bank; POPC, 1-palmitoyl-2-oleoyl-*sn*-glycero-3-phosphocholine; POPE, 1-palmitoyl-2-oleoyl-*sn*-glycero-3-phosphoethanolamine; PVDF, polyvinylidene fluoride; SAXS, small-angle X-ray scattering; SDS-PAGE, sodium dodecyl sulphate-polyacrylamide gel electrophoresis; SEC, size-exclusion chromatography; SMA, styrene maleic acid; SUMO, small ubiquitin-related modifier; TBS, Tris buffer containing NaCl; Triton X-100, polyethylene-glycol-p-1,1,3,3-tetramethyl-butylphenyl-ether; Tween 80, polyoxyethylene-sorbitan-monolaurate 80; TEM, transmission electron microscopy; TEV, Tobacco Etch Virus; UDP-glucose, uridine-diphosphate glucose; WG-CFPS, wheat germ cell-free protein synthesis; YPD, yeast extract-peptone-dextrose; 3D, three-dimensional

* Corresponding author at: Australian Centre for Plant Functional Genomics, School of Agriculture, Food and Wine, University of Adelaide, Waite Campus, Glen Osmond, SA 5064, Australia. Tel.: +61 8 8313 7160; fax: +61 8 8313 7102.
E-mail address: maria.hrmova@adelaide.edu.au (M. Hrmova).

[1] These two authors have contributed equally to this work.
[2] Permanent address: Institute of Chemistry, Centre for Glycomics, Slovak Academy of Sciences, Slovak Republic.

0005-2736/$ – see front matter © 2012 Elsevier B.V. All rights reserved.
http://dx.doi.org/10.1016/j.bbamem.2012.10.003

β-glucan synthases, namely plant cellulose synthases, the CrdS enzyme has been classified by CAZy in the GT2 family of glycosyl transferases [3,4]. The cDNA of CrdS from *Agrobacterium* sp. [1] translates into a protein of 654 amino acid residues. Bioinformatics evaluations predict that CrdS has a N_{out}–C_{in} topology, harbours seven membrane spanning α-helices and contains a single large cytoplasmic region inserted between the 3rd and 4th membrane α-helices [2], representing a putative catalytic module (CM). CM contains characteristic catalytic and substrate binding signatures Asp, Asp, Asp (D, D, D) and GlnxxArgTrp (QxxRW) found in other glucosyltransferases classified in the GT2 family [1–4]. CrdS is predicted to contain at least one pair of bonded cysteines located in CM, although the existence of this disulphide bridge is not supported by experimental evidence [2]. The 3D structures of the GT2 enzymes elucidated by X-ray crystallography comprise a soluble bacterial spore-coat protein [5], a chondroitin polymerase enzyme from *Escherichia coli* [6] involved in synthesis of chondroitin sulfate, a putative glycosyltransferase from *Bacteroides fragilis* [Protein Data Bank (PDB) accession 3BCV, Polani, Kumaran, Burley and Swaminathan, unpublished data] and a recently determined teichoic acid polymerase from *Staphylococcus epidermidis* [7].

Previously, cDNA encoding CM of CrdS cloned into the pET-32a(+) vector containing thioredoxin, and into the Champion™ pET SUMO system containing a SUMO (small ubiquitin-related modifier) coding region enabled high yield expression of CM, in the form of inclusion bodies [2]. The former vector was chosen because it is recognised to facilitate disulfide bond formation in the reducing environment of *E. coli* [8], alleviates toxic effects of recombinant protein production on host cells, prevents target proteins from proteolytic degradation and accelerates expression of proteins in a soluble form [9]. The inclusion bodies produced in *E. coli* were refolded using a range of buffers and non-surfactant sulfobetaines [2]. Refolded, chimeric CM was found to be inactive, although it showed a native-like circular dichroism spectrum [2].

The objective of the present work was to produce full-length CrdS through a eukaryotic wheat germ cell-free (CF) protein synthesis (WG-CFPS) expression system that enables rapid production of proteins [10]. CFPS systems based on cellular extracts, have emerged recently as efficient and versatile tools for the production of complex integral membrane proteins. Here, the entire process of protein production encompassing transcription and translation steps takes place *in vitro* [12–15]. The CFPS systems overcome many of the technical hurdles of *in vivo* membrane protein production as cell viability and protein production are essentially decoupled [14,16]. The CF systems, not being enclosed by a membrane are open and accessible, and allow supplementation of target-specific additives such as stabilisers, substrates, ligands, chaperones, surfactants and other components at any time during a CF reaction [16,17]. Moreover, the option to co-translationally insert membrane proteins directly into artificial hydrophobic environments often eliminates a need for reconstitution of membrane proteins into lipid environments [18]. In the past twenty years, a variety of extracts, configurations and expression modes have been established, developed and perfected [19]. WG-CFPS has been used for synthesis of mainly radio-labelled polypeptides in the past and only in recent years has substantial progress in protein yields of membrane and multi-domain proteins been achieved [10,11]. This progress has been primarily due to the removal of components causing damage to ribosomes and mRNA, so CFPS can be sustained for several days provided reaction substrates are replenished [19,20]. Last but not least, robotic automation of WG-CFPS has been achieved with the advent of robotised synthesisers and associated technical progression [21,22].

Our work with recombinant CrdS is aimed at a long-term goal to determine the three-dimensional (3D) structure of this integral membrane protein. In the previous work, the full-length form of CrdS was not produced in the *E. coli* host and only truncated forms were obtained [2]. This led us to explore new approaches towards stable expression of full-length CrdS. We became interested in deployment of particular avenues, such as co-translational insertion of CrdS in liposomes and application of nanodiscs. The emergence of nanodiscs as a tool to study structural aspects of membrane proteins in a near-native environment has gained considerable interest in the past decade [23,24]. During the process of spontaneous nanodisc self-assembly, the surfactant-solubilised membrane protein becomes surrounded by an annular lipid-bilayer patch, which is held together by a recombinant membrane scaffold protein (MSP). Following purification by size-exclusion chromatography (SEC), a uniform population of soluble, stable and correctly assembled membrane protein occupied nanodiscs is usually obtained [23,24].

In the current work, full-length CrdS was sub-cloned into the pEU-EO1™ plasmids for WG-CFPS, containing a 6xHis affinity tag and either Tobacco Etch Virus (TEV) or Factor Xa proteolytic sites. We investigated bilayer and dialysis modes of WG-CFPS and assessed yields of CrdS in the presence of a range of surfactants and surfactant peptides. Following co-translational insertion of CrdS in artificial liposomes, we demonstrated single-step purification by floatation through density gradient ultra-centrifugation. Furthermore, with the goal of structural studies, we assembled and purified CrdS nanodiscs to near homogeneity in two distinct lipid environments and characterised them by small-angle X-ray scattering (SAXS) using synchrotron radiation [25]. Synthesised CrdS was analysed by Matrix-Assisted Laser Desorption Ionization-Time of Flight Mass Spectrometry (MALDI-TOF/TOF MS) and assayed for catalytic activity.

2. Materials and methods

2.1. Chemicals and reagents

The sources of oligonucleotide primers, restriction and DNA-modifying enzymes, plasmid extraction kits, EDTA-free Complete Protease Inhibitor Cocktail tablets and other chemicals were described previously [2]. All lipids, except asolectin (Sigma, St. Louis, MO, USA) were purchased from Avanti Polar Lipids (Alabaster, AL, USA).

2.2. Recombinant plasmid construction

The full-length coding region of CrdS was amplified by PCR using the 5′ primer pairs (Table 1) from the pVS1512 plasmid of an 8.8 kb *EcoRI Agrobacterium* genomic fragment containing the *crdASC* genes [2]. The amplified fragments were cloned into the pGEM-T Easy vector system (Promega, Madison, WI, USA). For DNA amplifications the *E. coli* strain DH5α (Invitrogen, Carlsbad, CA, USA) was transformed with pGEM-His-CrdS, pGEM-His-TEV-CrdS and pGEM-His-Xa-CrdS constructs as recommended by the manufacturer. The plasmids were isolated and digested with *XhoI* and *NotI*, and the CrdS DNA fragments were sub-cloned in-frame into the pEU-EO1-HIS-TEV-MCS™ vector (CellFree Sciences, Tsurumi-ku, Yokohama, Japan) to generate the pEU-His-CrdS and pEU-His-TEV-CrdS constructs, and into the pEU-EO1-MCS™ vector (CellFree Sciences) to yield the pEU-His-Xa-CrdS construct. The three

Table 1
Primers used for ligation-based cloning of the pEU-His-CrdS, pEU-His-Xa-CrdS and pEU-His-TEV-CrdS DNA fusions.

Construct	Primer	Sequence[a]
pEU-His-CrdS	5′ Forward	**CTCGAG**AGTGCTGAAGGTGAC
	5′ Reverse	**GCGGCCGC**TTATCCTCAGAATGCCCGTGCGAG
pEU-His-Xa-CrdS	5′ Forward	**CTCGAG***ATTGAAGGACG*AAGTGCTGAACGTGAC
	5′ Reverse	**GCGGCCGC**TTATCCTCAGAATGCCCGTGCGAG
pEU-His-TEV-CrdS	5′ Forward	**CTCGAG**AGTGCTGAAGGTGAC
	5′ Reverse	**GCGGCCGC**TTATCCTCAGAATGCCCGTGCGAG

[a] Bold types indicate the *XhoI* (forward) and *NotI* (reverse) restriction sites. The italicised and underlined sequences indicate the proteolytic Factor Xa site and the stop-Gly-stop motif, respectively. The remainder of the sequences corresponds to coding regions of CrdS.

expression plasmids were transformed into the *E. coli* strain DH5α cells and the plasmid DNA was sequenced in both directions.

2.3. Wheat germ cell-free protein synthesis of CrdS

Wheat germ cell-free protein synthesis (WG-CFPS) of CrdS was performed sequentially through the uncoupled transcription and translation reactions. Care was taken to prevent RNAse contamination throughout by using RNase-free water (MP Biomedicals, Fountain Parkway Solon, Ohio, USA) and RNase AWAY® (Molecular BioProducts, San Diego, CA, USA) to sanitise the workspace.

2.3.1. Preparation of plasmid DNA

DNA was isolated from the *E. coli* cells transformed with the pEU-His-CrdS, pEU-His-TEV-CrdS and pEU-His-Xa-CrdS constructs using the PureYield™ Plasmid Miniprep System (Promega). The quality of purified DNA, expressed as A_{260}/A_{280} was within a range of 1.8–2.0. The DNA was used at a concentration of 1 μg/μl.

2.3.2. Transcription (preparation of mRNA)

Plasmid DNA of the pEU-His-CrdS, pEU-His-TEV-CrdS and pEU-His-Xa-CrdS constructs (2.5 μg) was combined with a transcription buffer (CellFree Sciences) and the nucleotide-tri-phosphate (NTP) mix (ATP, CTP, GTP, and UTP each at 3 mM) (Roche, Indianapolis, USA), SP6 RNA polymerase (1 U/μl) (Promega), RNAsin (1 U/μl) (Promega) and RNase free water (MP Biomedicals) were added to a total volume of 25 μl [20]. Synthesis of mRNA proceeded at 42 °C for 2.5 h. The quality of synthesised mRNA was confirmed by 1% (w/v) agarose gel electrophoresis.

2.3.3. Translation (synthesis of CrdS)

Translation was performed through either bilayer mode in the 150 μl total reaction volume or through dialysis mode of 50 μl internal reaction volumes, in a Slide-A-Lyser Mini dialysis cup, molecular mass cut-off 10 kDa (Thermo Scientific, Rockford, IL, USA). The translation reactions were setup in the dialysis buffer (CellFree Sciences) containing 0.3 mM L-amino acids (CellFree Sciences) with 10 μl mRNA/25 μl reaction mix. Translation reactions contained the WEPRO wheat germ extract (6.3 μl/25 μl) (CellFree Sciences), creatine-phosphokinase (0.4 μg/μl) (Roche) and RNase free water (MP Biomedicals). Biotinylated tRNA (1.5 μl/25 μl) (Promega) was added during translation in specific cases to allow for detection of CrdS through a streptavidin-coupled assay. The synthesis in bilayer mode was carried out as described [26] at 20 °C for 20 h, and the synthesis in dialysis mode proceeded according to [20] at 20 °C for up to 72 h, with the supply of a fresh dialysis buffer after 24-hour time intervals. The translation mixture in dialysis mode was placed in dialysis cups and suspended in a buffer reservoir containing 0.6 ml of the dialysis buffer (CellFree Sciences). The translation reaction mixture was supplemented with surfactants, surfactant peptides, amphipols and liposomes, prepared as specified below.

2.3.4. CrdS synthesis with surfactants

Non-ionic and zwitterionic surfactants of alkyl-glycosides, steroids, polyoxyethylene-alkyl-ethers, polyethyleneglycol and long-chain phosphoglycerol derivatives were tested above their critical micellar concentrations (CMC) in translation reactions. The list of surfactants, their concentrations and sources are summarised in Table 2.

2.3.5. CrdS synthesis with surfactant peptides

The CrdS synthesis proceeded with 1, 2 and 4 mM concentrations of the acetylated Ac-AAAAAAD (Ac-Ala-Ala-Ala-Ala-Ala-Ala-Asp), Ac-IIID (Ac-Ile-Ile-Ile-Asp) and Ac-LLLK-NH_2 (Ac-Leu-Leu-Leu-Lys-NH_2) surfactant peptides. The peptides were synthesised by Mimotopes (Clayton, Victoria, Australia) and dissolved in RNase free water (MP Biomedicals) to prepare 50 mM stock concentrations.

2.3.6. CrdS synthesis with amphipols

CrdS synthesis proceeded with amphipol A8-35 (Anatrace, Santa Clara, CA, USA) and styrene maleic acid (SMA) at concentrations ranging from 0.5% to 4%. SMA was kindly provided by Dr Timothy Knowles (University of Birmingham, UK).

2.3.7. CrdS synthesis with liposomes

The synthesis of CrdS proceeded with liposomes prepared at final lipid concentrations of 2.5 mg/ml, 5 mg/ml and 10 mg/ml either by using a single lipid component or a mixture of lipids; in the latter case DOPG was mixed with POPE in a 2:3 ratio, by weight. The list of lipids used, their formulae and sources are given in Table 3. CrdS quantification was performed using the ImageJ software [27] from scanned Western blot images. A CrdS calibration curve was based on known amounts of BSA. The liposomes were prepared as follows. The pre-weighted lipid powder in a glass-tube was dissolved in chloroform and dried on a rotary evaporator followed by purging with a stream of nitrogen to remove chloroform. The resultant lipid coating in the glass test-tube was dried for 2 h under *vacuo* to remove every trace of chloroform. The dried lipid film was dissolved in the lipid re-hydration buffer (25 mM HEPES, 100 mM NaCl, pH 7.5) to a final concentration of 100 mg/ml. The tube was constantly agitated until dissolved and was kept above the transition temperature of a particular lipid, which varied between −20 °C and 23 °C. The suspension was extruded 21 times, above the lipid transition temperature, using the Avestin LiposoFast extruder (Avestin, Ontario, Canada) through polycarbonate filters with pore sizes of 100 or 400 nm to produce a population of unilamellar liposomes.

2.4. Purification of CrdS proteo-liposomes through floatation on Accudenz gradient

A 75 μl aliquot taken from a WG-CFPS translation reaction containing liposomes was mixed with 75 μl of 80% (w/v) Accudenz (Accurate Chemical and Scientific, Westbury, NY) prepared in 25 mM HEPES, pH 7.5, containing 100 mM NaCl and 10% (v/v) glycerol. Accudenz is a non-ionic, biologically inert density gradient component. The mixture was transferred to an ultra-clear centrifuge tube (Beckman Coulter, Fullerton, CA, USA), successively overlaid with 350 μl of 30% (w/v) Accudenz in the same buffer and with 100 μl of 25 mM HEPES, pH 7.5, containing 100 mM NaCl. The mixture was centrifuged at 100,000×*g* for 4 h at 4 °C in the L-80 XP ultra-centrifuge using a SW55Ti rotor (Beckman Coulter). After ultra-centrifugation, 60 μl fractions were sequentially collected from the top of the gradient and examined by SDS-PAGE (sodium dodecyl sulphate-polyacrylamide gel electrophoresis) and Western immuno-blot analyses as described below.

2.5. Purification of CrdS through Immobilized Metal Affinity Chromatography (IMAC)

The CrdS protein synthesised in the presence of Brij-58 in dialysis mode was equilibrated in 10 mM $Na_2HPO_4 \cdot 2\ H_2O$, 150 mM NaCl and 10 mM imidazole, pH 8.0, and added to the Ni-NTA resin (Bio-Rad, Hercules, CA, USA) pre-equilibrated in the same buffer. The mixture was incubated for 16 h at 4 °C and loaded onto a 1×10 cm Econo-column (Bio-Rad). The flow-through was collected and the resin was washed four times with five bed volumes of a wash buffer (20 mM $Na_2HPO_4 \cdot 2\ H_2O$, 300 mM NaCl, 20 mM imidazole, pH 8.0) containing 0.04% (w/v) Brij-58. The CrdS protein was eluted six times with one bed volume of the buffer specified above that contained 50 mM, 100 mM, 150 mM, 200 mM, 250 mM and 500 mM imidazole. The fractions were evaluated by SDS-PAGE and Western immuno-blot analyses using either a mouse IgG2a isotype anti-6xHis monoclonal antibody from Clontech (Takara Bio, Shiga, Japan) or rabbit polyclonal antibody, raised against the intracellular catalytic region of CrdS [2]. The

Table 2
Surfactants used during wheat germ cell-free synthesis of CrdS.

Surfactants	Short name	Final concentration	x CMC	Source[a]
n-Dodecyl-β-D-maltoside	DDM	0.8% (w/v)	12	Anatrace
n-Decyl-β-D-maltoside	DM	0.08% (w/v)	9.2	Anatrace
n-Octyl-β-D-glucopyranoside	β-OG	0.5% (w/v)	1.3	Anatrace
Digitonin		0.4% (w/v)	4.5	Sigma
Polyoxyethylene-(20)-cetyl-ether ($C_{16/20}$)	Brij-58	0.04% (w/v)	4.7	Sigma
Polyoxyethylene-sorbitan-monolaurate 80	Tween 80	3% (v/v)	1.5	Sigma
Polyethylene-glycol-p-1,1,3,3-tetramethyl-butylphenyl-ether	Triton X-100	0.5% (v/v)	33.5	BDH
Nonylphenyl-polyethylene-glycol	NP40	0.5% (w/v)	1.3	Merck
3-[(3-Cholamidopropyl)dimethylammonio]-1-propansulfonate	CHAPS	0.5% (w/v)	1.8	Anatrace

[a] The sources are Anatrace (Santa Clara, CA, USA), Sigma (St. Louis, MO, USA), BDH Chemicals (Poole, Dorset, UK) and Merck Chemicals (Darmstadt, Germany).

purity of CrdS after IMAC was estimated comparatively based on relative contributions of CrdS and other protein components that were detected on the SDS-PAGE gels.

2.6. Preparation of CrdS nanodiscs

Nanodiscs were prepared [23,24] with modifications as described below. The CrdS protein was purified by IMAC as described above, and concentrated in a Microcon Ultracel YM10 microconcentrator, molecular mass cut-off 10 kDa (Millipore, Billerica, USA). Approximate protein concentration of CrdS was calculated using a Qubit Protein Assay Kit (Invitrogen) and SDS-PAGE. The lipid components of nanodiscs comprised either the *E. coli* total lipid extract or POPC (Avanti Polar Lipids, Alabaster, AL, USA) that were prepared essentially as described for liposomes, except that sodium cholate (Sigma) was added to the lipid re-hydration buffer such that the final concentration during reconstitution was between 20 and 40 mM. The plasmid encoding MSP1E3D1, acquired from Addgene (Cambridge, MA, USA) was prepared as described [28,29]. Empty POPC nanodiscs were prepared at a reconstitution ratio of 130:1 (lipid:MSP), while the nanodiscs containing CrdS were prepared at the 0.5:120:1 (CrdS:lipid:MSP) ratio in a total volume of 225 μl. The solubilised components were mixed and incubated under rotation for 2 h at 4 °C. Biobeads SM-2 (Bio-Rad) were added to the mixture at 0.5 g/ml to facilitate surfactant removal and to initiate nanodisc assembly. After 16 h, a hole was pierced at the bottom of the test tube using a 0.4 mm needle and the nanodiscs were collected by centrifugation (1500×*g*, 2 min, 22 °C) into a new test tube. Nanodisc samples were re-centrifuged (10,000×*g*, 2 min, 22 °C) to remove precipitates before SEC. The presence of CrdS protein in nanodiscs was examined by SDS-PAGE and Western immuno-blot analyses on a polyvinylidene difluoride (PVDF) membrane with detection using a mouse 6xHis monoclonal antibody (Clontech).

2.6.1. Purification of the CrdS nanodiscs through SEC

The CrdS nanodiscs were purified at room temperature on a Superdex 200 10/300 GL column (GE Healthcare, Piscataway, NJ, USA) connected to an ÄKTA™ Purifier UPC-10 system (GE Healthcare). The void volume of the Superdex column was determined with Blue Dextran. After pre-equilibration of the column in TBS buffer (40 mM Tris, 0.3 M NaCl, pH 7.4), samples (225 μl) were pre-filtered through 0.45 μm nylon ISO-Disc filters (Supelco, Bellefonte, PA, USA) and run at a flow rate of 0.5 ml/min in TBS on the ÄKTA™ Purifier. Peaks were monitored at

Table 3
Lipids used for preparation of liposomes for wheat germ cell-free synthesis of CrdS.

Lipid	Short name	Charge[a]	Structure
1,2-Dimyristoyl-*sn*-glycero-3-phosphocholine	DMPC	Z	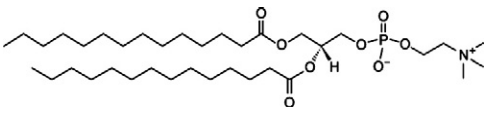
1-Palmitoyl-2-oleoyl-*sn*-glycero-3-phosphocholine	POPC	Z	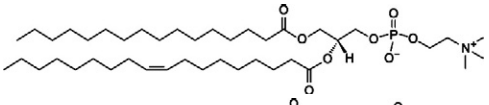
1,2-Dioleoyl-*sn*-glycero-3-phosphocholine	DOPC	Z	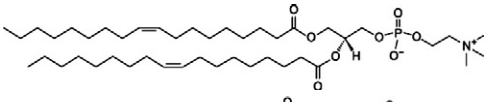
1,2-Dioleoyl-*sn*-glycero-3-phospho-(1′-*rac*-glycerol)	DOPG	A	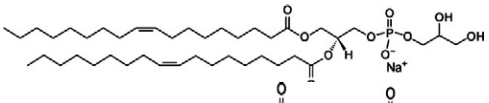
1-Palmitoyl-2-oleoyl-*sn*-glycero-3-phosphoethanolamine	POPE	Z	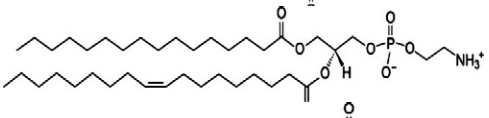
1,2-Dioleoyl-3-trimethylammonium-propane	DOTAP	C	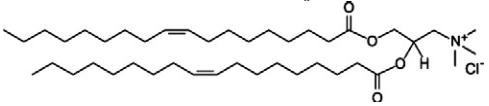
Asolectin	Asolectin	Z	Not applicable
E. coli total lipid extract	–	–	Not applicable

[a] Z, A and C indicate zwitterionic, anionic and cationic lipids, respectively.

254 nm and 1 ml fractions were collected. The nanodisc samples were concentrated in a Microcon Ultracel YM10 micro-concentrator to approximately 200 μl volumes and kept at 4 °C until analysis.

2.7. Analysis of CrdS nanodiscs by small-angle X-ray scattering using synchrotron radiation

Small-angle X-ray scattering (SAXS) data of CrdS nanodiscs were collected on the SAXS/WAXS beamline of the Australian Synchrotron (Melbourne, Australia) using a Pilatus-1M pixel-array detector (Dectris, Switzerland). For each data set 25 frames of a 2-second exposure time were collected from a sample moving through the X-ray beam at a constant 5 μl/s flow rate in a temperature-controlled 1.5 mm quartz capillary. Solutions of CrdS inserted in the *E. coli* total lipid extract or POPC nanodiscs were measured at 30 °C in TBS buffer at a single MSP-based protein concentration (~0.1 mg/ml). The sample-to-detector distance was 1.6 m, covering a range of momentum transfer 0.01 Å-1<q<0.6 Å-1 ($q = 4\pi\sin\theta/\lambda$, where 2θ is the scattering angle and $\lambda = 1.03$ Å is the X-ray wavelength). Comparison of successive 2-second frames revealed no detectable radiation damage. Data from the detector were normalised to the transmitted beam intensity, averaged and scattering of the buffer solutions was subtracted using the ScatterBrain software package available at the Australian Synchrotron. The SAXS profiles were analysed using the latest cross-platform ATSAS package [30] and scattering density distributions were determined by indirect Fourier transformation (IFT) using the program GNOM [31].

2.8. SDS-PAGE, Western immuno-blot analyses and protein determination

Typically, 5 μl of CF reactions was evaluated by SDS-PAGE analysis as described [2], except that prior to loading on SDS-PAGE gels, the protein samples were incubated for 30 min at 37 °C in the SDS-PAGE loading buffer. The proteins contained in CF reactions included newly synthesised CrdS and wheat germ extract components. The overall protein concentration varied between 5 and 6 mg/ml. The Western immuno-blot analysis [2] was carried out with 0.45 μm PVDF transfer membranes (Amersham Biosciences, Little Chalfont, Buckinghamshire, UK). Working dilutions of antibodies were as follows: anti-His 1:4000 (v/v), anti-CrdS 1:4000 (v/v) and secondary antibody 1:5000 (v/v). Working solutions of antibodies were prepared in 25 mM Tris–HCl buffer, pH 7.5 containing 137 mM NaCl, 3 mM KCl and 0.05% (w/v) Tween 20. Blots were incubated with antibodies for a duration between 1 to 16 h with gentle agitation at 4–8 °C. The blots were developed with the Novex® ECL HRP Chemiluminescent Substrate Reagent Kit (Invitrogen) or with the BCIP/NBT-purple liquid reagent (Sigma) according to the manufacturer's instructions and the images were scanned (Clinx Science Instruments, Shanghai, China). Where Transcend tRNA was used, immuno-blot detection was carried out *via* streptavidin conjugated with the alkaline phosphatase chromogen (Sigma) and the membranes were developed with the BCIP/NBT-purple liquid reagent until a desired intensity was achieved. Protein staining on SDS-PAGE gels proceeded either by Coomassie Brilliant Blue R-250 (Sigma) [2] or through SilverQuest Silver Staining Kit (Invitrogen). Total protein staining on PVDF membranes proceeded with Ponceau S (Sigma). Protein concentration was determined using the Qubit Protein Assay Kit (Invitrogen) or by the Protein Assay Kit, based on a Coomassie Brilliant Blue G-250 dye shift (Bio-Rad) [2]. Precision Plus protein molecular mass standards were from Bio-Rad. Purity of CrdS preparations resolved by IMAC and density gradient centrifugation was determined visually based on relative contributions of individual protein bands on SDS-PAGE gels. Semi-quantitative estimation of protein content on SAS-PAGE gels was based on known amounts of BSA.

2.9. Other procedures

2.9.1. Tryptic mapping of CrdS by Matrix-Assisted Laser Desorption Ionization-Time of Flight Mass Spectrometry

The band corresponding to synthesised CrdS with Brij-58 in dialysis mode, was excised from the SDS-PAGE gel and placed in sterile Milli-Q water. The protein was digested with trypsin and the peptide mixture was analysed *via* MALDI-TOF/TOF MS. The MS and corresponding MS/MS spectra were combined and submitted to a Mascot database search as described [2].

2.9.2. CrdS proteo-liposomal particle sizing

CrdS proteo-liposomes (60 μl fraction 3 following the Accudenz density ultra-centrifugation) and empty liposomes were centrifuged (10,000×*g*, 2 min, 22 °C), the pellet was re-suspended in 50 mM MOPS-KOH buffer, pH 7.8 to a volume of 150 μl and dialysed in the D-Tube™ Dialyzer Mini tubes (Novagen, Madison, WI, USA) for 16 h at 4 °C against the same buffer to remove Accudenz. The dialysed, non-concentrated proteo-liposomes (50 μl) were mixed with 950 μl of the 50 mM MOPS-KOH buffer, pH 7.8. The diameter of the liposomes was determined using dynamic light scattering with the NICOMP 380 Particle Sizing Systems (Santa Barbara, CA, USA) operating in vesicle mode and the data was weighted on a number of liposomes.

2.9.3. Liposome-associated topology of CrdS

CrdS (60 μg) in the DMPC liposomes was digested in 50 mM Tris–HCl, pH 8.0, 0.5 mM EDTA and 1 mM DTT with the TEV protease (2 μg) at room temperature for 24 h. The TEV protease was prepared in-house using the pRK793 expression plasmid [32]. Topology of CrdS was analysed through Western immuno-blot analysis with anti-6xHis antibody (Clontech) as described above.

2.9.4. Transmission electron microscopy (TEM) of liposomes and CrdS nanodiscs

CrdS-occupied and empty DMPC liposomes were purified through floatation in an Accudenz density gradient as described above. About 20 μl of the purified, non-concentrated specimen of liposomes from fraction 3 was placed on a thin piece of parafilm. The carbon coated grid was floated on the droplet for 10 min to let liposomes absorb. The grids were washed thrice with 50 mM HEPES, pH 7.5 containing 100 mM NaCl, followed by sterile Milli-Q water and air dried. The grids were stained with aqueous 0.5% (w/v) uranyl acetate (Sigma) and washed five times with water and air dried. For nanodiscs, both empty and CrdS-assembled discs were imaged *prior* to purification through SEC. Crude nanodiscs were absorbed for 1 min onto collodion and carbon coated nickel grids that were washed as described above, stained with aqueous 2% (w/v) uranyl acetate and processed as specified for liposomes. The liposomes and nanodiscs were imaged on the transmission electron microscope Philips CM 100 (FEI, Hillsboro, Oregon, USA) operated at 80 kV, at the Adelaide Microscopy Centre of the University of Adelaide.

2.9.5. (1,3)-β-D-Glucan synthase activity

The reaction mixtures contained 3.4 mM UDP-[^{3}H]-glucose (specific activity 10–45 Ci/mmol) (Perkin Elmer, Waltham, MA, USA), 80 μg α-amylase, 0.27 mM GTP, 9 mM $MgCl_2$ (all from Sigma), 2.2 mM laminaribiose (Megazyme, Bray, Wicklow, Ireland) and 10 μl of enzyme samples [33,34]. The enzyme samples were taken from CF reactions and represented either non-concentrated CrdS synthesised with Brij-58 or Ac-AAAAAAD, and CrdS co-translationally inserted in the *E. coli* total lipid extract liposomes. The enzyme activities of CrdS reconstituted in the *E. coli* total lipid extract or POPC nanodiscs were also measured. The mixed membrane fraction isolated from *Saccharomyces cerevisiae*, as described below, was used as a positive control for activity measurements [33,34]. The (1,3)-β-D-glucan synthase reactions incubated at 25 °C for various time intervals were stopped by adding 50 μl of

10% (w/v) trichloroacetic acid and the mixtures were filtered using the Millipore filter method [34]. The radioactivity incorporated into (1,3)-β-D-glucan, which represents the product of the synthetic reaction, was measured by scintillation counting using the EcoLite Scintillation fluid (MP Biomedicals) and a LS6500 Scintillation Counter (Beckman Coulter).

The mixed membrane fraction of *S. cerevisiae* was prepared from cells grown in the YPD (yeast extract-peptone-dextrose) medium at 28 °C. The cells were harvested in the early logarithmic phase of growth. Cell pellets were resuspended in buffer A [25 mM HEPES, pH 7.8, 5 mM EDTA, 10 mM NaF, 1 mM phenylmethylsulphonyl fluoride, 1 mM DTT, EDTA-free Complete Protease Inhibitors and 30% (v/v) glycerol] and disrupted with glass beads (Sigma) in a Bead-Beater (BioSpec Products, Bartlesville, OK, USA). The disintegrated cells were centrifuged (12,000×*g*, 10 min, 4 °C), the pellet was re-suspended in buffer A, transferred to the Polyallomer centrifuge tubes (Beckman Instruments, Fullerton, CA, USA) and centrifuged (100,000×*g*, 50 min, 4 °C). The resulting pellet was resuspended in buffer A with 2 μM GTP and 5 mM UDP-glucose, and stored at −80 °C in aliquots. The (1,3)-β-D-glucan product was characterised as described [34]. Here, the radioactive product was hydrolysed by (1,3)-β-D-exo-glucanase from Mollusc (Sigma) for 16 h at 30 °C and the remaining radioactivity was measured by scintillation counting as described above. Treatments of radioactive products by boiled (1,3)-β-D-exo-glucanase and α-amylase (Sigma) were conducted for 16 h at 30 °C and remaining radioactivity was estimated.

3. Results

3.1. Construction of pEU-EO1™ expression plasmids for wheat germ cell-free protein synthesis

PCR-amplified full-length cDNA of CrdS was cloned into the pGEM-T Easy vector system, using the primers listed in Table 1. The amplified CrdS coding regions inserted in the pGEM-T-CrdS plasmids were sequenced and found to be correct. The *XhoI*- and *NotI*-digested blunt-ended pGEM-T-CrdS DNA fusions were sub-cloned in-frame into the pEU-EO1™ vectors affording the three expression plasmids pEU-EO1-His-CrdS, pEU-EO1-His-Xa-CrdS and pEU-EO1-His-TEV-CrdS. These DNA fusions contained the coding region of CrdS and the sequences encoding 6xHis affinity tags and either Factor Xa or TEV (Tobacco Etch Virus) proteolytic sites at their 5′-termini, followed with cloning overhang sequences of 9–12 bp long. The 6xHis tag and the TEV site in the pEU-EO1-His-TEV-CrdS plasmid were separated by a 7-residue linker DYDIPTT that was designed to facilitate cleavage of a 6xHis affinity tag *via* the TEV protease. The cleavage of 6xHis-TEV-CrdS with the latter protease would leave an additional Gly residue at the NH_2-terminus of CrdS, while the cleavage with the Factor Xa protease afforded an intact NH_2-terminus of CrdS.

3.2. CrdS is synthesised during wheat germ cell-free protein synthesis in bilayer mode and co-translationally inserted in liposomes

Efficiency of wheat germ CF protein synthesis (WG-CFPS) system was investigated in bilayer mode adopting de-coupled transcription and translation reaction modes. The translation was carried out for 16 h at 20 °C in the presence of DMPC liposomes with all three pEU-EO1-His-CrdS, pEU-EO1-His-Xa-CrdS and pEU-EO1-His-TEV-CrdS mRNAs. As indicated in Fig. 1, with all three DNA fusions, SDS-PAGE profiles showed good yield of CrdS in the presence of DMPC liposomes. Here, low μg quantities of CrdS/150 μl of reaction mixtures were obtained (Fig. 1, lanes 1–3), while no CrdS was synthesised in the reaction mixture lacking mRNA (Fig. 1, lane 4). We observed a discrepancy between migration of the synthesised 6xHis-CrdS, 6xHis-Xa-CrdS and 6xHis-TEV-CrdS proteins on the SDS-PAGE gels and their theoretical molecular masses, however this anomaly was not unprecedented [35].

The data presented in Fig. 1 (lane 3) with the His-TEV-CrdS construct was corroborated in a separate experiment (Fig. 2). The

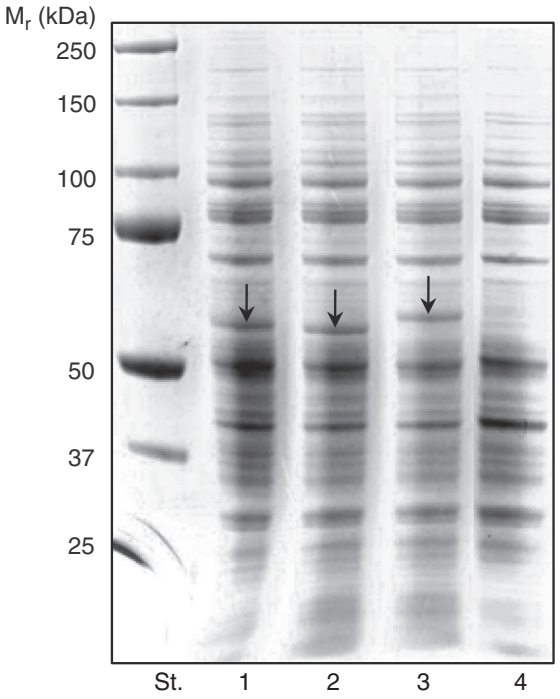

Fig. 1. SDS-PAGE of WG-CFPS translation reactions performed in bilayer mode and supplemented with DMPC liposomes (10 mg/ml) and mRNA of His-CrdS, His-Xa-CrdS and His-TEV-CrdS in lanes 1–3, respectively. Lane 4 contains the reaction lacking mRNA. The black arrows point to the synthesised CrdS proteins that migrate to a region of 56–60 kDa; theoretical masses of the CrdS proteins are between 73 and 76 kDa. St. indicates molecular mass standards.

identity of the synthesised CrdS protein was verified through Western blot using the anti-CrdS antibody (Fig. 2B, lanes 1 and 2). In addition, synthesis of CrdS was also confirmed by detection with alkaline phosphatase-conjugated streptavidin (Fig. 2C, lanes 1 and 2). Our next task was to assess, if synthesised CrdS was co-translationally inserted in the DMPC liposomes or if CrdS aggregated during translation (Fig. 2). When the translation reaction with CrdS was separated into the supernatant and pellet fractions by centrifugation, the synthesised CrdS protein remained associated with the pellet fraction while hardly any CrdS protein was detected in the supernatant, pointing to the fact that CrdS may have been successfully reconstituted in DMPC liposomes (Figs. 2C and 3). As indicated in Fig. 2B, CrdS could efficiently be detected with the rabbit polyclonal antibody, raised against the intracellular catalytic region of CrdS [2], or with the streptavidin-alkaline phosphatase conjugate (Fig. 2C). In the latter case, streptavidin targets biotinylated lysine residues that had been incorporated into CrdS during CFPS from biotinylated tRNA. Hence, this assay allows for detection of only newly synthesised CrdS protein molecules from CrdS mRNA. It is of note that the higher molecular mass protein bands that migrated between 70 and 250 kDa (Fig. 2C) resulted from the detection of native biotinylated proteins contained in the wheat germ extract, and not due to oligomeric assemblies of CrdS. Notably, the protein of about 130 kDa size found in all preparations (Fig. 2B) most likely represented a wheat germ protein as it was not detected *via* alkaline phosphatase-conjugated streptavidin (Fig. 2C).

To confirm that the pellet fraction contained the CrdS DMPC-liposomes and not simply aggregated CrdS, the proteo-liposomes of approximately 100 nm diameter were subjected to floatation by Accudenz density gradient ultra-centrifugation and then detected [36]. As indicated in Fig. 3 (lane 3), fractions with the CrdS proteo-liposomes detected with anti-CrdS antibody, floated near the top of the gradient. This observation highlighted the fact that over 95% of CrdS was successfully inserted co-translationally in the

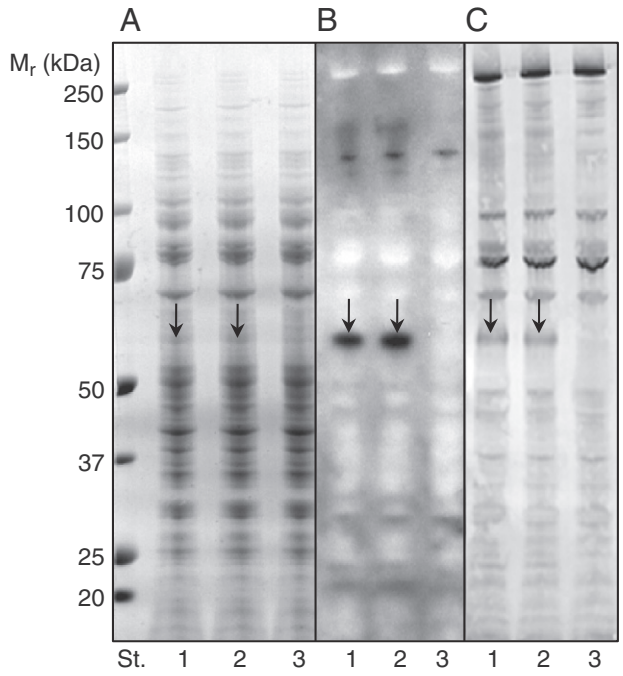

Fig. 2. SDS-PAGE and Western immuno-blot analyses of WG-CFPS translation reactions performed in bilayer mode and supplemented with DMPC (2.5 mg/ml) liposomes. Lanes 1 and 2 (duplicates) in the Coomassie stained panel A, and in the Western immuno-blot with the anti-CrdS antibody (panel B), contain translation reactions with His-TEV-CrdS mRNA, and lane 3 represents the reaction lacking mRNA. Lane 1 in the Western immuno-blot detected *via* alkaline phosphatase-conjugated streptavidin (panel C) contains the total WG-CFPS translation reaction, and lanes 2 and 3 represent separated pellet and supernatant fractions, respectively. The black arrows point to synthesised CrdS that migrate to a region of 56–60 kDa; CrdS theoretical mass is 73–76 kDa. St. indicates molecular mass standards.

DMPC liposomes, while only very low amount of synthesised CrdS was found at the bottom of the test tube in the form of an aggregate (Fig. 3 inset, lane 10). Further, the floatation through Accudenz density gradient using ultra-centrifugation substantially improved the purity of the CrdS proteo-liposomes. The purified CrdS-liposomal preparations (Fig. 4A) and those without CrdS (empty DMPC liposomes) were imaged by transmission electron microscopy (TEM). In these images (Fig. 4), the proteo-liposomes with or without CrdS appeared as rounded objects, sizes of which ranged between 80 and 100 nm. No significant variations in the appearance of liposomes with and without reconstituted CrdS were observed (Fig. 4A and B). Notably, in both cases fusion of unilamellar liposomes into the multilamellar structures was observed.

3.3. Screening of CrdS production using wheat germ cell-free protein synthesis in bilayer mode with liposomes prepared from a variety of lipids

The next question to address was whether other types of lipids could also lead to successful incorporation of CrdS in their bilayers. We investigated the effects of lipids on CrdS synthesis in the high-throughput bilayer mode. Here, CrdS was synthesised in the presence of a variety of liposomes, prepared from a single zwitterionic, anionic and cationic lipid components or a mixture of lipids at concentrations ranging from 2.5 mg/ml to 10 mg/ml (Table 3). The CrdS protein synthesised under these conditions was detected directly on SDS-PAGE gels, as described in the Materials and methods section. The yields of CrdS synthesised in the presence of liposomes prepared from a variety of lipids are summarised in Fig. 5. The highest yields of CrdS occurred with liposomes prepared from zwitterionic lipids DMPC and with liposomes prepared from soybean asolectin and *E. coli* lipids, followed by liposomes prepared from zwitterionic DOPC and POPC (Fig. 5). No CrdS was synthesised in the presence of liposomes prepared from charged lipids, *i.e.* DOPG (anionic lipid) and DOTAP (cationic lipid). However surprisingly, when the liposomes were prepared from DOPG (anionic lipid) and POPE (zwitterionic lipid) in a ratio of 2:3 by weight, the CrdS protein was synthesised (Fig. 5). The liposomes prepared from the total lipid extract of *E. coli* also led to high yield of CrdS; this yield was comparable to that during CFPS with the zwitterionic DMPC and with the asolectin liposomes. The conclusion from these experiments was that lipid type and composition were of paramount importance for a successful co-translational insertion of CrdS in high yields.

3.4. CrdS production through wheat germ cell-free protein synthesis in bilayer mode with surfactants, surfactant peptides and amphipols

A range of surfactants, surfactant peptides and amphipols were screened during CFPS of CrdS (Table 2, Figs. 6 and 7). The list of surfactants, their sources and concentrations that were above their CMC are summarised in Table 2. The effect of the tested surfactants on synthesis of CrdS was variable (Fig. 6). Out of nine surfactants tested (Table 2), four surfactants namely Brij-58, digitonin, Triton X-100 and Tween 80 were compatible with CFPS, leading to production of CrdS in a soluble form, while with β-OG, NP40 and CHAPS the CrdS synthesis was not observed (data not shown). The highest yields of CrdS were achieved with Brij-58, followed by digitonin, Triton X-100 and Tween 80 (Fig. 6).

CFPS of CrdS in the presence of the three acetylated surfactant peptides Ac-AAAAAAD (Ac-Ala-Ala-Ala-Ala-Ala-Ala-Asp), Ac-IIID (Ac-Ile-Ile-Ile-Asp), and Ac-LLLK-NH_2 (Ac-Leu-Leu-Leu-Lys-NH2) was carried out at 1 mM, 2 mM and 4 mM concentrations (Fig. 7). The CrdS protein was synthesised in the presence of all the three peptides, although the yields of CrdS varied. CrdS yield was higher in the presence of Ac-AAAAAAD and Ac-IIID at 1 mM and 2 mM concentrations (Fig. 7, lanes 3–4 and 6–7), compared to that with Ac-LLLK-NH_2 (Fig. 7, lanes 9–10). Notably, at 4 mM concentrations of the surfactant peptides, CrdS synthesis was either decreased or inhibited, in particular with Ac-AAAAAAD (Fig. 7, lanes 5, 8 and 11).

Finally, the presence of amphipols A8-35 and SMA in 0.5% (w/v) to 4% (w/v) concentrations was found to be inhibitory during CFPS of CrdS (data not shown).

3.5. Synthesis of CrdS with Brij-58 in dialysis mode and purification of CrdS through Immobilized Metal Affinity Chromatography

Optimal conditions for WG-CFPS of CrdS in bilayer mode were selected to set up a reaction in dialysis mode, as described in the Materials and methods section. The synthesis was carried out in the presence of 0.04% (w/v) Brij-58 for 24 h, 48 h and 72 h, and the reaction mixtures were analysed by SDS-PAGE (Fig. 8, lanes 1–3). Based on our semi-quantitative estimations, yield of CrdS in the presence of Brij-58 was as high as 1 mg/ml after 48 h (Fig. 8, lane 2) and this yield remained unchanged after the next 24-hour incubation period (Fig. 8, lane 3).

The CrdS protein synthesised through dialysis mode in the presence of Brij-58 was purified by Immobilized Metal Affinity Chromatography (IMAC) using a Ni-NTA affinity resin. The data in Fig. 9 indicate that CrdS could be purified significantly from a crude translation reaction by IMAC, and that reasonable purity of CrdS was achieved in the fractions eluted with 150 mM, 200 mM, 250 mM imidazole (Fig. 9, lanes 9–11). On the other hand, contaminating components were removed during the 20 mM imidazole washing steps (Fig. 9, lanes 3–6). The protein sample eluted with 250 mM imidazole contained the highest amount of CrdS with fewer contaminants as detected on the Coomassie Brilliant Blue R-250-stained SDS-PAGE gel (Fig. 9, lane 11, black arrow). The purity of CrdS (Fig. 9, lane 11), which should be the only newly synthesised membrane protein in

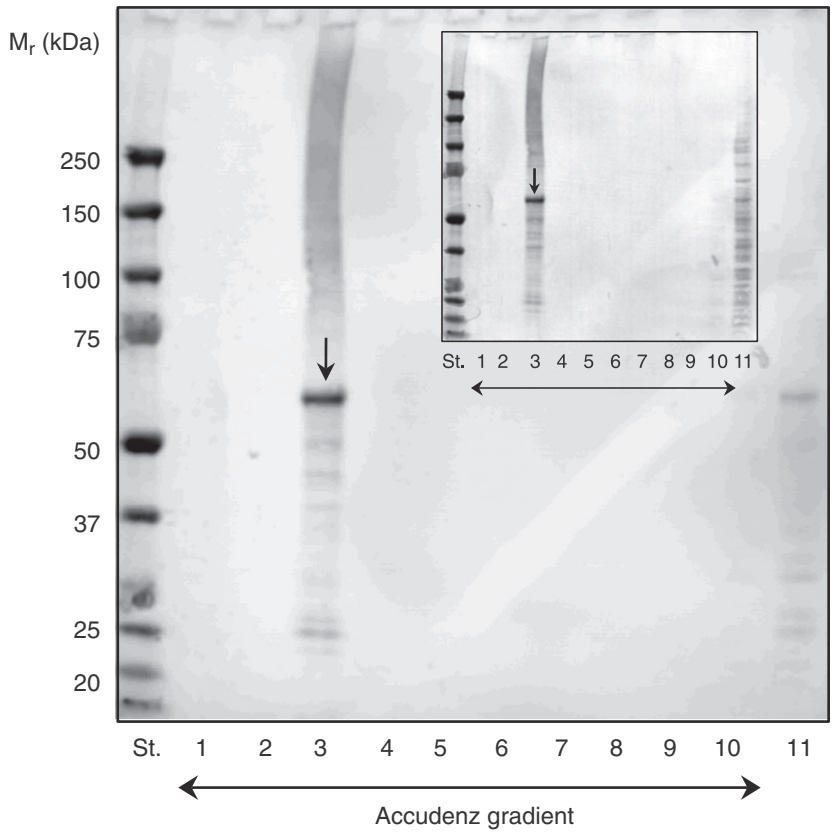

Fig. 3. Density gradient ultra-centrifugation of the CrdS proteo-liposomes made from DMPC. Western immuno-blot analysis was performed with the anti-CrdS antibody. Lanes 1–10 represent fractions collected after ultra-centrifugation. Lane 3 contains the fraction with CrdS that has successfully been incorporated in DMPC liposomes and lane 11 contains a non-fractionated WG-CFPS translation reaction mixture supplemented with the DMPC liposomes. The inset shows the membrane stained with Ponceau S. The black arrows point to synthesised CrdS that migrates to a region of 56–60 kDa; CrdS theoretical mass is 73–76 kDa. St. indicates molecular mass standards.

this preparation, was estimated to be between 50% and 60%. This estimation formed a basis for stoichiometry to assemble CrdS nanodiscs.

3.6. CrdS synthesised through wheat germ cell-free synthesis is a full-length protein

CrdS synthesised in the presence of Brij-58 in dialysis mode was purified by IMAC, and analysed by SDS-PAGE and the Western immuno-blot analysis using the anti-6xHis antibody and the rabbit polyclonal antibody, raised against the intracellular CM of CrdS [2]. The protein band corresponding to CrdS was excised from the SDS-PAGE gel and subjected to tryptic digestion. The analysis of tryptic fragments was performed by MALDI-TOF/TOF MS (Table 4). A Mascot database searches of the peptide sequences matched perfectly the generated peptide ions to the putative (1,3)-β-D-glucan synthase catalytic subunit (GenBank accession AF057142) (Table 4).

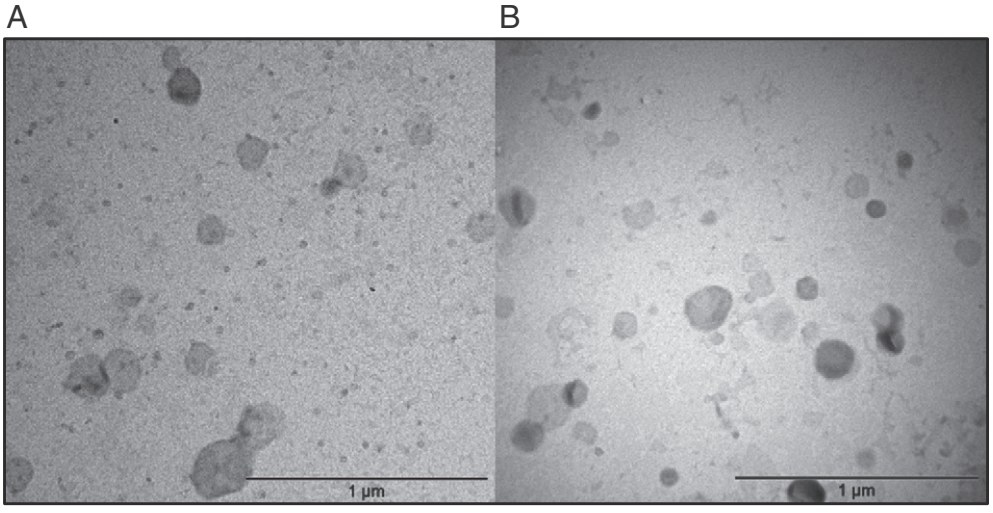

Fig. 4. TEM of the DMPC liposomes with (panel A) and without (panel B) CrdS. The lines indicate sizes of 1 µm.

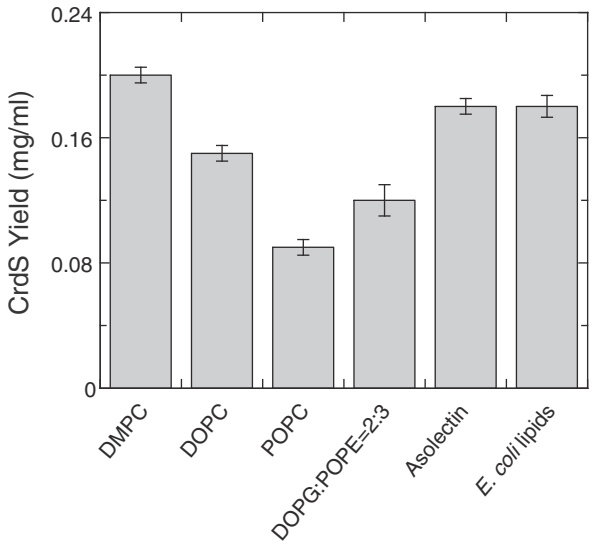

Fig. 5. Yields of CrdS during WG-CFPS with of liposomes prepared from a variety of lipids. CrdS yields are given in mg/ml for liposomes prepared from DMPC (2.5–10 mg/ml), DOPC (2.5 mg/ml), POPC (5 mg/ml), DOPG:POPE = 2:3 ratio by weight (5 mg/ml), asolectin (5 mg/ml) and the total extract of lipids from *E. coli* (5 mg/ml). The numbers in brackets indicate lipid concentrations that were optimal for WG-CFPS. No synthesis occurred with DOPG and DOTAP (data not shown). CrdS quantification was performed using the ImageJ software [27]. The standard errors are shown as vertical bars and were determined from three measurements.

3.7. Reconstitution of CrdS in nanodiscs and purification through SEC

The CrdS protein synthesised in the presence of Brij-58 and purified by IMAC as described above, was reconstituted in the *E. coli* total lipid extract or POPC nanodiscs (Fig. 10). Here, the CrdS:lipid:MSP components were mixed in a 0.5:120:1 molar ratio and following surfactant removal, the self-assembled nanodiscs were purified by SEC on the Superdex 200 column. As indicated in Fig. 10A, both types of CrdS nanodiscs eluted at significantly faster rates than the empty POPC nanodiscs (Fig. 10A), while the remaining MSP protein and other contaminant proteins eluted later (18–23 ml) (Fig. 10A).

To confirm that the CrdS protein successfully reconstituted in the *E. coli* total lipid extract and POPC nanodiscs, the fractions from SEC that eluted between 6 and 9 ml (Fig. 10A) were pooled, concentrated and examined by silver-stained SDS-PAGE (Fig. 10B) coupled with a Western immuno-blot analysis on PVDF membranes (Fig. 10C). As documented in Fig. 10B and C (lanes 2 and 3), the CrdS protein could successfully be detected using both analytical approaches. Notably, the Western immuno-blot analysis operated within a detection limit (Fig. 10C, lanes 2 and 3) using the mouse anti-6xHis monoclonal antibody. This observation suggested that 6xHis tag could be partly obscured after CrdS is reconstituted in nanodiscs. We could also observe that the CrdS proteins reconstituted in the *E. coli* lipids or POPC nanodiscs migrated on the SDS-PAGE gel in a form of diffused bands. These protein bands, which are delineated by two arrowheads (Fig. 10B, and C, lanes 2 and 3) migrated slightly slower than CrdS purified by IMAC (Fig. 10C, lane 1, white arrow). We suggest that these differences in CrdS migration could result from a tight association of CrdS with lipids. Contrary to these specific associations of CrdS with the *E. coli* or POPC lipids, purified CrdS migrated in a form of a sharp protein band in the absence of lipids (Fig. 10C, white arrow). To determine morphological properties of CrdS nanodiscs, they were imaged by TEM prior to SEC. The TEM images of CrdS nanodiscs made from *E. coli* lipids (Fig. 10D, top panel) and POPC (Fig. 10D, bottom panel), indicated that these nanoparticles appeared poly-disperse in nature (Fig. 10D). Although a substantial proportion of both types of

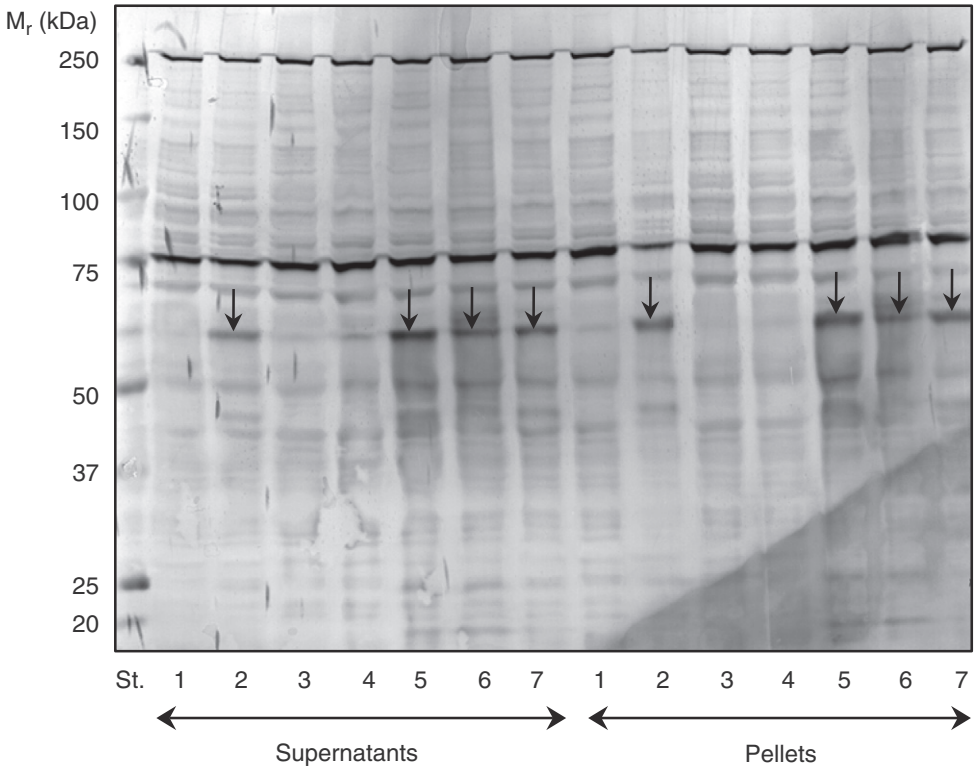

Fig. 6. SDS-PAGE analysis of WG-CFPS translation reactions performed in bilayer mode and supplemented with surfactants. Lane 1 (supernatant and pellet fractions) contains reactions lacking mRNA. Lanes 2–7 (supernatant and pellet fractions) represent the His-TEV-CrdS mRNA reactions in the presence of digitonin, DM, DDM, Brij-58, Tween 80 and Triton X-100. The concentrations of surfactants used in WG-CFPS are listed in Table 2. Black arrows point to highest yields of synthesised CrdS. St. indicates molecular mass standards.

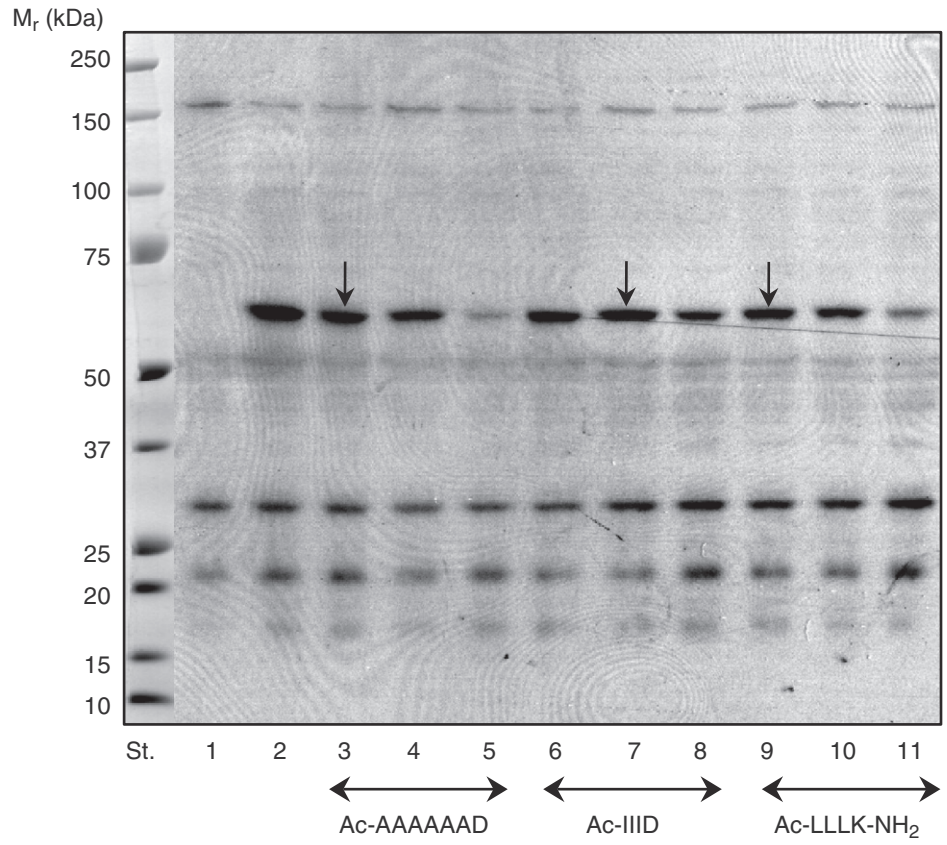

Fig. 7. Anti-CrdS antibody Western immuno-blot analysis of WG-CFPS translation reactions performed in bilayer mode and supplemented with surfactant peptides. Lanes 1 and 2 represent reactions lacking mRNA, and with His-TEV-CrdS mRNA and 0.04% (w/v) Brij-58, respectively. Lanes 3–5, 6–8 and 9–11 contain the His-TEV-CrdS mRNA reactions in the presence of 1 mM, 2 mM and 4 mM Ac-AAAAAAD, 1 mM, 2 mM and 4 mM Ac-IIID and 1 mM, 2 mM and 4 mM Ac-LLLK-NH_2, respectively. The black arrows point to highest yields of synthesised CrdS. St. indicates molecular mass standards.

the CrdS nanodiscs was non-clustered, clumps of nanodiscs were also observed (Fig. 10D; white and black arrows in top and bottom panels).

3.8. Characterisation of CrdS nanodiscs by small-angle X-ray scattering using synchrotron radiation

To find out if the SEC-purified CrdS nanodiscs were formed correctly as the bilayer-embedded membrane protein complexes, the purified CrdS nanodiscs were characterised by SAXS (Fig. 11). The SAXS profiles of CrdS reconstituted in the *E. coli* total lipid extract or POPC nanodiscs were typical of those reported for other membrane-inserted proteins in nanodisc bilayer environments. These nanodiscs typically have a characteristic broad maximum at ~0.1 Å that corresponds to the phospholipid bilayer [37,38]. Using an indirect Fourier transformation (IFT) approach [31,39], the scattering density distributions of the protein–lipid complexes were determined (Fig. 11, inset) that provided a real-space representation of the scattering data. The distributions for both CrdS nanodiscs showed alternating positive and negative peaks at short distances (<50 Å), reflecting the complex contrast landscape across the bilayer resulting from the lower scattering length density of the inner alkyl layer relative to solvent (TBS buffer). An extended tail of positive scattering density was observed with the maximum particle diameter (D_{max}) approaching ~175 Å for both CrdS nanodiscs, indicating that solvent-exposed CrdS extended into solution away from the membrane. These quantitative particle diameter data of both types of CrdS nanodiscs agreed well with those obtained through TEM imaging (*cf.* Figs. 10D and 11). The scattering density distributions suggested that an approximate bilayer width of the purified CrdS nanodiscs was 50 Å. Again, the latter parameter was consistent with the distributions reported in the literature [37,38,40].

3.9. CrdS synthesised with the surfactant peptide Ac-AAAAAAD or reconstituted in the E. coli liposomes exhibits (1,3)-β-D-glucan synthase activity

The CrdS enzyme is believed to operate as the UDP-glucose: (1,3)-β-D-glucan 3-β-D-glucosyltransferase (EC 2.4.1.34). Thus, to find out if CrdS was synthesised in a catalytically active form, (1,3)-β-D-glucan synthase activity assays were carried out. This assay directly evaluates synthesis of the (1,3)-β-D-glucan product, where the formed radioactive product is collected by filtration on Millipore filters and its radioactivity is evaluated by scintillation counting [34]. Because high yields of the CrdS protein were required for these enzyme activity measurements, CrdS was synthesised in the presence of the surfactant Brij-58 and the surfactant peptide Ac-AAAAAAD, or co-translationally inserted in the *E. coli* total lipid extract liposomes, in dialysis mode. A mixed membrane fraction isolated from *S. cerevisiae* and containing a membrane-associated (1,3)-β-D-glucan synthase [33,34], served as a positive control for these (1,3)-β-D-glucan synthase activity measurements.

The data in Table 5 indicated that CrdS synthesised in the presence of Brij-58 was not active, as there was no increase in radioactivity of the (1,3)-β-D-glucan product synthesised from UDP-[^{3}H]-glucose serving as a donor substrate. Similarly, CrdS that was reconstituted in *E. coli* total lipid extract or POPC nanodiscs was found to be catalytically incompetent (Table 5). Conversely, the CrdS proteins synthesised with

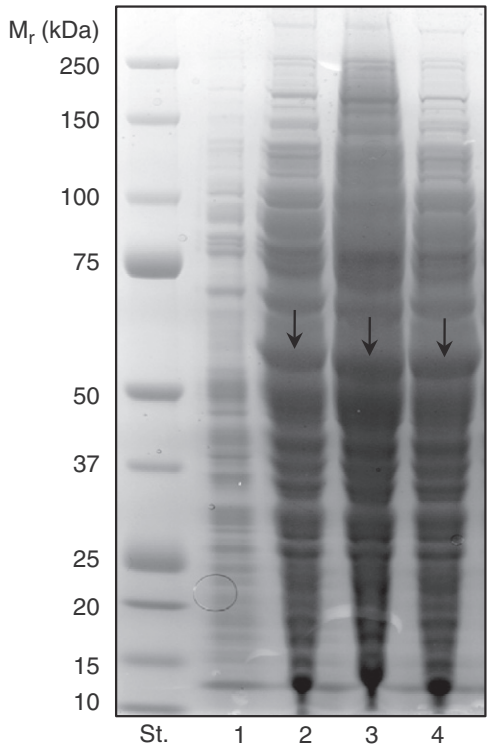

Fig. 8. SDS-PAGE analysis of WG-CFPS translation reactions performed through dialysis mode. Lane 1 represents the reaction lacking mRNA, and lanes 2–4 contain the His-TEV-CrdS mRNA reactions with 0.04% (w/v) Brij-58 after 24 h, 48 h and 72 h, respectively. The black arrows point to synthesised CrdS. St. indicates molecular mass standards.

Table 4
Amino acid sequences of tryptic fragments of CrdS identified by MALDI-TOF/TOF.

CrdS tryptic peptides[a]
SIIAAQAMDYPR
TYCEAVGVNYVTRPDNK
VAVVQTPQFYFNSDPIQHNLGIDK
VFFDVFQPAK
WCLGTIQIGLLR
FGKEEMIGVDFR
ITGLSTENITLAAVPSSSDVKDVFVPEAGWMR

[a] Amino acid sequences are indicated in a 1-letter code.

the surfactant peptide Ac-AAAAAAD or co-translationally inserted in the *E. coli* liposomes, were active (Table 5). The average specific activities, calculated from two independent measurements, were 0.18 mU/mg and 0.22 mU/mg of protein for CrdS synthesised with Ac-AAAAAAD or for CrdS co-translationally inserted in the *E. coli* liposomes, respectively (Table 5). In comparison, the specific activity of (1,3)-β-D-glucan synthase isolated from the *S. cerevisiae* membranes was 1.97 mU/mg protein (Table 5). The latter value was nearly tenfold higher than the specific activities of CF-synthesised CrdS, which was not surprising as the native mixed membrane fractions of *S. cerevisiae* were used for activity measurements.

4. Discussion

Membrane proteins are fundamental to essential cellular functions, yet information on their structural and functional properties is limited. At the end of August 2012, around 355 unique 3D structures of membrane monotopic and polytopic β-barrel and α-helical proteins have been deposited in databases (http://blanco.biomol.

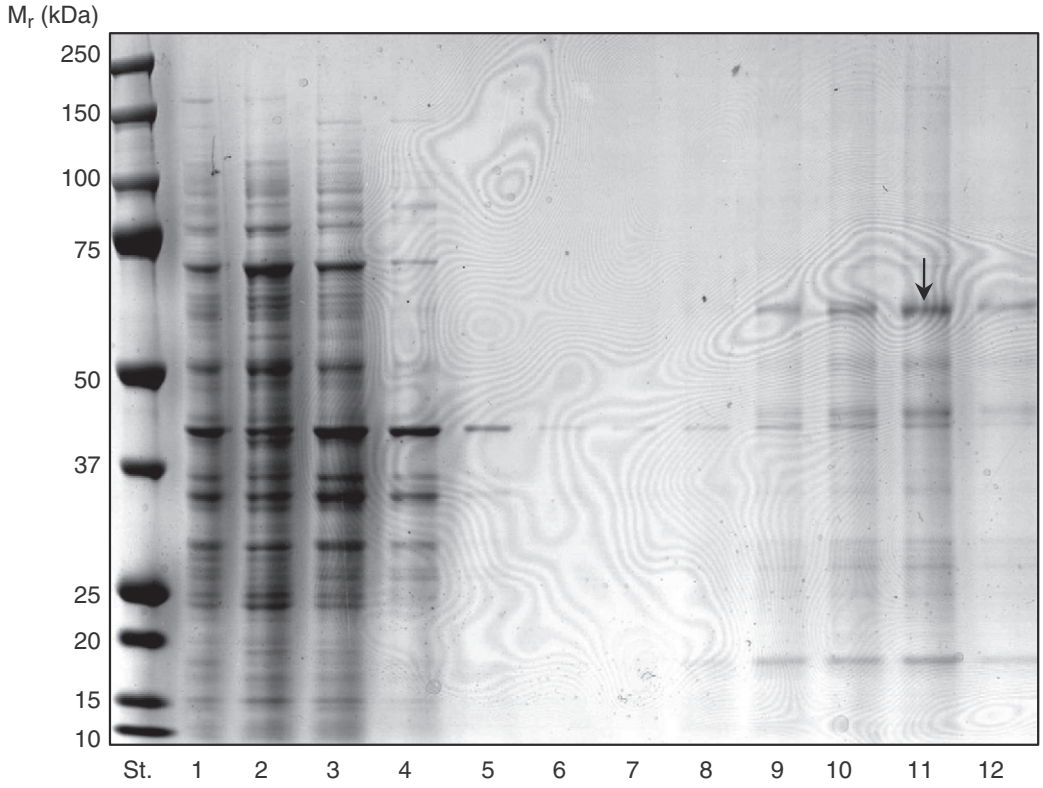

Fig. 9. SDS-PAGE analysis of CrdS purified *via* IMAC in the presence of 0.04% (w/v) Brij-58. Lane 1 contains a crude translation reaction before IMAC. Lane 2 shows unbound components collected as flow-through following incubation of the CFPS reaction with the Ni-NTA beads. Components removed during the 20 mM imidazole washing steps are shown in lanes 3–6. Lanes 7–12 indicate fractions eluted with 50 mM, 100 mM, 150 mM, 200 mM, 250 mM and 500 mM imidazole. Purity of the CrdS preparation shown in lane 11 was estimated to be between 50% and 60%. The black arrow points to purified CrdS. St. indicate molecular mass standards.

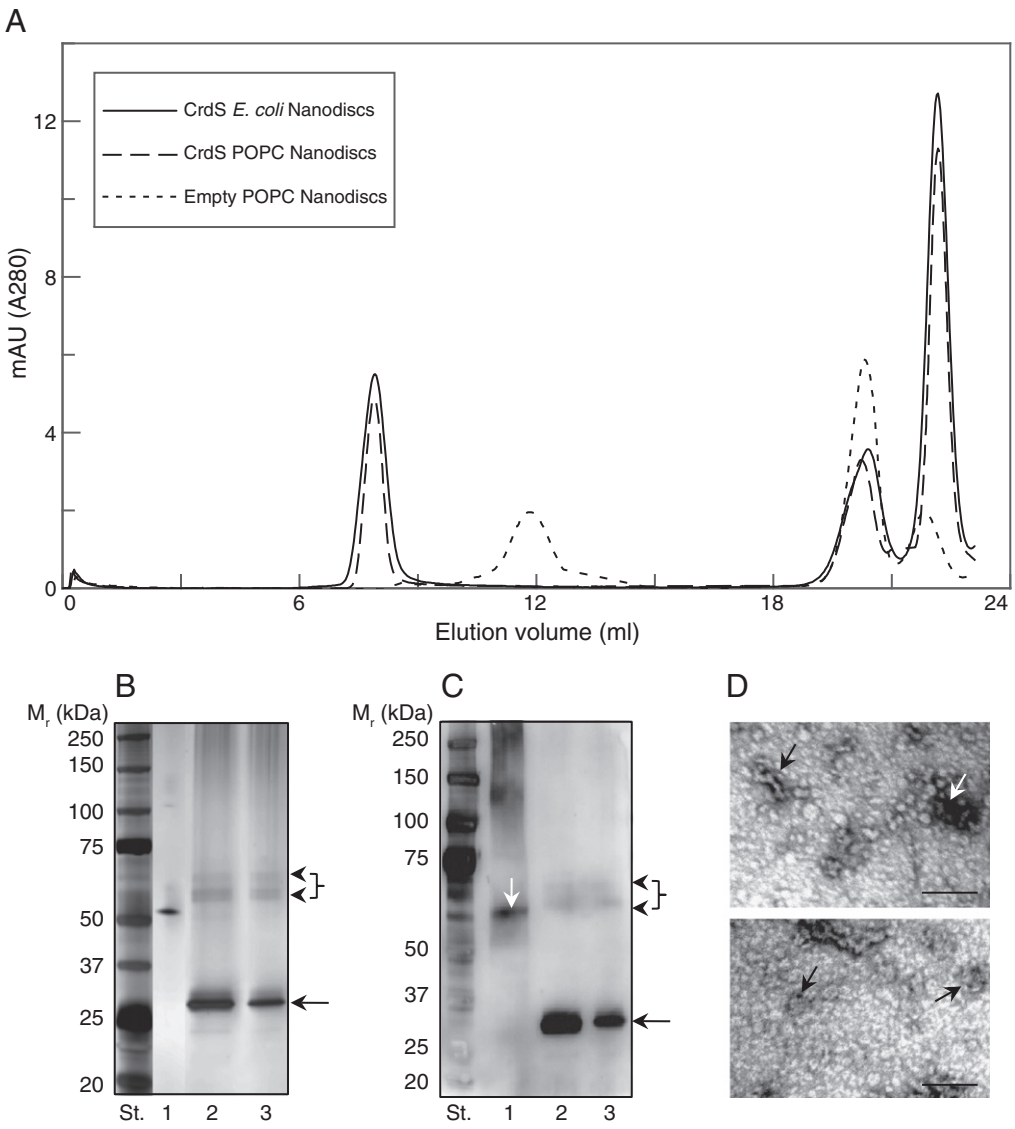

Fig. 10. Reconstitution of CrdS in nanodiscs. Nanodisc assembly (from *Escherichia coli* lipids or POPC and MSP1E3D1) proceeded as described in the Materials and methods section. Panel A, shows an elution profile of the CrdS nanodiscs during SEC on the Superdex 200 10/300 GL column. Full line, dashed and dotted traces indicate elution volumes of the CrdS nanodiscs prepared from the *E. coli* lipids (full line) or POPC (dashed line) and those of POPC empty nanodiscs (dotted line), respectively. In silver-stained SDS-PAGE (panel B), lane 1 contains 75° ng of BSA per lane, and lanes 2 and 3 represent the reconstituted CrdS nanodiscs made from the E. coli lipids and POPC, respectively. The respective top arrowheads and the bottom arrows point to CrdS and MSP1E3D1. A known amount of BSA in lane 1 (75° ng) was used to estimate the protein concentration of CrdS. Panel C, in Western immuno-blot detected with the anti 6xHis antibody, lane 1 contains IMAC-purified CrdS (white arrow), and lanes 2 and 3 represent the reconstituted CrdS nanodiscs made from the *E. coli* lipids and POPC, respectively. The arrowheads, bound by brackets in panels B and C, point to a diffused band of CrdS, respectively. The bottom arrow indicates MSP1E3D1. In panels B and C, St. indicates molecular mass standards. Panel D shows the TEM images of the CrdS nanodiscs made from *E. coli* lipids (top panel) or POPC (bottom panel). White and black arrows show the clustered CrdS nanodiscs. A substantial proportion of CrdS nanodiscs is non-clustered. The lines correspond to 100° nm.

uci.edu/mpstruc/) compared to nearly 84,000 released structures of soluble proteins. The reasons for this low incidence of 3D membrane protein structures compared to those of soluble proteins are many-fold. For example, membrane proteins exist in low abundance and a variety of conceptual difficulties associated with their production and isolation remain unresolved. Although, relatively simple cloning of membrane proteins' cDNA into a diversity of vector systems is prevalent [41–45], membrane proteins' production, purification and crystallisation are less successful and require extensive effort. To this end, the majority of 3D structures of resolved membrane proteins were produced in bacterial hosts, and fewer of them have been obtained in yeast, insect, mammalian cells or through CFPS [10,11].

CFPS systems are an alternative to cell-based systems, the popularity of which started growing only recently with the advent of robotised synthesisers and other technical and conceptual advances [21,22]. An advantage of CFPS is that they allow preparing membrane proteins without residual lipids that are typically co-extracted from membranes and thus researchers can control the lipid composition and environment of synthesised membrane proteins. It has been suggested that the lipid environment around proteins in membranes is responsible for functional modulation of membrane proteins. One of the main CFPS platforms currently used is a eukaryotic wheat germ extract CFPS platform [10–14,17–22], which has been applied in the current work. It has been well documented that WG-CFPS systems enable rapid production of proteins and thus this platform plays an important role in modern functional genomics [10,11,17–22]. This system holds promise in particular for eukaryotic membrane proteins [10,11], as they almost always require post-translational modifications

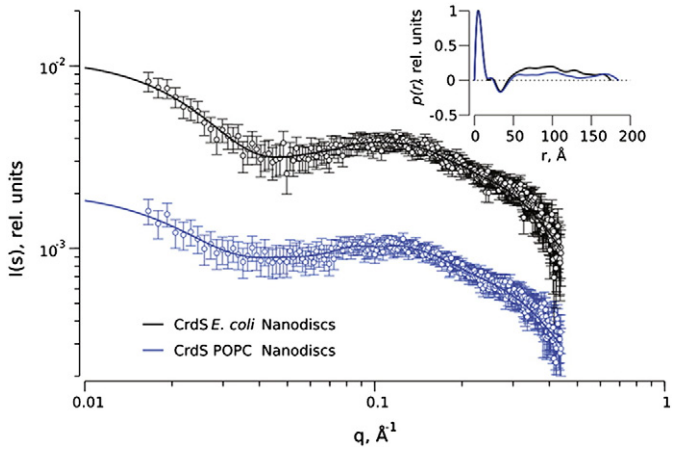

Fig. 11. SAXS of CrdS nanodiscs prepared from the *E. coli* or POPC lipids and MSP1E3D1. The SAXS profiles of the *E. coli* total lipid extract or POPC nanodiscs with reconstituted CrdS are indicated in black or blue circles, respectively. Inset shows regularised curves from the IFT fitting procedure used to generate the real space scattering density distribution functions, p(r). Fits and density distributions of the *E. coli* lipids or POPC nanodiscs with reconstituted CrdS are shown as black and blue solid lines, respectively. The SAXS profiles are offset for clarity.

that can be achieved *via* coupling of CFPS systems with *in-situ* glycosylation, phosphorylation, *etc.*

In the current work, our target CrdS transferase enzyme is confined within cell membranes of *Agrobacterium* sp. [2]. This enzyme is believed to catalyse formation of a (1,3)-β-D-glucan (curdlan) polymer by a repetitive addition of glucosyl residues from the UDP-glucose donor substrate. CrdS as a GT2 family glycosyl transferase enzyme (CAZy database) is clustered with other plant membrane enzymes of paramount significance, such as cellulose, (1,3)-β-D-glucan and (1,3;1,4)-β-D-glucan synthases [2–4]. The CrdS protein harbours seven membrane spanning α-helices, contains a single CM and has a predicted N_{out}–C_{in} topology [2]. Only a few 3D structures of the GT2 enzymes were elucidated up to date, notably all of them by X-ray crystallography [5–7, Polani, Kumaran, Burley and Swaminathan, unpublished data]. However, all these enzymes do not harbour membrane α-helices and essentially embody catalytic modules that fold into α/β architectures [5–7, Polani, Kumaran, Burley and Swaminathan, unpublished data]. Thus, an urgency to resolve a 3D structure of a membrane-associated transferase enzyme in the GT2 family remains.

Our previous attempts to obtain sufficient yield of the full-length CrdS protein in the *E. coli* host for 3D structural, biochemical and biophysical analyses failed [2]. In these experiments we used a variety of bacterial vectors (*e.g.* pET15b, pBAD24, Champion™, pET SUMO™), but irrespective of the conditions, the heterologous expression led to production of truncated forms of CrdS that were produced *via* abortive translation. Hence, in our current study we concentrated our efforts on CFPS of full-length CrdS based on a well-defined wheat germ system, which has been documented to produce sufficient amounts of proteins for both analytical and preparative purposes [10,11,46].

When investigating the initial conditions for WG-CFPS of CrdS, we established that the purities of plasmid DNA fusions, expressed as a A_{260}/A_{280} ratio for transcription reactions (the suitable range is 1.8–2.0), as well as purities of mRNAs for translation reactions (lack of low molecular mass mRNA species of less than 500 bp) were of paramount importance to detect synthesis of full-length CrdS and obtain good yield. We methodically examined the efficiency of WG-CFPS in bilayer and dialysis modes, using a wide range of surfactants, surfactant peptides and amphipols, and of liposomes prepared from a variety of lipids. We found optimal conditions for excellent yield of CrdS in the presence of surfactants, surfactant peptides, and liposomes. The best performing surfactant was with Brij-58, which is considered to be mild, probably owing to its low CMC [47]. On the other hand, the addition of amphipols A8-35 or SMA inhibited WG-CFPS of CrdS. The reason for this inhibitory behaviour of amphipols is not fully understood and could result from either functional de-stabilisation of ribosomes contained in wheat germ, or that amphipols directly interfere with structure of ribosomes and thus CF synthesis. To this end, it has been suggested that A8-35 and sulfonated amphipols may interact with basic patches at surfaces of ribosomal nanoparticles [48].

The CrdS proteins containing 6xHis affinity tag, or 6xHis affinity tag and Factor Xa or TEV proteolytic sites synthesised in WG-CFPS typically migrated around the ranges of 56–60 kDa, though their calculated masses are between 73 and 76 kDa. Although unexpected, our observations with this anomalous migration of membrane CrdS were not unprecedented, since it was previously observed that membrane proteins' band positions do not always correlate with their formula molecular masses [35]. Through tryptic mapping and Mascot database searches, we found out that the generated peptide ions in length of 10–32 amino acid residues, matched perfectly to the putative (1,3)-β-D-glucan synthase catalytic subunit (GenBank accession AF057142). Hence, the MALDI-TOF/TOF MS analysis in conjunction with Western immuno-blot detection unambiguously confirmed that full-length CrdS was synthesised through WG-CFPS.

Excellent yield of CrdS in the presence of artificial liposomes prepared from *E. coli* lipid extract was obtained through WG-CFPS. This high yield was not unexpected as CrdS is a membrane protein of a bacterial origin. It has been estimated that the most abundant phospholipid species (70%) in the inner membrane of *E. coli* is POPE [49]. It consequently seemed logical that the addition of POPE to DOPG, by 3:2 weight ratio leads to CrdS synthesis, while DOPG alone did not support synthesis. Surprisingly, when the liposomes prepared from soybean asolectin lipids were added to CFPS translation reactions, high yield of CrdS was also obtained. It is of note that the soybean (plant) asolectin lipids represent a complex mixture of phospholipids such as lecithin, cephalin and phosphatidylinositol in equal proportions, along with minor amounts of other phospholipids and polar lipids.

To determine the liposome-associated topology of CrdS following co-translational insertion, the CrdS protein was synthesised in the presence of 100 nm DMPC liposomes. We surmised that in these liposomes, CrdS could either adopt N_{out}–C_{in} topology, N_{in}–C_{out} topology or a mixture of both. Here, the N_{out}–C_{in} topology of CrdS was predicted previously through the PRED-TMR algorithm [2,41]. If the N_{out}–C_{in} topology was occurring in the DMPC liposomes, then the NH_2-terminus of the CrdS protein would protrude to the exterior of the liposomes and CM would localise to the liposomal lumen. To this end, the CrdS proteo-liposomes purified through floatation by Accudenz density gradient ultra-centrifugation, were digested with the TEV protease and analysed through a Western immune-blot analysis. When the TEV-treated CrdS proteo-liposomes separated by SDS-PAGE were detected with the anti-6xHis antibody, the reactivity of the TEV-treated CrdS towards this antibody was significantly diminished. Further, the protein band of TEV-treated CrdS on the SDS-PAGE gel shifted to a lower molecular mass and became diffuse (data not

Table 5
(1,3)-β-D-Glucan synthase activity of CrdS prepared through wheat germ cell-free synthesis in the presence of surfactant Brij-58 and surfactant peptide Ac-AAAAAAD, and of CrdS co-translationally inserted in the *E. coli* total lipid extract liposomes, or reconstituted in the *E. coli* total lipid extract and POPC nanodiscs.

Sample	Specific activity (mU/mg protein)[a]
CrdS with Brij-58	0
CrdS with Ac-AAAAAAD	0.18 ± 0.06
CrdS in *E. coli* lipid extract liposomes	0.22 ± 0.05
CrdS in *E. coli* lipid extract nanodiscs	0
CrdS in POPC nanodiscs	0
Mixed membrane fraction of *S. cerevisiae*	1.97 ± 0.07

[a] A mean of two independent measurements.

shown). These observations suggested that in some CrdS molecules, the NH_2-terminus harbouring the 6xHis tag could have been excised by the TEV protease. Thus, in some DMPC liposomes, the NH_2-terminus of CrdS was likely pointing to the exterior of the liposomes, while the other liposomal population contained CrdS in the N_{in}–C_{out} topology. Hence, it can be concluded that CrdS reconstituted in the DMPC liposomes exhibited a random orientation. The possible explanation for this random distribution could be in a diameter (100 nm) and hence high-angle curvature of proteo-liposomes. This curvature could hinder proper insertion of large CM of CrdS into the liposomal lumen, whereas larger diameter proteo-liposomes may be conducive to the correct N_{out}–C_{in} topology of CrdS.

Recombinant CrdS synthesised with the Ac-AAAAAAD surfactant peptide or co-translationally inserted in the *E. coli* lipid extract liposomes was found to be active. On the other hand, CrdS synthesised with Brij-58 or reconstituted in the *E. coli* lipids and POPC nanodiscs was inactive. The latter observation indicates that the CrdS protein synthesised with the surfactant Brij-58 may not have been properly folded and also that reconstitution of CrdS in nanodiscs could not restore CrdS's catalytic activity. However, the observation that CrdS synthesised with the surfactant peptide Ac-AAAAAAD was active, may suggest that surfactant peptides could self-assemble to form a belt surrounding membrane proteins leading to formation of a stable surfactant peptide-membrane protein complex [50]. To find out if the radioactive material synthesised by CrdS (and by the mixed membrane fractions of *S. cerevisiae*) produced the (1,3)-β-D-glucan polymer, the radioactive material was hydrolysed by the (1,3)-β-D-exo-glucanase enzyme that is known to hydrolyse (1,3)-β-D-glucan through an exo-hydrolytic mechanism to glucose [33,34]. Gratifyingly, we found that the radioactivity incorporated in the (1,3)-β-D-glucan product had decreased in all cases by approximately 60% by the (1,3)-β-D-exo-glucanase treatment, indicating that a substantial proportion of the material synthesised by CrdS corresponded to the (1,3)-β-D-glucan product. Conversely, the treatment with a boiled (1,3)-β-D-exo-glucanase or α-amylase left the radioactivity incorporated in the (1,3)-β-D-glucan product unchanged, again confirming the chemical identity of the synthesised product.

Reconstitution of membrane proteins in nanodiscs, pioneered by Sligar and co-workers has been described with membrane proteins of various lengths [23,24,51,52]. The advantage of this technique is generation of homogenous nanoscale lipid bilayers, which enclose a desired membrane protein that is exposed to aqueous environments on both sides. These nanodiscs can then be subjected to biophysical, enzymatic and structural investigations. These nanoscale particles can be effortlessly handled similar to soluble proteins, as their membrane components are shielded by the lipid bilayer milieu, although, specific challenges during nanodiscs construction remain. To this end, the bottleneck represents a gentle isolation or production of a specific membrane protein that can be obtained from biological sources, or expressed and synthesised.

To reconstitute the CrdS protein in nanodiscs, firstly CrdS had to be synthesised in the presence of a mild surfactant Brij-58 in high yield and purified by IMAC. We estimated that nearly 90% of CrdS could be recovered by this purification technique. Subsequently, the surfactant-solubilised CrdS protein was subjected to spontaneous assembly with MSP1E3D1 and either the *E. coli* lipids or a zwitterionic POPC lipid, resulting in spontaneous formation of CrdS:lipid:MSP nanodiscs. The CrdS-containing nanodiscs were then purified by SEC to near homogeneity and both SDS-PAGE and Western immuno-blot analyses indicated the presence of CrdS in these artificial bilayers (Fig. 10). When the CrdS-containing nanodiscs were subjected to SDS-PAGE, the CrdS protein migrated slightly slower than CrdS purified by IMAC, most likely due to associations of CrdS with lipids. These data also indicated that the CrdS protein bound lipid molecules tightly and that the presence of SDS could not entirely abolish these protein–lipid associations. The precise reasons, why CrdS nanodiscs eluted near the void volume during SEC are at present not known. We suggest that at least two factors may play a role. More precisely, the CrdS protein, after assembling in nanodiscs, could cause formation of asymmetrical particles. This could be due to occurrence of a large catalytic module and a COOH-terminal extension being positioned on one side of the nanodisc bilayer, while the other side of the bilayer contains short loops inter-connecting individual α-helices [2]. Second, CrdS nanodiscs could form clusters of aggregated or stacked particles, formation of which could be mediated by Brij-58 that remains to be tightly associated with the CrdS protein during CFPS.

The CrdS-loaded nanodiscs purified by SEC were characterised by SAXS. Our experimental SAXS data were found to be consistent with membrane insertion of the CrdS protein into the bilayer of both *E. coli* lipids- and POPC-formed nanodiscs. The SAXS data provided evidence that CrdS nanodiscs have been formed [37,38,40] and gave us confidence to reconstitute CrdS in these bilayers for future, more detailed structural studies. Future work will focus on parameter extraction and modelling from samples at higher concentrations, particularly in the differentiation of empty and CrdS-loaded nanodiscs, and in separation of protein and lipidic scattering *via* contrast variation in small-angle neutron scattering experiments. Future work will also expand upon the initial studies presented in our current work, and explore in-depth bilayer insertion and membrane perturbation caused by CrdS in nanodiscs formed from the *E. coli* lipids and POPC, and from a variety of other lipids.

Finally, meaningful studies of polysaccharide synthases such as CrdS are rare [53] and progress on structural descriptions of β-D-glucan synthases has been slow-moving [3]. This is particularly accurate for synthases of the GT2 family, which contains enzymes required for the synthesis of polysaccharides such as cellulose, (1,3)- and (1,3;1,4)-β-D-glucans [2,3]. It has proved problematic to purify these enzymes from nearly any biological material [2,3], because of a membrane location of these polysaccharide synthases, their low concentration in cellular tissues and a tendency to lose enzyme activity following tissue disruption and isolation. For these reasons, CFPS systems using cDNA fusions offer an alternative route to prepare sufficient amounts of polysaccharide synthases for structural, physicochemical, kinetic and substrate specificity studies.

5. Conclusions

A set of suitable procedures based on WG-CFPS has been developed leading to high yield of an integral membrane CrdS enzyme from *Agrobacterium* sp. that is classified by the Enzyme Commission as UDP-glucose: (1,3)-β-D-glucan 3-β-D-glucosyltransferase (EC 2.4.1.34). Here, we synthesised full-length CrdS as evidenced by MALDI-TOF/TOF MS, from the pEU-EO1™ plasmids, containing a 6xHis affinity tag and either Factor Xa or TEV proteolytic sites. CFPS afforded good yield of CrdS with a variety of surfactants, surfactant peptides and liposomes through bilayer and dialysis modes. The dialysis mode with the surfactant Brij-58 afforded between 1 and 2 mg/ml quantities of CrdS. IMAC purified CrdS synthesised with Brij-58 was assembled in the *E. coli* lipids or POPC nanodiscs. CrdS synthesised in the presence of the surfactant peptide Ac-AAAAAAD and co-translationally inserted in the *E. coli* liposomes was catalytically competent. We expect that these rapid and efficient WG-CFPS procedures could be used for generation of other membrane catalysts, particularly where large quantities of proteins are required for downstream functional, structural and other applications.

Funding source

This work was supported by the DP120100900 and LP120100201 grants from the Australian Research Council to MH.

Acknowledgements

We are grateful to Dr Leanne Kelly and Dr Gwenda Mayo (Australian Centre for Plant Functional Genomics) for MALDI-TOF/TOF MS and TEM

analyses, respectively. Ramya Sampath is thanked for technical support. Dr Timothy Knowles (University of Birmingham, UK) is acknowledged for providing SMA. Financial support from the Australian Synchrotron Research Program is funded by the Commonwealth of Australia and access to the SAXS/WAXS beamline is also acknowledged.

References

[1] S.J. Stasinopoulos, P.R. Fisher, B.A. Stone, V.A. Stanisich, Detection of two loci involved in (1→3)-β-glucan (curdlan) biosynthesis by *Agrobacterium* sp. ATCC31749, and comparative sequence analysis of the putative curdlan synthase gene, Glycobiology 9 (1999) 31–41.
[2] M. Hrmova, B.A. Stone, G.B. Fincher, High-yield production, refolding and molecular modelling of the catalytic module of (1,3)-β-D-glucan (curdlan) synthase from *Agrobacterium* sp, Glycoconj. J. 27 (2010) 461–476.
[3] B.A. Stone, A.K. Jacobs, M. Hrmova, R.A. Burton, G.B. Fincher, The biosynthesis of plant cell wall and related polysaccharides by enzymes of the GT2 and GT48 families, in: P. Ulvskov (Ed.), Plant Polysaccharides Series: Annual Plant Reviews, 41, Blackwell Publishing, Danvers, 2011, pp. 109–166.
[4] B.L. Cantarel, P.M. Coutinho, C. Rancurel, T. Bernard, V. Lombard, B. Henrissat, The Carbohydrate-Active enZymes database (CAZy): an expert resource for glycogenomics, Nucleic Acids Res. 37 (2009) D233–D238.
[5] S.J. Charnock, G.J. Davies, Structure of the nucleotide-diphospho-sugar transferase, SpsA from *Bacillus subtilis*, in native and nucleotide-complexed forms, Biochemistry 18 (1999) 6380–6385.
[6] T. Osawa, N. Sugiura, H. Shimada, R. Hirooka, A. Tsuji, T. Shirakawa, K. Fukuyama, M. Kimura, K. Kimata, Y. Kakuta, Crystal structure of chondroitin polymerase from *Escherichia coli* K4, Biochem. Biophys. Res. Commun. 378 (2009) 10–14.
[7] A.L. Lovering, L.Y. Lin, E.W. Sewell, T. Spreter, E.D. Brown, N.C. Strynadka, Structure of the bacterial teichoic acid polymerase TagF provides insights into membrane association and catalysis, Nat. Struct. Mol. Biol. 17 (2010) 582–589.
[8] E.J. Stewart, F. Aslund, J. Beckwith, Disulfide bond formation in the *Escherichia coli* cytoplasm: an *in vivo* role reversal for the thioredoxins, EMBO J. 17 (1998) 5543–5550.
[9] Y. Tsunoda, N. Sakai, K. Kikuchi, Improving expression and solubility of rice proteins produced as fusion proteins in *Escherichia coli*, Protein Expr. Purif. 42 (2005) 268–277.
[10] A.S. Spirin, J.R. Swartz, Cell-free protein synthesis, Methods and Protocols, Wiley-VCH Verlag, Weinheim, 2008.
[11] N. Farrokhi, M. Hrmova, R.A. Burton, G.B. Fincher, Heterologous and cell free expression systems, in: D. Somers, P. Langridge, P. Gustafson (Eds.), Plant genomics, Meth. Mol. Biol., 513, Humana Press Inc., Totowa, 2009, pp. 175–198.
[12] F. Katzen, G. Chang, W. Kudlicki, The past, present and future of cell-free protein synthesis, Trends Biotechnol. 23 (2005) 150–156.
[13] S. Wagner, M.L. Bader, D. Drew, J.-W. de Gier, Rationalizing membrane protein overexpression, Trends Biotechnol. 24 (2006) 364–371.
[14] L. Liguori, B. Marques, A. Villegas-Mendez, R. Rothe, J.L. Lenormand, Production of membrane proteins using cell-free expression systems, Expert Rev. Proteomics 4 (2007) 79–90.
[15] D.F. Savage, C.L. Anderson, Y. Robles-Colmenares, Z.E. Newby, R.M. Stroud, Cell-free complements *in vivo* expression of the *E. coli* membrane proteome, Protein Sci. 16 (2007) 966–976.
[16] D. Schwarz, V. Dötsch, F. Bernhard, Production of membrane proteins using cell-free expression systems, Proteomics 8 (2008) 3933–3946.
[17] F. Junge, S. Haberstock, C. Roos, S. Stefer, D. Proverbio, V. Dötsch, F. Bernhard, Advances in cell-free protein synthesis for the functional and structural analysis of membrane proteins, New Biotechnol. 28 (2011) 262–271.
[18] F. Junge, B. Schneider, S. Reckel, D. Schwarz, V. Dotsch, F. Bernhard, Large-scale production of functional membrane proteins, Cell. Mol. Life Sci. 65 (2008) 1729–1755.
[19] A.S. Spirin, V.I. Baranov, L.A. Ryabova, S.Y. Ovodov, Y.B. Alakhov, A continuous cell-free translation system capable of producing polypeptides in high yield, Science 242 (1988) 1162–1164.
[20] K. Madin, T. Sawasaki, T. Ogasawara, Y. Endo, A highly efficient and robust cell-free protein synthesis system prepared from wheat embryos: plants apparently contain a suicide system directed at ribosomes, Proc. Natl. Acad. Sci. U.S.A. 97 (2000) 559–564.
[21] D.A. Vinarov, C.L.L. Newman, J.L. Markley, Wheat germ cell-free platform for eukaryotic protein production, FEBS J. 273 (2006) 4160–4416.
[22] M. Aoki, T. Matsuda, Y. Tomo, Y. Miyata, M. Inoue, T. Kigawaa, S. Yokoyama, Automated system for high-throughput protein production using the dialysis cell-free method, Protein Expr. Purif. 68 (2009) 128–136.
[23] T.H. Bayburt, Y.V. Grinkova, S.G. Sligar, Self-assembly of discoidal phospholipid bilayer nanoparticles with membrane scaffold proteins, Nano Lett. 2 (2002) 853–856.
[24] I.G. Denisov, Y.V. Grinkova, A.A. Lazarides, S.G. Sligar, Directed self-assembly of monodisperse phospholipid bilayer nanodiscs with controlled size, J. Am. Chem. Soc. 126 (2004) 3477–3487.
[25] H.D.T. Mertens, D.I. Svergun, Structural characterization of proteins and complexes using small-angle X-ray solution scattering, J. Struct. Biol. 172 (2010) 128–141.
[26] T. Sawasaki, Y. Hasegawa, M. Tsuchimochi, N. Kamura, T. Ogasawara, T. Kuroita, Y. Endo, Bilayer cell-free protein synthesis system for high-throughput screening of gene products, FEBS Lett. 514 (2010) 102–105.
[27] M.D. Abramoff, P.J. Magalhaes, S.J. Ram, Image processing with ImageJ, Biophotonics Int. 11 (2004) 36–42.
[28] J.E. Tropea, S. Cherry, D.S. Waugh, Expression and purification of soluble His_6-tagged TEV protease, Meth. Mol. Biol. 498 (2009) 297–307.
[29] F.J.D. Alvarez, C. Orelle, A.L. Davidson, Functional reconstitution of an ABC transporter in nanodiscs for use in electron paramagnetic resonance spectroscopy, J. Am. Chem. Soc. 132 (2010) 9513–9515.
[30] M.V. Petoukhov, D. Franke, A.V. Shkumatov, G. Tria, A.G. Kikhney, M. Gajda, C. Gorba, H.D.T. Mertens, P.V. Konarev, D.I. Svergun, New developments in the ATSAS program package for small-angle scattering data analysis, J. Appl. Crystallogr. 45 (2012) 342–350.
[31] D.I. Svergun, Determination of the regularization parameter in indirect-transform methods using perceptual criteria, J. Appl. Crystallogr. 25 (1992) 495–503.
[32] R.B. Kapust, J. Tözsér, J.D. Fox, D.E. Anderson, S. Cherry, T.D. Copeland, D.S. Waugh, Tobacco Etch Virus protease: mechanism of autolysis and rational design of stable mutants with wild-type catalytic proficiency, Protein Eng. 14 (2001) 993–1000.
[33] E.M. Shematek, J.A. Braatz, E. Cabib, E. Biosynthesis, Biosynthesis of the yeast cell wall. I. Preparation and properties of (1,3)-β-glucan synthetase, J. Biol. Chem. 255 (1980) 888–894.
[34] M. Hrmova, C.S. Taft, C.P. Selitrennikoff, (1,3)-β-D-Glucan synthase of *Neurospora crassa*: partial purification and characterization of solubilized enzyme activity, Exp. Mycol. 13 (1989) 129–139.
[35] A. Rath, M. Glibowicka, V.G. Nadeau, G. Chen, C.M. Deber, Detergent binding explains anomalous SDS-PAGE migration of membrane proteins, Proc. Natl. Acad. Sci. U.S.A. 106 (2009) 1760–1765.
[36] A. Nozawa, T. Ogasawara, S. Matsunaga, T. Iwasaki, T. Sawasaki, Y. Endo, Production and partial purification of membrane proteins using a liposome-supplemented wheat cell-free translation system, BMC Biotechnol. 11 (2011) 35–44.
[37] I.G. Denisov, M.A. McLean, A.W. Shaw, Y.V. Grinkova, S.G. Sligar, Thermotropic phase transition in soluble nanoscale lipid bilayers, J. Phys. Chem. B 109 (2004) 15580–15588.
[38] B.J. Baas, I.G. Denisov, S.G. Sligar, Homotropic cooperativity of monomeric cytochrome P450 3A4 in a nanoscale native bilayer environment, Arch. Biochem. Biophys. 430 (2004) 218–228.
[39] O. Glatter, A new method for the evaluation of small-angle scattering data, J. Appl. Crystallogr. 10 (1977) 415–421.
[40] N. Skar-Gislinge, J.B. Simonsen, K. Mortensen, R. Feidenhans, S.G. Sligar, B.L. Møller, T. Bjørnholm, L. Arleth, Elliptical structure of phospholipid bilayer nanodiscs encapsulated by scaffold proteins: casting the roles of the lipids and the protein, J. Am. Chem. Soc. 132 (2010) 13713–13722.
[41] C. Pasquier, V.J. Promponas, G.A. Palaios, J.S. Hamodrakas, A novel method for predicting transmembrane segments in proteins based on a statistical analysis of the SwissProt database: the PRED-TMR algorithm, Protein Eng. 12 (1999) 381–385.
[42] G.S. Waldo, B.M. Standish, J. Berendzen, T.C. Terwilliger, Rapid protein-folding assay using green fluorescent protein, Nat. Biotechnol. 17 (1999) 691–695.
[43] D. Drew, S. Newstead, Y. Sonoda, H. Kim, G. von Heijne, S. Iwata, GFP-based optimization scheme for the overexpression and purification of eukaryotic membrane proteins in *Saccharomyces cerevisiae*, Nat. Protoc. 3 (2008) 784–798.
[44] J.M. Hsieh, G.M. Besserer, M.G. Madej, H.-Q. Bui, S. Kwon, J. Abramson, Bridging the gap: a GFP-based strategy for overexpression and purification of membrane proteins with intra and extracellular C-termini, Protein Sci. 19 (2010) 868–880.
[45] K. Mizutani, S. Yoshioka, Y. Mizutani, S. Iwata, B. Mikami, High-throughput construction of expression system using yeast *Pichia pastoris*, and its application to membrane proteins, Protein Expr. Purif. 77 (2011) 1–8.
[46] A. Deniaud, L. Liguori, I. Blesneac, J.L. Lenormand, E. Pebay-Peyroula, Crystallisation of the membrane protein hVDAC1 produced in cell-free system, Biochim, Biophys. Acta - Biomembranes 1798 (2010) 1540–1546.
[47] L. Isaksson, J. Enberg, R. Neutze, B.G. Karlsson, A. Pedersen, Expression screening of membrane proteins with cell-free protein synthesis, Protein Expr. Purif. 82 (2012) 218–225.
[48] P. Bazzacco, E. Billon-Deni, S. Sharma, L.J. Catoire, S. Mar, C. Le Bon, E. Point, J.-L. Banères, G. Durand, F. Zito, B. Pucci, J.-L. Popot, Nonionic homopolymeric amphipols: application to membrane protein folding, cell-free synthesis, and solution nuclear magnetic resonance, Biochemistry 51 (2012) 1416–1430.
[49] N. Dowhan, Molecular basis for membrane phospholipid diversity, why are there so many lipids? Annu. Rev. Biochem. 66 (1997) 199–232.
[50] X. Zhao, Y. Nagai, P.J. Reeves, P. Kiley, H.G. Khorana, S. Zhang, Designer peptide surfactants stabilize diverse functional membrane proteins, Chem. Soc. Rev. 41 (2012) 1721–1728.
[51] R. Yan, X. Mo, A.M. Paredes, K. Dai, F. Lanza, M.A. Cruz, R. Li, Reconstitution of the platelet glycoprotein Ib-IX complex in phospholipid bilayer nanodiscs, Biochemistry 50 (2011) 10598–10606.
[52] M.T. Marty, A. Das, S.G. Sligar, Ultra-thin layer MALDI mass spectrometry of membrane proteins in nanodiscs, Anal. Bioanal. Chem. 402 (2012) 721–729.
[53] Y. Ihara, T. Takeda, F. Sakai, Y. Hayashi, Transferase activity of GhCesA2 (putative cotton cellulose 4-β-glucosyltransferase) expressed in *Pichia pastoris*, J. Wood Sci. 48 (2002) 425–428.

Statement of Authorship

Title of the paper	Molecular Function of a Plant Anion-Permeable Efflux Transporter Involved in Boron-Toxicity Tolerance
Publication status	Publication style

Authors Contribution

By signing the Statement of Authorship, each author certifies that their stated contribution to the publication is accurate and that permission is granted for the publication to be included in the candidate's thesis

Name of Principal Author (Candidate)	Yagnesh Nagarajan
Contribution to the paper	Designed ,performed experiments, analysed data and wrote paper
Signature	Date 18/12/14

Name of Co-Author	Jay Rongala
Contribution to the paper	Designed and performed experiments
Signature	Date 18/12/2014.

Name of Co-Author	Nadim Shadiac
Contribution to the paper	Assisted with experiments
Signature	Date 18/12/14

Name of Co-Author	Julie Hayes
Contribution to the paper	Performed and analysed *Xenopus Oocyte* experiments
Signature	Date 18/12/14

Name of Co-Author	Tim Sutton
Contribution to the paper	Designed and assisted with analysing the experiments
Signature	Date 18/12/14

Name of Co-Author	Matthew Gilliham
Contribution to the paper	Designed and assisted with analysing the experiments
Signature	Date 18-12-14

Name of Co-Author	Stephen D. Tyerman
Contribution to the paper	Designed and assisted with analysing the experiments
Signature	Date 18/12/14

Name of Co-Author	Gordon McPhee
Contribution to the paper	Performed, analysed AFM experiments and wrote paper
Signature	Date 18/12/14

Name of Co-Author	Nicolas H. Voelcker
Contribution to the paper	Designed, analysed AFM experiments and wrote paper
Signature	Date 18/12/14

Name of Co-Author	Haydyn D. T. Mertens
Contribution to the paper	Designed, performed, analysed SAXS experiments and wrote paper
Signature	Date 18/12/14

Name of Co-Author	Nigel M. Kirby
Contribution to the paper	Designed, performed and analysed SAXS experiments
Signature	Date 18/12/14

Name of Co-Author	Jung-Goo Lee
Contribution to the paper	Designed and performed quantum mechanical model
Signature	Date 18-12-14

Name of Co-Author	Yaroslava G. Yingling
Contribution to the paper	Designed and performed quantum mechanical model
Signature	Date 18-12-14

Name of Co-Author	Maria Hrmova
Contribution to the paper	Designed, analysed and wrote paper
Signature	Date 18-12-2014

Chapter 3

MOLECULAR FUNCTION OF A PLANT ANION-PERMEABLE EFFLUX TRANSPORTER INVOLVED IN BORON-TOXICITY TOLERANCE

Yagnesh Nagarajan[a], Jay Rongala[a], Nadim Shadiac[a], Julie Hayes[a], Tim Sutton[a], Matthew Gilliham[b], Stephen D. Tyerman[b], Gordon McPhee[c], Nicolas H. Voelcker[c], Haydyn D. T. Mertens[d,1], Nigel M. Kirby[d], Jung-Goo Lee[e], Yaroslava G. Yingling[e], and Maria Hrmova[a,2]

[a] Australian Centre for Plant Functional Genomics, School of Agriculture, Food and Wine, University of Adelaide, Glen Osmond, SA 5064, Australia.
[b] ARC Centre of Excellence in Plant Energy Biology, School of Agriculture, Food and Wine, University of Adelaide, Glen Osmond, SA 5064, Australia.
[c] Mawson Institute, University of South Australia, Mawson Lakes, SA 5095, Australia.
[d] Australian Synchrotron, SAXS/WAXS Beamline, Clayton, Victoria 3168, Australia.
[e] Department of Materials Science and Engineering, North Carolina State University, Raleigh, NC 27695-7907, USA.

[1]Current address: BIOSAXS Group, EMBL Hamburg, Hamburg, 22603, Germany.

[2]Address correspondence to **maria.hrmova@adelaide.edu.au**

ABSTRACT

High boron concentrations in soils represent an ecological constraint that restricts crop yields worldwide. Plant membrane transport proteins are fundamental to controlling tolerance of genotypes to high boron, but their three-dimensional structures are unavailable. In barley, the root anion-permeable transporter HvBot1 plays a key role in boron tolerance, facilitating the efflux of borate anions from cells. Here, we describe structural and functional features of HvBot1 using combined *in silico* and *in vitro* approaches. Molecular modelling reveals that HvBot1 is comprised of 13 membrane-spanning and five cytoplasmic α-helices, the latter facilitating oligomerisation. We predict trimeric supra-molecular assembly of HvBot1 and allocate a Na^+-binding site to the proximity of a central pore that may be involved in conducting a variety of anions. Using a wheat germ cell-free synthesis system we synthesize full-length HvBot1 and co-translationally insert it into liposomes to demonstrate *via* patch-

clamp electrophysiology that HvBot1 mediates Na^+-dependent anion transport and exhibits channel-like characteristics. Small-angle X-ray scattering demonstrates that the thickness of HvBot1 liposomes is locally perturbed and atomic force microscopy reveals that HvBot1 protrudes 17 Å above the bilayer surface. Our combined methods offer a proof-of-principle approach for molecular descriptions of permeation mechanisms that underlie plant transporter function.

INTRODUCTION

Plant transporters facilitating borate anions $[B(OH)_4]^-$ efflux are classified in the 2.A.31 Anion Exchanger (AE) family, together with distant orthologs of mammalian and yeast carriers (Saier et al., 2014). Plant members of the AE family play important roles in tolerance to both high and low boron concentrations in soils (Takano et al., 2002; Nakagawa et al., 2007; Sutton et al., 2007; Pallotta et al., 2014). For example, under conditions of limited boron supply to *Arabidopsis*, the transporter AtBor1 is expressed specifically on the inner plasma membrane of pericycle and endodermal cells of the root, exporting boron to the xylem for transfer to shoots (Takano et al., 2010). Similarly, rice OsBor1 is required for both efficient boron uptake and xylem loading (Nakagawa et al., 2007). Furthermore, in barley, HvBot1 is highly expressed in roots of boron toxicity-tolerant genotypes (Sutton et al., 2007; Reid, 2007) facilitating the efflux of borate anions from root cells. Despite a net boron concentration gradient directed into root cells, there is a favourable outwardly-directed electrochemical gradient for borate anions that counteracts accumulation of boron in roots, thus reducing boron transport to the above-ground parts of the plant (Hayes and Reid, 2004). When AtBor1, OsBor1 and HvBot1 are expressed in *Saccharomyces cerevisiae*, they all confer tolerance to high boron and reduce yeast intracellular concentrations (Takano et al., 2002; Nakagawa et al., 2007; Sutton et al., 2007). In barley roots, efflux of borate anions can be reduced by anion channel inhibitors. Borate anion efflux is pH-dependent, where its mechanism is lost at pH values approaching the pK_a value of boric acid (9.24) (Hayes and Reid, 2004). These observations are consistent with HvBot1 operating as a borate anion-permeable transporter. Two alternative models for efflux of borate anions, based either on an anion channel or anion exchange mechanism, have been suggested for HvBot1 (Hayes and Reid, 2004). Another member of the AE 2.A.31 family, mammalian NaBC1 functions as an electrogenic voltage-regulated and Na^+-coupled borate anion transporter (Park et al., 2004), while YNL275w from *S. cerevisiae* transports HCO_3^-, Cl^-, I^-, Br^-, NO_3^- and borate anions

(Zhao and Reithmeier, 2001; Jennings et al., 2007). Mechanistic explanations for some AE 2.A.31 family members have been offered (Boron et al., 2009), but it is not known if uniport, anion/anion (other than borate) antiport, or anion/cation symport account for permeation in plant borate transporters.

The structural properties and underlying molecular mechanisms of the plant members of AE 2.A.31 transporters, such as HvBot1, have not been described due to the challenges of producing folded plant membrane proteins (Shadiac et al., 2013). Here, we carried out *in silico* structural predictions and *in vitro* functional analyses using co-translational insertion of HvBot1 into liposomes *via* Wheat Germ Cell-Free Protein Synthesis (WG-CFPS). Based on our data we suggest that HvBot1 should be designated as a channel-like Na^+-dependent anion transporter with high affinity to borate anions.

RESULTS

In silico predictions reveal the complex structure of HvBot1

To gain insights into the structural framework of plant members of the AE 2.A.31 family, we constructed *in silico* a three-dimensional (3D) model of HvBot1 (GenBank accession ABS83562.1) consisting of 574 residues. The details of model construction and its evaluation are described in Supplementary Information. The HvBot1 protein forms complex architecture containing individually folded membrane and cytoplasmic α-helical bundles (Figures 1A and 1B). Topological distributions of secondary structures indicate that the N-terminus is exposed to the cell exterior, while the C-terminus is oriented to the cell interior. Notably, nearly all potential phosphorylation sites (16 out of 18) are located on the intracellular side of the structure or on five short intracellular α-helices. Based on the crystal structure of the uracil/H^+ symporter (Lu et al., 2011), identified by I-Tasser (Zhang, 2008) as a distant structural homologue of HvBot1, we were able to assign functional properties to the membrane components of HvBot1. Seven α-helices shape the pore (Figure 1A and 1B, in pink), while six additional α-helices surround the pore-forming α-helices, some of which are kinked (Figures 1A and 1B, in green). In addition to these 13 membrane α-helices, five short α-helices form an independently folded domain that we named “sombrero”, which protrudes from the membrane plane by approximately 17 Å into the cell interior (Figures 1A and 1C). Molecular dynamics (MD) of an 84 ns simulation of the HvBot1 structure in the environment of a dioleoylphosphocholine (DOPC) lipid bilayer (Figure 1C and Supplemental Figure 1)

revealed the presence of a Na^+-binding site that co-localized to the proximity of pore-forming α-helices (Figures 1 and 2, and Supplemental Figure 2A). A close view of the Na^+ ion-binding site indicated that six residues participated in nona-hedral coordination of Na^+. These were N63 (carbonyl O and OD1), T68 (carbonyl O and OG1), E70 (OE1 and OE2), T71 (OG1), Q113 (OE1) and G117 (carbonyl O). While four Na^+-bonding oxygen atoms (N63, OD1; T68, OG1; E70, OE2; T71, OG1) were identified at distances of approximately 2.2 Å to 3.2 Å during the last 52 ns of MD simulation time for the last three oxygen atoms, and during the 34 ns simulation time (from 23 ns to 57 ns) for OD1 of N63, the other five Na^+-bonding partners (N63, carbonyl O; T68, carbonyl O; E70, OE1; Q113, OE1; G117, carbonyl O) were at 3.2 Å to 5.6 Å distances during the last 60 ns simulation time (Figure 2) Surface electrostatic potential calculations allocated mostly positively charged patches near the Na^+-binding site, while a lower density of charged regions was observed in membrane-embedded regions (Supplemental Figure 2B).

Functional HvBot1 is produced *in vitro* and *in vivo*

The effectiveness of WG-CFPS to yield HvBot1 *via* co-translational insertion into liposomes was investigated in a de-coupled bilayer mode (Periasamy et al., 2013). The translation reaction was carried out in the presence of a variety of liposomes (Figure 3A and Supplemental Figure 3A), including a mixture of lipids to mimic the composition of a plant membrane (Magdy et al., 1994). SDS-PAGE indicated that HvBot1 was embedded in mono-, di- and tri-meric forms in asolectin liposomes with a yield of 0.16 mg of monomer per ml of a translation reaction mixture (Figure 3A, and Supplemental Figures 3A and 3C). On the other hand, blue native PAGE revealed the presence of trimeric HvBot1 only (Figure 3A). We also examined synthesis in the presence of mild surfactants Brij58, digitonin and Tween 80, and acetylated surfactant peptides, which led to similar yields of monomeric HvBot1, but to lower yields of oligomeric forms, while surfactant peptides were detrimental to synthesis of all forms of HvBot1 (Supplemental Figures 3B and 3D). Given that the incorporation of membrane proteins in liposomes cannot be mediated by a translocon (the protein-conducting channel) (White and von Heijne, 2004), it is evident that the presence of trace amounts of native lipids in a WG extract and a close proximity of ribosomes to liposomes are adequate for co-translational insertion. The identity of synthesized HvBot1 was verified through Western immuno-blots (WIB) (Figure 3A and Supplemental Figure 3) and Electrospray

Ionisation Mass Spectrometry to reveal that peptide ions matched those of peptide sequences of HvBot1.

Similar oligomerisation patterns of HvBot1 were observed using a cell-based expression system in *P. pastoris* (Figure 3B). Mono-, di- and tri-meric forms were readily detectable *via* WIB, with trimeric HvBot1 the most abundant (Figure 3B). We confirmed membrane localisation of HvBot1 by confocal imaging of chimeric HvBot1-GFP in *P. pastoris* and in onion epidermal cells that transiently expressed the 35S:HvBot1:GFP construct (Supplemental Figure 4). During SDS-PAGE we observed variation in the mobility of HvBot1 forms derived from WG-CFPS and *P. pastoris* expression, which could be explained by differential solvation of proteins by SDS. This anomaly was not unparalleled (Rath et al., 2009).

As blue native PAGE of co-translationally inserted HvBot1 (Figure 3A) revealed a trimeric form of HvBot1, we predicted *in silico* its quaternary structure (Figure 1E, Supplemental Figure 5 and Supplemental Table 1). Based on the assumption that the membrane-protruding sombrero component and exposed intracellular loops could mediate oligomerisation, we built dimeric D1-D3 and trimeric T1-T3 assemblies (Supplemental Table 1 and Supplemental Figure 5). Evaluations of the total energies (Supplemental Table 1) favoured D3 and T1 as the most likely quaternary structures (Figure 1E and Supplemental Figure 5). Based on our electrophoretic analyses and structural predictions we suggest that trimeric HvBot1 may be functional *in planta*, or that mono-, di- and tri-meric forms may be in a dynamic equilibrium.

Thickness of HvBot1 liposomes is locally perturbed

Insertions of HvBot1 in membrane bilayers of liposomes were analyzed by small-angle X-ray scattering (SAXS), under the solution conditions, using synchrotron radiation, to monitor the local perturbation of the bilayer structure upon WG-CFPS. Modelled bilayer electron density profiles derived from SAXS data (Pabst, 2006) for multilamellar 1,2-dimyristoyl-sn-glycero-3-phosphocholine (DMPC) (Figure 4A) and unilamellar asolectin (Figure 4B) liposomes indicated that significant alteration of the bilayer structure accompanied insertion of HvBot1 (Figure 4 and Supplemental Table 2). The position of the head group (z_H), hydrocarbon tail width (σ_C) and amplitude (ρ_C) were altered for both tested liposomal environments (Supplemental Table 2). As a result, the average distances between phosphate head groups across both bilayers (d_{HH}, taken to be the approximate bilayer thickness) decreased upon

insertion of HvBot1 in DMPC and asolectin liposomes consistent with membrane embedding (Supplemental Table 2).

HvBot1 protrudes 1.7 nm above the bilayer surface

Atomic Force Microscopy (AFM) revealed distinctive morphological and structural characteristics of HvBot1 that was co-translationally inserted in DMPC liposomes. Images were compared with those of bilayers of empty DMPC liposomes, and DMPC liposomes that underwent WG-CFPS in the absence of HvBot1 mRNA (Figures 5A and 5B). We only observed surface-protruding features in the DMPC liposomes containing HvBot1 (Figure 5C). In 66% of these high-resolution scans (≤1 μm x ≤1 μm; minimum pixel resolution 512 x 512) we found protruding features on an otherwise flat surface, which we presumed to be HvBot1 integrated into the bilayer (Figure 5C, white arrows). The average values (and standard deviations) of heights and diameters of these features were 1.7±0.6 nm (Figure 5D) and 19.2±7.5 nm, respectively. By contrast, only 10% of high-resolution scans on the DMPC samples undergoing WG-CFPS in the absence of HvBot1 mRNA presented any form of protrusions (Figure 5B), while no protrusions were observed in empty DMPC bilayers (Figure 5A).

HvBot1 is a channel-like anion transporter

To examine transport properties of HvBot1, we used: (i) asolectin liposomes with co-translationally inserted HvBot1 combined with stopped-flow light scattering spectrophotometry with fluorescent detection (Supplemental Figure 6); (ii) two-electrode voltage clamp (TEVC) electrophysiology of *X. laevis* oocytes expressing HvBot1 (Figure 6); and (iii) patch-clamp electrophysiology (Steller et al., 2012) of giant asolectin liposomes with co-translationally inserted HvBot1 (Figure 7).

Stopped-flow light scattering spectrophotometry recordings of borate transport by HvBot1 inserted in asolectin liposomes and using a pH-sensitive dye biscarboxyfluorescein (BCECF) showed an exponential fluorescence response curve, implying that borate anions were permeated by HvBot1. BCECF fluorescence increased due to the increasing pH values in the lumen of the proteo-liposomes, while no fluorescence increase was recorded in liposomes lacking HvBot1 (Supplemental Figure 6).

The ability of HvBot1 to mediate electrogenic movement of borate anions was demonstrated by electrophysiology experiments, where TEVC of *X. laevis* oocytes injected with *HvBot1* cRNA increased both inward and outward currents in the presence of external boric acid at three pH values, whereas no boric acid-inducible currents were detected in water-injected control oocytes (Figure 6). The largest current differences between the control oocytes and the Hv*Bot1*-gene-injected oocytes were recorded at pH 7.0, while very small currents were measured at pH 9.0. The reversal potential values for the *X. laevis* Hv*Bot1*-gene-injected oocytes were 49.9 mV, -12.5 mV and -58.6 mV, at pH 7.0, 8.0 and 9.0, respectively. Assuming a pH value of 7.69 in the cytosol of *X. laevis* oocytes (Sasaki et al., 1992) and complete equilibrium of boric acid across the plasma membrane, reversal potentials indicated that HvBot1 operated in a Nernstian manner with respect to borate anions and facilitated transport as a passive uniporter (Figure 6).

Patch-clamped giant liposomes with HvBot1 were used to further study transport properties (Figure 7). While no currents were observed when liposomes underwent WG-CFPS in the absence of HvBot1 mRNA, we observed single channel opening and closing events with liposomes containing HvBot1. These data indicated that HvBot1 operated as an ion channel between -60 and +100 mV (Figure 7A). The currents were completely abolished (Figure 7A) by applying 80 µM 4'-diisothiocyano-2,2'-stilbenedisulfonic acid (DIDS), a known blocker of anion channels (Liu et al., 1998). Currents measured with 5 mM NaCl and boric acid (internal face) and 5-50 mM boric acid concentrations (external side) at the same pH (Figure 7), moved reversal potentials towards more negative values (Figure 7B) and agreed with the calculated shifts in the Nernst potential for borate anions (0, -8.5, -18.4, -35.9 mV at 5, 12.5, 25 and 50 mM boric acid, respectively), which was consistent with the movement of borate anions through HvBot1. No currents were observed, when NaCl (internal face) was replaced with KCl or LiCl on the same bilayer. Borate anion transport *via* HvBot1 followed Michaelis-Menten ($v_0=V_{max}[S]/(K_m+[S])$ kinetics with K_m=104.1 ± 5.4 µM and G_{max} = 15.8±0.18 pS (Figure 7C). The K_m constant indicated that in our system, HvBot1 has a tighter affinity for borate anions than Bor1p from *S. cerevisiae* (K_m of 1.8 mM) (Jennings et al., 2007). Conductance dependencies on symmetric (25 mM) concentrations of chloride, phosphate, nitrate and sulphate anions indicated that HvBot1 permeated a variety of polyvalent anions (Figure 7D). Lower concentrations of these anions (0.5 to 10 mM) did not generate detectable currents. To examine if HvBot1 operated as a Na^+-dependent channel or a Na^+ co-transporter, we measured currents with varying concentrations (5-25 mM) of sodium glutamate on the external side, and a constant symmetric concentration (25 mM) of boric

acid. These data showed that there were either no changes (for NaCl) or small changes (for sodium glutamate, Figure 7E) in reversal potentials, suggesting that Na^+ was activating currents rather than being transported by HvBot1.

DISCUSSION

Coverage of the 3D conformational space of α-helical proteins remains sparse. This necessitates structural predictions to help with understanding of membrane proteins constituting around 30% of a typical proteome (Shadiac et al., 2013). Here, we (i) present an *in silico* model of HvBot1 that is important for molecular descriptions of permeation mechanisms by plant anion-permeable efflux transporters of the AE 2.A.31 family, and (ii) reveal transport properties of HvBot1, using cell-free synthesis coupled with nanotechnology. Deployment of a cell-free synthesis for HvBot1 in significant quantities overcome problems associated with production of functional proteins.

MD simulations of HvBot1 in a lipid environment revealed the presence of a Na^+-binding site trapped among oxygen atoms, which create a large activation barrier for Na^+ to escape from this particular conformational state of HvBot1 (Figure 1 and Supplemental Figure 2). Additional MD simulations using alternative conformation of HvBot1 indicated the presence of the 2^{nd} Na^+-binding site, located around the 5^{th} and 6^{th} membrane α-helices, and suggesting that borate anions may approach the pore-forming region from several directions. We propose Na^+ cations may attract borate during certain stages of the transport event creating a possibility for borate to be captured inside the HvBot1 pore since the pore region is located near the Na^+-binding sites (Supplemental Figure 2A), or that Na^+ locally neutralize the negatively charged milieu of phospholipids to allow for passage of borate anions through a pore (Figure 2). Comparative analyses of residue conservation (Celniker et al., 2013), based on 500 sequences with 35% or greater sequence identity to HvBot1, including that of AtBor1 from *A. thaliana* (GenBank accession BAC20173.1), revealed that the pore-forming α-helices and three (T68, E70 and T71) out of six Na^+-binding residues achieved high conservation scores (Supplemental Figures 2C to 2E and Supplemental Figure 7). This led us to conclude that these structural elements might be critical for anion movement. As our *in silico* observations suggested Na^+-dependency during transport of anions through HvBot1, by using patch-clamped proteo-liposomes, we were able to experimentally observe Na^+ dependency of the transporter. In particular, the liposome system allowed us to uncover kinetic properties without compromise of the presence of other proteins in a bilayer. We could also simulate

HvBot1 quaternary structure (Figure 1E, Supplemental Figure 5 and Supplemental Table 1), where each monomer is likely to contribute with its own part to the total energy of each supra-assembly.

As it may be expected that the HvBot1 transport protein is inserted in liposomes in either orientation, we looked for two distinct populations of protruding features through AFM. However, only a single topology feature was observed (Supplemental Figure 8). The size (1.7 nm) of the protrusions in bilayers was consistent with the modelled size of the sombrero component, which was predicted to extend from the membrane by approximately the same distance (Figure 1 and Supplemental Figure 2). These observations suggested that HvBot1 was incorporated in DMPC liposomes predominantly in one orientation. Further, the SAXS data indicated that HvBot1 spanned liposomal bilayers and that in response to co-translational insertion the thickness of bilayers was locally reduced. Similar findings were reported for nanodisc-reconstituted bacteriorhodopsin (Kynde et al., 2014).

In summary, computational, bioinformatics, biochemical, biophysical and electrophysiology data provided compelling support for HvBot1 to be annotated as a Na^+-dependent channel-like anion-permeable transporter with high affinity to borate anions. Our conceptual approach can be utilized for studies of similar transporters that are engineered *via* rational design or of natural variants (Pallotta et al., 2014). While this knowledge is central to understanding mechanisms of plant boron-toxicity tolerance, our methodology is applicable to other transporter structure/function studies in a high-throughput mode. We conclude that a combined *in silico* approach of structural predictions of architecture, and *in vitro* experimental observations can significantly enhance the knowledge of fundamental biology of membrane transporters. Our data reveal essential knowledge for plant biologists and breeders involved in production of future elite cultivars adapted to areas, where high boron limits plant productivity.

METHODS

In silico construction of 3D model of HvBot1 and generation of oligomeric assemblies

Predictions of the HvBot1 secondary structures were performed using PSIPRED (Jones, 1999), MEMSAT3 (Jones et al., 1994), MEMSAT SVM (Nugent and Jones, 2009), MEMPACK (Nugent et al., 2011), SABLE (Wagner et al., 2005) and I-TASSER (Zhang, 2008), and were combined. The initial 3D model of a full length HvBot1 protein with

truncated loops was obtained from I-TASSER (Iterative Threading Assembly Refinement) (Zhang, 2008). The membrane part of the model obtained from I-TASSER resembled that of the crystal structure of the uracil transporter (PDB accession 3QE7). The structure of membrane α-helices was manually adjusted using the Accelrys Discovery Studio Environment v3.5 (Accelrys Software Inc., San Diego, CA, USA) to receive agreement with predicted secondary structures. To re-construct the whole protein in a membrane, we employed a Divide and Conquer method (Cormen et al., 2000). Namely, we divided the protein anchored in a dioleoylphosphocholine (DOPC) lipid bilayer into region I (membrane α-helices) and region II (inter-connecting loops), followed by recombination of both regions. We carried out molecular dynamics (MD) simulations of the whole system with explicit water, salt, and lipid molecules following minimisations and heating cycles as follows. The end-to-end distances of the loops were chosen to fit the corresponding protein gaps, as the dispositions of loops were not known, where the geometries of region I were selected from those at the end of 5 ns MD simulations. To obtain the desired end-to-end distances of the protein structure, two different approaches were employed for short and long loops. For the short loops, the linear peptide chains were built using the AMBER sequence command, which created the topology and coordinate files for AMBER simulations (Caseet et al., 212), followed by minimisation, heating/equilibration and MD calculations proceeding typically for 1-2 ns at 300 K. Out of these MD trajectories, conformations at the desired distances were selected using gOpenMol visualizer and analyzer (Laaksonen, 1992; Bergman et al., 1997). For long loops, the short MD simulation did not lead to desired conformations. Therefore, each end-to-end distance of a selected conformation was manually adjusted to achieve the desired conformation followed by minimisation using Accelrys Discovery Studio Environment v3.5. Since optimisation resulted in a deviation from a desired distance, this procedure was repeated until the target distance was reached. During the Divide and Conquer method we employed a re-association procedure, originally used to construct large molecules for Quantum Mechanics simulations (Lee and Friesner, 1993; Lee et al., 2008). To re-associate region II with region I, the terminal residues of both regions, and several buffer residues were included to overlap the terminal residues, such that the atoms of the peptide bonds at the cut-out regions overlapped with high accuracy. Using the Accelrys Discovery Studio Environment v3.5, the overlaid atoms and the buffer residues were deleted to re-construct the whole system without overlapping atoms. Once the recombination process was completed, partial minimisation of the whole system, except of α-helical and lipid regions, was carried out using the Accelrys Discovery Studio Environment v3.5 to avoid clashes of

atoms or atypical bond distances. Once the protein was modelled, consisting of 574 residues, where the first 24 N-terminal residues and the last 68 C-terminal residues were not included (as no structural counterparts were found in databases), lipids, explicit water and salt molecules were added to produce a system with 102,070 atoms that was minimized by AMBER. The force field algorithms during modelling were ff99SB (Hornak et al., 2006) for protein, lipid11 (Skjevik et al., 2012) for lipid molecules and TIP3 (Jorgensen et al., 1983) for water molecules. After gradually heating the system to 300 K, equilibration MD in duration of 30 ns and production runs were (84 ns) were carried out, using the SHAKE algorithm with a time step of 2 fs and Langevin dynamics with the collision frequency of 1.0, a random seed, and the surface tension of 10.0 dyne/cm.

The stereochemical quality of the HvBot1 structure was performed using PROCHECK (Laskowski et al., 1993). The evaluation indicated that 99.6% of residues were located in the most favoured, additionally allowed and generously allowed regions, when excluding Gly and Pro residues. Two residues S392 and L120 (0.4%) were located in a disallowed region. The respective overall G-factors, determined by PROCHECK, which estimate overall stereochemical parameters were -0.31, and 0.17 for HvBot1 and the uracil transporter (3QE7) that was used as a starting structure during initial stages of modelling. The *z*-score values deduced from ProSa2003 (Sippl, 1993), reflecting combined statistical potential energy, were -5.39 and -8.92 for HvBot1 and 3QE7, respectively.

Electrostatic surface potential was calculated with the Adaptive Poisson–Boltzmann Solver (Baker et al., 2001) with solvent contributions (dielectric constants for solvent and protein components were 78 and 2, respectively) as implemented in PyMOL (http://www.pymol.org), and mapped onto the molecular surfaces generated with a probe radius of 1.4 Å. The molecular graphics was generated with PyMOL.

To obtain rational estimates of spatial dispositions of individual protomers within quaternary structure of HvBot1, we built dimer (D) conformations under the following assumptions: (i) lipid, ion and water molecules were removed from a MD simulated protein-lipid complex (Figure 1C); (ii) the sombrero component (Figure 1A, five short intracellular α-helices and adjoining loops; residues 359-462) with itself or with other regions (residues 264-270 and/or 188-194) located on the exposed intracellular loops of a second protomer were considered to participate in oligomer formation; (iii) N- and C-terminal regions of HvBot1 were not considered to be involved in oligomer formation. During the second step we generated an initial conformation of dimer D1 (Supplemental Figure 5A, top panel). The second D2 conformation (Supplemental Figure 5A, middle panel) was generated by a 45^{o}-

counter-clockwise rotation of the second protomer D1 around the z-axis. The third D3 conformation (Supplemental Figure 5A, bottom panel) was initially obtained by a 120^{o}-clockwise rotation of the second protomer D1 around the z-axis. In the third step, both protomers for each D1 to D3 conformations were manually adjusted, so that the two protomers could form favourable electrostatic and/or van der Waals interactions. Furthermore, these manually adjusted dimers were optimized by AMBER with implicit solvent using the same force field parameters as those that were used through the MD simulations specified above. During geometry optimisations, no symmetry restrictions were used. Based on optimized D1-D3 conformations (Supplemental Figure 5A), three trimeric T1-T3 conformations (Supplemental Figure 5B) were generated, such that all potential combinations of two protomers in trimers could belong to dimers. In the final step, trimeric conformations T1-T3 were optimized. The total energies for optimal D1-D3 and T1-T3 geometries are summarized in Supplemental Table 1. It should be noted, that these conformations are based on (i) - (iii) criteria specified above and that other conformations are theoretically possible.

Chemicals and reagents

The sources of oligonucleotide primers, restriction and DNA modifying enzymes, plasmid extraction kits, EDTA-free Complete Protease Inhibitor Cocktail tablets and other chemicals were described previously (17). Benzonase (40 U/ml) was from Invitrogen (Carlsbad, CA, USA), asolectin lipid from soybean and all other lipids were from Sigma-Aldrich (St. Louis, MO, USA) and Avanti Polar Lipids (Alabaster, AL, USA), respectively. Styrene/Maleic Anhydride copolymer 3:1 (SMA) was provided by Professor Michael Overduin and Dr Timothy Knowles (The University of Birmingham, Birmingham, UK).

Wheat-Germ Cell-Free Protein Synthesis (WG-CFPS) of HvBot1

To construct the HvBot1 DNA fusion, a full-length HvBot1 (GenBank accession ABS83562.1) was amplified from cDNA of the barley (*Hordeum vulgare* L.) landrace Sahara 3771 (Sutton et al., 2007) and cloned in-frame into the pEU-EO1-MCS^{TM} expression vector (CellFree Sciences, Tsurumi-ku, Yokohama, Japan), which included an N-terminal 6xHis tag followed by the Tobacco-Etch Virus (TEV) site (Glu-Asn-Leu-Tyr-Phe-Gln↓Gly) (Phan et al., 2002), to generate the 6xHis-TEV-HvBot1-pEU DNA fusion (Supplemental Table 3).

To prepare unilamellar asolectin liposomes for co-translational insertion of HvBot1 *via* WG-CFPS, the lipid was dissolved in chloroform at 10 mM concentration, deposited on the conductive side of indium tin oxide glass slide and allowed to dry for 2-4 h at an ambient temperature. The slide was purged with a nitrogen gas continuously for 15-30 minutes to remove residual traces of chloroform. An O-ring was placed around the dried lipid film, into which 200 µl of 100 mM sorbitol was added. Electro-formation of giant unilamellar vesicles (GUVs) proceeded at 37^{o}C using the Vesicle Prep Pro (Nanion Technologies, Munich, Germany) as described by Nanion. Preparation of 100 nm and 400 nm liposomes proceeded in the lipid re-hydration buffer (100 mM NaCl, 25 mM Hepes, pH 7.5), into which dried lipids were resuspended to a final concentration of 50 mg/ml. Liposomes were extruded 21 times above the lipid transition temperatures using the Liposofast extruder (Avestin, Ontario, Canada) equipped with 100 nm or 400 nm pore size polycarbonate filters.

To conduct WG-CFPS of HvBot1 in the presence of unilamellar liposomes and surfactants, the synthesis was conducted as described previously (Periasamy et al., 2013), through uncoupled transcription and translation at 25^{o}C for 24 hours in a bilayer mode. Briefly, a transcription reaction was set up at 42^{o}C and transcribed mRNA was added to the translation reaction mixture to synthesize HvBot1 *via* co-translational insertion into liposomes, prepared as described above. DMPC (1,2-dimyristoyl-sn-glycero-3-phosphocholine), POPC (1-palmitoyl-2-oleoyl-*sn*-glycero-3-phosphocholine) and asolectin lipids were prepared at 50 mg/ml. A mixture of POPC:POPE (1-palmitoyl-2-oleoyl-*sn*-glycero-3-phosphoethanolamine): POPG [1-palmitoyl-2-oleoyl-sn-glycero-3-phospho-(1'-rac-glycerol)]:cholesterol=6:3:1:0.1 (by weight) was used at 10 mg/ml. For synthesis of HvBot1 with surfactants, liposomes were replaced by Brij-58, n-dodecyl-β-D-maltoside, n-decyl-β-D-maltoside, digitonin, Triton X-100, Tween 80 or acetylated (Ac) surfactant peptides Ac-AAAAAAD (Ac-Ala-Ala-Ala-Ala-Ala-Ala-Asp), Ac-IIID (Ac-Ile-Ile-Ile-Asp) and Ac-LLLK-NH_2 (Ac-Leu-Leu-Leu-Lys-NH_2) in the translation reaction as described (Periasamy et al., 2013). Samples from WG-CFPS were evaluated by immuno-dot-blot analyses and the positive samples were analyzed by SDS-PAGE coupled with Western immuno-blot (WIB) analyses using either a mouse IgG2a isotype anti 6xHis monoclonal antibody (Clontech, Takara Bio, Shiga, Japan) or a crude serum raised through immunisation of rabbits with the CSVDKDLKSLKDAVLREGDE peptide, derived from HvBot1. Prior to loading on SDS-PAGE gels, the protein samples were incubated for 30 min at 37^{o}C in a SDS-PAGE loading buffer. Immuno-blots were developed with the Novex® ECL HRP Chemi-Luminescent substrate Reagent Kit (Invitrogen) or with the BCIP/NBT-purple liquid reagent

(Sigma-Aldrich) according to the manufacturer's instructions and the images were scanned (Clinx Science Instruments, Shanghai, China). Blue native PAGE proceeded according to the NativePAGE™ Bis-Tris Gel protocol (Invitrogen).

HvBot1 liposomes were purified as follows. Liposomes with co-translationaly incorporated HvBot1 were purified using Accudenz density gradient ultra-centrifugation as described (Periasamy et al., 2013), except that the solutions did not contain NaCl. Purified HvBot1 liposomes were dialyzed for 14-18 h at 4^{o}C using 10 kDa cut-off Slide-A-Lyser Mini dialysis cups (Thermo Scientific, Rockford, IL, USA) against 10 mM histidine buffer, adjusted with Bis-Tris Propane (BTP) to pH 7.5, and stored on crushed ice, where they remained stable for up to five days.

The diameters of proteo-liposomes were determined with the NICOMP 380 Particle Sizing Systems (Santa Barbara, CA, USA) operating in a vesicle mode. The data were weighted on approximately 60 liposomes.

Topology of HvBot1 in DMPC liposomes was determined by digestion with TEV protease (Phan et al., 2002) as follows. Incubation of proteo-liposomes with TEV protease proceeded for 16 h at 25^{o}C with or without TEV (Periasamy et al., 2013). Aliquots of non-digested and TEV protease-treated liposomes were detected by WIB analyses using a mouse IgG2a isotype anti 6xHis monoclonal antibody (Clontech) and a crude serum raised against the HvBot1 peptide specified above. The immuno-blots were developed with the Novex® ECL HRP Chemi-Luminescent substrate Reagent Kit (Invitrogen) as described above and scanned.

Tryptic mapping of HvBot1 by Electrospray Ionisation (ESI) Mass Spectrometry (MS)

The HvBot1 protein co-translationally synthesized in the presence of the 400 nm asolectin liposomes was subjected to SDS-PAGE and the band coinciding with the position of HvBot1 was cut out from the gel. Tryptic mapping proceeded as described (Periasamy et al., 2013). The ESI MS analysis revealed ions matching peptide sequences of HvBot1 (GenBank accession ABS83562.1): DDWLAGLR, GIVGEFSMPK, MHEVFIEMDNK, EGDEDGKLAGEFDPR, IQLLFVGASR, VLEGPHASFVESVSSR, FFEPNDLR and IDAEILDELTTHRG.

Expression and purification of HvBot1 from *Pichia pastoris*

To construct the HvBot1 DNA fusion for expression, amplified HvBot1 cDNA was digested with *Xho*1 and *Not*1 (NEB), and cloned in-frame into the pPICZ-B expression vector (Invitrogen) to generate the 6xHis-HvBot1-pPICZ-B DNA fusion (Supplemental Table 3). This DNA fusion was linearized and transformed into competent *P. pastoris* X-33 cells according to the EasySelect™ Pichia Expression Kit Manual (Invitrogen). Approximately 100 colonies were picked after three days of growth on agar plates and used to inoculate two ml of liquid BMGY media (media composition is specified in the EasySelect™ Pichia Expression Kit Manual, Invitrogen) in 10 ml conical test tubes. Liquid cultures were grown for two days at 25^{o}C, transferred to liquid BMMY media and induced for four days at 25^{o}C maintaining 1% (v/v) methanol (Nordén et al., 2011). After four days, cells were harvested by centrifugation (10 min, 4500xg, ambient temperature), pellets were resuspended in 10% (v/v) glycerol and 150 µl of cells were lysed in the lysis buffer that contained the 90% (v/v) Yeast-Buster reagent (Invitrogen), 1% (v/v) benzonase, 2 mM mercaptoethanol, 10 mM EDTA, 1 mM PMSF, and an EDTA-free Complete Protease Inhibitor Cocktail (Roche, Indianapolis, IN, USA). Distribution of HvBot1 in various fractions was evaluated as follows. The mixture was incubated for 20 min at room temperature on a microtiter shaker (Ratek, Victoria, Australia) at 300 rpm and the lysate was collected by centrifugation (10 min, 4500xg, ambient temperature) to generate the first soluble fraction. The pellet was resuspended in 4% (w/v) SDS, incubated for 10 min at ambient temperature and the second solubilized fraction was collected by centrifugation (10 min, 4500xg, ambient temperature). The remaining pellet was solubilized in 8 M urea in 0.1 M NaOH and the third solubilized fraction was collected by centrifugation (10 min, 4500xg, ambient temperature). The fourth fraction represented the material that remained insoluble after the alkali/urea treatment. The presence of HvBot1 in all fractions was evaluated by immuno-dot-blot and SDS-PAGE coupled with WIB analyses as described above. The majority of HvBot1 was allocated to an alkali/urea fraction.

To analyse protein expression levels of selected clones, medium scale expression trials were performed using 250 ml cultures induced for three days by 0.5% (v/v) methanol. The cells were pelleted by centrifugation (5 min, 4500xg, 4°C), resuspended in a breaking buffer (5% v/v glycerol, 50 mM Tris-HCl, pH 8), disrupted 10 times in the presence of acid-washed glass beads (Sigma-Aldrich) in a Bead-Beater (Bio Spec Products, Bartlesville, OK, USA) with 30 sec intermittent cooling intervals and the homogenates were clarified by centrifugation (5 min, 4500xg, 4°C). To collect a mixed-membrane fraction, the supernatant

was centrifuged (120 min, 200,000xg, 4°C), and the membrane pellet at a protein concentration 20-40 mg/ml was re-suspended in the solubilisation buffer containing 10% (v/v) glycerol, 200 mM NaCl, 50 mM Tris-HCl, pH 8 and 2.5% (w/v) SMA. Solubilisation proceeded for three hours at room temperature and the resultant mixture was centrifuged (60 min, 150,000xg, 4°C) to remove any insoluble aggregates. SMA-solubilized HvBot1 was mixed with 0.5 ml of the Complete His-Tag Purification Resin (Roche) pre-equilibrated in 10% (v/v) glycerol, 200 mM NaCl and 50 mM Tris-HCl, pH 8, and incubated for 2 h at 4^{o}C. The resin with solubilized HvBot1 was washed with the equilibration buffer, and HvBot1 was released in the elution buffer containing 10% (v/v) glycerol, 200 mM NaCl, 300 mM imidazole and 50 mM Tris-HCl, pH 8 in four steps.

Confocal imaging of HvBot1 in *P. pastoris*

To construct the HvBot1-Green Fluorescent Protein (GFP) DNA fusion for expression in *P. pastoris*, amplified HvBot1 cDNA was sub-cloned in-frame into the pPICZ-B expression vector (Invitrogen) through hybridisation with *GFP* cDNA using an GenArt kit (Invitrogen) to generate the HvBot1-TEV-GFP-10xHis-pPICZ-B DNA fusion (Supplemental Table 3). To confirm expression and cellular localisation of HvBot1, imaging of GFP-tagged HvBot1 expressed in *P. pastoris* was performed using the LSM 5 PASCAL fluorescence microscope (Carl-Zeiss, Jena, Germany). Cells with an empty pPICZ-B plasmid transformed in *P. pastoris* were used as a negative control.

Transient expression of HvBot1 in onion epidermal cells

To construct the HvBot1 DNA fusion for transient expression, the HvBot1 cDNA was introduced into the Gateway vector pMDC83 (Invitrogen) by recombination to generate the 35S-HvBot1-GFP DNA fusion (Supplemental Table 3). The fusion was used to transform onion (*Allium cepa* L.) epidermal cells by particle bombardment, using a biolistic PDS-1000/He particle delivery system (BioRad). Onion cells were maintained in the dark on Murashige and Skoog medium for 24 h, prior to confocal image analysis. GFP fluorescence was visualized using a 488 nm argon laser, before and after plasmolysis by treatment with 1 M sucrose for 1 min.

Analysis of insertion of HvBot1 in bilayers of proteo-liposomes by SAXS using synchrotron radiation

The SAXS data of the asolectin or DMPC liposomes with and without HvBot1 were collected on the SAXS/WAXS beamline of the Australian Synchrotron (Melbourne, Australia) (Kirby et al., 2013) using a Pilatus-1M pixel-array detector (Dectris, Switzerland). For each data set 60 frames of a 1-second exposure time were collected from a sample flowing vertically through the X-ray beam at a constant 5 μl/s flow rate in a temperature-controlled 1.5 mm quartz capillary. Solutions of HvBot1 inserted in asolectin or DMPC liposomes (extruded through 50 nm or 100 nm filters) were measured at 23°C in 50 mM Tris-HCl buffer, pH 7.5 containing 300 mM NaCl at approximately 0.2 to 0.6 mg/ml protein and 5 mg/ml lipid concentrations. The sample-to-detector distance was 1.5 m covering a range of momentum transfer $0.01<q<0.6$ Å^{-1} ($q=4\pi\sin\theta/\lambda$, where 2θ is a scattering angle and $\lambda=1.03$ Å is the X-ray wavelength). Comparison of successive 1-second frames revealed no detectable radiation damage. Data from the detector were normalized to the transmitted beam intensity, scaled to absolute intensity using water as an intensity standard, averaged and scattering of the buffer solutions was subtracted using the ScatterBrain IDL software package available at the Australian Synchrotron. The SAXS profiles were analyzed using the latest ATSAS package (Petoukhov et al., 2012) and the bilayer electron density profiles that were extracted from SAXS data using a global analysis approach of GAP (Pabst et al., 2000) with asolectin (ULV model) and DMPC (MCT model) liposomal data fits, assuming positionally uncorrelated bilayers and the inclusion of a structure factor, respectively.

AFM evaluation of morphological properties of HvBot1 co-translationally synthesized in DMPC liposomes

All AFM imaging was conducted by using the JPK Instruments NanoWizard III AFM (JPK Instruments, Berlin, Germany) equipped with a temperature controlled BioCell™ stage maintained at 19.5±0.2°C, in 25 mM Hepes buffer pH 7.5, containing 100 mM NaCl. Imaging was performed in contact mode using optimized parameters and MSNL cantilevers (Bruker AFM Probes, Camarillo, CA, USA), whereby the spring constants k, determined by the thermal calibration method were around 0.17 N/m. This method involves recording the thermal noise spectrum in air before performing a force-distance curve on a hard surface,

such as mica to obtain the cantilever sensitivity. These two values are then used to estimate the spring constant. The force imparted by the tip on the sample during scanning was between 120 and 300 pN. The susceptibility of this technique to cantilever drift resulted in continual adjustment of the vertical deflection voltage between scans to maintain an appropriate imaging force. Scan rate was maintained between 8-12 Hz resulting in a tip velocity between approximately 5-9 µm/sec for small scale images. All components of the BioCell™ stage and cantilever mounting apparatus (glass block/spring) were sonicated in ethanol and rinsed in milliQ water prior to use to reduce particles in solution, which could interfere with imaging. The DMPC liposomal fusion with HvBot1 proceeded as follows. Mica discs of 9.9 mm in a diameter were freshly cleaved and glued to clean glass coverslips of 24 mm in a diameter, using a UV curable adhesive (Loctite® 358) before being incubated at 27°C until required. Care was taken to ensure an even distribution of glue between mica and coverslip, and that the glue was fully cured with no air bubbles. Aliquots of proteo-liposome stock solution were diluted to 0.5 mg/ml with 25 mM Hepes buffer, pH 7.5 in a 1.5 ml centrifuge tube and gently mixed. Before extrusion both the liposomal solutions and the extruder apparatus were heated to 27°C. A 500 µl volume of the liposomal solutions was extruded through a Nucleopore™ polycarbonate membrane with 100 nm pore size, and 20 µl was spotted on to the freshly cleaved mica and incubated for 5 min at ambient temperature. Prior to imaging, mica was washed in a constant stream of buffer to avoid de-wetting and positioned in the BioCell™ stage. The stage was mounted on the AFM apparatus and equilibrated for approximately 15 min before imaging.

HvBot1 insertion in DPMC liposomes was confirmed by WIB analysis. As, HvBot1 could be distributed in bilayers in two distinct populations, height values of protruding features were recorded by taking cross-sectional parameters through the highest point on the feature, which were indicative of the distance from the membrane surface. The heights recorded to construct the histogram would therefore reflect real topology of HvBot1 in liposomes, and describe how the HvBot1 protein protruded from the surface of the bilayer imaged by AFM.

Recordings of transport in liposomes with inserted HvBot1 using stopped-flow light scattering

A pH-sensitive biscarboxyfluorescein (BCECF) (Invitrogen) dye was added at 80 µM to 400 nm asolectin HvBot1 liposomes, prepared as described above; the HvBot1 protein amount

corresponded to 25 µg as quantified by SDS-PAGE and ImageJ (Schneider et al., 2012). The mixture was incubated for 15 min at ambient temperature of approximately 21^{o}C. The mixture of HvBot1 liposomes and BCECF was subsequently probe-sonicated (Branson, Danbury, CT, USA) for 10 sec followed by 1 min incubation on ice. This procedure was repeated twice to ensure that the dye penetrated HvBot1 liposomes. Unincorporated BCECF was removed by centrifugation (5 min, 4500xg, ambient temperature) in 10 mM MOPS-KOH buffer, pH 6.8 until the fluorescence of the supernatant fraction decreased to zero. Transport measurements with boric acid were carried out using a DX.17MV stopped-flow spectrophotometer (Applied Photophysics, Surrey, UK), whereby fluorescence was measured at excitation and emission wavelength of 488 nm and 512 nm, respectively, upon rapidly mixing liposomes with a solution that created an inwardly-directed concentration gradient of boric acid in 10 mM MOPS-KOH buffer, pH 8.5, containing 300 mM sucrose and 100 mM boric acid; the pH after mixing was 8.5. Reversal potential values were determined using a Goal Seek feature in Microsoft Excel 2010, by setting y-intercept values of the fitted functions to zero.

TEVC electrophysiology recordings of transport by HvBot1 expressed in *Xenopus laevis* oocytes

To construct the HvBot1 DNA fusion for TEVC electrophysiology recordings, amplified HvBot1 cDNA was cloned into the GATEWAY entry vector pCR8 (Invitrogen) and recombined into pGEMHE:DEST *via* Gateway LR clonase II (Invitrogen) to generate the pGEMHE:DEST-HvBot1 DNA fusion (Supplemental Table 3). This fusion was linearized with *NheI* and used as a template for capped RNA (cRNA) transcription, using a mMessage mMachine T7 kit (Life Technologies, Victoria, Australia). Oocytes from *X. laevis* were isolated and maintained as described (Virkki et al., 2006). Oocytes were injected with 46 nl of cRNA (0.7 µg/µl) encoding HvBot1 or with RNase-free water using a Nanoject II automatic nanolitre injector (Drummond Scientific, Broomall, PA, USA). After injection, the oocytes were incubated at 18°C for 2 days in ND96 solution (96 mM NaCl, 2 mM KCl, 5 mM $MgCl_2$, 0.5 mM $CaCl_2$, 5 mM Hepes-KOH, pH 7.6) containing 2.5 ml of horse serum, 50 µg ml tetracycline, 5000 units of penicillin and 5 mg of streptomycin per 50 ml, with the solution changed daily. Experiments were undertaken two days after injections of oocytes. TEVC was performed on whole oocytes using an OC-725C amplifier (Warner Instruments Corporation, Hamden, CT, USA) with signals digitized with an Axon 1440A Digidata system

(Axon, Raleigh, NC, USA). Currents were recorded using pClamp 10.3 software (Axon). Membrane currents were recorded in a control bath solution containing 25 mM N-cyclohexyl-2-aminoethanesulfonic acid (CHES) and 0.3 mM $CaCl_2$, or in a bath solution containing 25 mM boric acid and 0.3 mM $CaCl_2$. All solutions were adjusted to pH 7, pH 8 or pH 9 using 0.5 M BTP. Solution osmolarities were adjusted to 220 mOsmol/kg with mannitol. Readings were recorded by clamping the membrane potential at a holding voltage of -40 mV, while the stepwise increments of 20 mV were carried out from -120 mV to 40 mV for 1.5 sec, returning to -40 mV between each sweep.

Electrophysiology recordings of transport using asolectin patched-clamped giant liposomes with inserted HvBot1

Between 3-6 µl of a suspension of giant proteo-liposomes, prepared as described above, containing approximately 5 µg of HvBot1, determined by SDS-PAGE and ImageJ (Schneider et al., 2012), were pipetted onto a micro-structured glass chip with an aperture of approximately 1 µm in diameter. Measurements were performed at ambient temperature with the Port-a-Patch automated patch-clamp system (Nanion Technologies) using borosilicate glass chips. Single-channel events were recorded by adding a solution containing 10 mM histidine, 5 mM NaCl and 5 mM boric acid, pH 7.5 on the internal side of a glass chip, and 5-75 mM boric acid concentrations on the external side of the chip. Boric acid was dissolved in the same buffer as that used on the internal side of the chip. The osmolarity of all buffers was adjusted to 220 Osmol/kg using 1M sorbitol, dissolved in milliQ water (conductance of 17.2 µS/cm). During transport studies, the inhibitor 4,4'-diisothiocyano-2,2'-stilbenedisulfonic acid (DIDS) was used at 80 µM concentration in the presence of 25 mM boric acid. Kinetic parameters K_m and G_{max} were derived from dependence of conductance on 0.085-1.275 mM concentrations of borate. For all other anions (phosphate, chlorate and nitrate and sulphate), symmetric concentrations at 25 mM were used. Dependence of conductance of HvBot1 on Na^+ was measured with symmetric 25 mM boric acid and 2.5-25 mM concentrations of NaCl or sodium glutamate on the external side. All solutions were pH-adjusted with BTP unless otherwise indicated. The measurements were recorded using a HEKA amplifier (HEKA Electronics, Chester, Canada) connected to Ag/AgCl electrodes in the Port-a-Patch system. The signal was filtered using a 4-pole low-pass Bessel filter at a frequency of 10 kHz and sampled at 50 kHz, and the signal was acquired using an EPC10 amplifier (HEKA

Electronics). The data were analyzed using HEKA software (HEKA Electronics). All measurements were repeated three times, from which the values of SEM were calculated.

Accession Numbers

GenBank accessions are: ABS83562.1 for Hv*Bot1* and KF148625 for Ta*Bot-B5b*. PDB accession for the uracil transporter is 3QE7. UniProt accessions (Supplemental Figure 7) are: A9XTK3 (*Hordeum vulgare*), I1NKR0 (*Oryza glaberrima*), B9RB14 (*Ricinus communis*), H2KX48 (*Oryza sativa*), M5XLJ9 (*Prunus persica*), Q8VYR7 (*Arabidopsis thaliana*), A5JUZ5 (*Citrus macrophylla*), K4AVY8 (*Solanum lycopersicum*) and G7IKZ7 (*Medicago truncatula*).

Supplemental Data

The following materials are available in the online version of this article.

Supplemental Figure 1. A Time *versus* distance (in Å) profile of nine oxygen atoms that coordinate Na^+ during 84 ns MD simulation of HvBot1.

Supplemental Figure 2. Properties and conservation of HvBot1.

Supplemental Figure 3. WG-CFPS of HvBot1 in the presence of liposomes and surfactants.

Supplemental Figure 4. Subcellular localisation of chimeric HvBot1-GFP in *P. pastoris* and after transient expression in onion cells, evaluated by confocal imaging.

Supplemental Figure 5. Predicted spatial dispositions of protomers in quaternary assemblies of HvBot1.

Supplemental Figure 6. Transport of borate anions by HvBot1 proteo-liposomes analyzed by stopped-flow light scattering.

Supplemental Figure 7. Multiple sequence alignment of HvBot1 with nine closely related putative plant transport proteins belonging to the AE 2.A.31 family.

Supplemental Figure 8. Schematic representation of a bilayer observable by AFM.

Supplemental Table 1. Total energies of simulated dimeric D1-D3 and trimeric T1-T3 supra-molecular assemblies of HvBot1.

Supplemental Table 2. Bilayer phospholipid head-group distances determined from a global fit of the SAXS data using ULV and MCT (asolectin) and MCT (DMPC) models.

Supplemental Table 3. Primers used for cloning of HvBot1.

ACKNOWLEDGMENTS

We thank Michael Overduin and Timothy Knowles (The University of Birmingham, UK) for SMA, Gwenda Mayo and Jingwen Tiong (University of Adelaide) for advice on imaging, Leanne Kelly and Tony Bacic (University of Melbourne, Australia) for mass spectrometry analysis, and Peter Kolesik (Bionomics Ltd., Australia) for discussions. This research was supported by grants from the Australian Research Council (to M.H., N.V., M.G. and S.D.T.), the Grains Research & Development Corporation (to M.H. and J.R), the Waite Research Institute (to M.H. and M.G.), the South Australian Government (to M.G. and S.D.T.) and the API scholarships from the University of Adelaide (to Y.N. and J.R.). A part of research was funded by the SAXS/WAXS beamline of the Australian Synchrotron (to M.H., H.D.T.M. and N.K).

AUTHOR CONTRIBUTIONS

M.H. designed research. Y.N., J.R., N.S., J.H., T.S., G.M., H.D.T.M., J.-G.L., S.D.T. and M.H. performed research. Y.N., H.D.T.M., N.K., M.G., S.D.T., N.H.V., J.-G.L., Y.G.Y. and M.H. analyzed data. M.H wrote the article with input from all authors.

REFERENCES

Baker, N.A., Sept, D., Joseph, S., Holst, M.J., and McCammon, J.A. (2001). Electrostatics of nanosystems: application to microtubules and the ribosome. Proc. Natl. Acad. Sci. USA **98**: 10037-10041.

Bergman, L., Laaksonen, L., and Laaksonen, A. (1997). Visualization of solvation structures in liquid mixtures. J. Mol. Graph. Model. **15**: 301-306.

Berka, K., et al. (2012). MOLEonline 2.0: interactive web-based analysis of biomacromolecular channels. Nucleic Acids Res. **40**: W222-W227.

Boron, W.F., Chen, L., and Parker, M.D. (2009). Modular structure of sodium-coupled bicarbonate transporters. J. Exp. Biol. **212**: 1697-1706.

Caseet, D.A., et al. (2012). AMBER 12. University of California, San Francisco, USA.

Celniker, G., et al. (2013). ConSurf: Using evolutionary data to raise testable hypotheses about protein function. Isr. J. Chem. **53**: 199-206.

Cormen, T.H., Leiserson, C.E., and Rivest, R.L. (2000). Introduction to algorithms (1st ed.). MIT Press and McGraw-Hill.

Hayes, J.E., and Reid RJ (2004). Boron tolerance in barley is mediated by efflux of boron from the roots. Plant Physiol. **136**: 3376-3382.

Hornak, V., et al. (2006). Comparison of multiple Amber force fields and development of improved protein backbone parameters. Proteins **65**: 712-725.

Jennings, M.L., Howren, T.R., Cui, J., Winters, M., and Hannigan, R. (2007). Transport and regulatory characteristics of the yeast bicarbonate transporter homolog Bor1p. Am. J. Physiol. Cell Physiol. **293**: C448-C476.

Jones, D.T. (1999). Protein secondary structure prediction based on position-specific scoring matrices. J. Mol. Biol. **292**: 195-202.

Jones, D.T., Taylor, W.R., and Thornton, J.M. (1994). A model recognition approach to the prediction of all-helical membrane protein structure and topology. Biochemistry **33**: 3038-3049.

Jorgensen, W.L., Chandrasekhar, J., Madura, J.D., Impey. R.W., and Klein, M.L. (1983). Comparison of simple potential functions for simulating liquid water. J Chem Phys **79**: 926-935.

Kirby, N.M., et al. (2013). A low-background-intensity focusing small-angle X-ray scattering undulator beamline. J. App. Cryst. **46**: 1670-1680.

Kynde, S.A., et al. (2014). Small-angle scattering gives direct structural information about a membrane protein inside a lipid environment. Acta Crystallogr D Biol Crystallogr **70**: 371-383.

Laaksonen, L. (1992). A graphics program for the analysis and display of molecular dynamics trajectories. J. Mol. Graph. **10**: 33-34.

Laskowski, R.A., MacArthur, M.W., Moss, D.S., and Thornton, J.M. (1993). PROCHECK: a program to check the stereochemical quality of protein structures. J. Appl. Cryst. **26**: 283-291.

Lee, J.-G., and Friesner, R.A. (1993). Atomic charges for large molecules derived from electrostatic potentials: fragment density matrix approach. J. Phys. Chem. **97**: 3515-3519.

Lee, J.-G., Lee. Y.S., and Roland, C. (2008). Structural determination of large molecules through the reassembly of optimized fragments. J. Mol. Graphics Model. **27**: 364-375.

Liu, J., Lai, Z.F., Wang, X.D., Tokutomi, N., and Nishi, K. (1998). Inhibition of sodium current by chloride channel blocker 4,4'-diisothiocyanatostilbene-2,2'-disulfonic acid (DIDS) in guinea pig cardiac ventricular cells. J. Cardiovasc. Pharmacol. **31**: 558-567.

Lu, F., et al. (2011). Structure and mechanism of the uracil transporter UraA. Nature **472**: 243-245.

Magdy, M., Monsur, F., van Hasselt, P.R., and Kuiper, P.J.C. (1994). Plasma membrane lipid alterations induced by NaCl in winter wheat roots. Physiol. Plant. **92**: 473-478.

Nakagawa, Y., et al. (2007). Cell-type specificity of the expression of Os BOR1, a rice efflux boron transporter gene, is regulated in response to boron availability for efficient boron uptake and xylem loading. Plant Cell **19**: 2624-2635.

Nordén, K., et al. (2011). Increasing gene dosage greatly enhances recombinant expression of aquaporins in Pichia pastoris. BMC Biotechnol. **11**: 47.

Nugent, T., and Jones, D.T. (2009). Transmembrane protein topology prediction using support vector machines. BMC Bioinformatics **10**: 159.

Nugent, T., Ward, S., and Jones, D.T. (2011). The MEMPACK α-helical transmembrane protein structure prediction server. Bioinformatics **27**: 1438-1439.

Pallotta, M., et al. (2014). Molecular basis of adaptation to high soil boron in wheat landraces and elite cultivars. Nature, doi:10.1038/nature13538.

Pabst, G. (2006). Global properties of biomimetic membranes: Perspectives on molecular features Biophys. Biophys. Rev. Lett. **1**: 57-84.

Pabst, G.M., Rappolt, M., Amenitsch, H., and Laggner, P. (2000). Structural information from multilamellar liposomes at full hydration: full q-range fitting with high quality x-ray data. Phys. Rev. E **62**: 4000-4009.

Park, M., Li, Q., Shcheynikov, N., Zeng, W., and Muallem, S. (2004). NaBC1 is a ubiquitous electrogenic Na^+-coupled borate transporter essential for cellular boron homeostasis and cell growth and proliferation. Mol. Cell **16**: 331-342.

Periasamy, A., et al. (2013). Cell-free protein synthesis of membrane (1,3)-β-D-glucan (curdlan) synthase: co-translational insertion in liposomes and reconstitution in nanodiscs. Biochim Biophys Acta - Biomembranes **1828**: 743-757.

Petoukhov, M.V., et al. (2012). New developments in the ATSAS program package for small-angle scattering data analysis. J. Appl. Crystal. **45**: 342-350.

Phan, J., et al. (2002). Structural basis for the substrate specificity of tobacco etch virus protease. J. Biol. Chem. **277**: 50564-50572.

Rath, A., Glibowicka, M., Nadeau, V.G., Chen, G., and Deber, C.M. (2009). Detergent binding explains anomalous SDS-PAGE migration of membrane proteins. Proc. Natl. Acad. Sci. USA **106**: 1760-1765.

Reid, R.J. (2007). Identification of boron transporter genes likely to be responsible for tolerance to boron toxicity in wheat and barley. Plant Cell. Physiol. **48**: 1673-1678.

Saier, M.H., Reddy, V.S., Tamang, D.G., and Vastermark, A. (2014). The transporter classification database Nucleic Acids Res. **42**: D251-D258.

Sasaki, S., Ishibashi, K., Nagai, T., and Marumo, F. (1992). Regulation mechanisms of intracellular pH of Xenopus laevis oocyte. Biochim, Biophys. Acta **1137**: 45-51.

Schneider, C.A., Rasband, W.S., and Eliceri, K.W. (2012). NIH Image to ImageJ: 25 years of image analysis. Nature Meth. **9**: 671-675.

Shadiac, N., Nagarajan, Y., Waters, S., and Hrmova, M. (2013). The close allies in membrane protein research: cell-free synthesis and nanotechnology. Mol. Membr. Biol. **30**: 229-245.

Sippl, M.J. (1993). Recognition of errors in three-dimensional structures of proteins. Proteins **17**: 355-362.

Skjevik, Å.A., Madej, B.D., Walker, R.C., and Teigen, K. (2012). LIPID11: A modular framework for lipid simulations using amber. J. Phys. Chem. B **116**: 11124-11136.

Steller, L., Krier, M., and Salzer, R. (2012). Natural and artificial ion channels for biosensing platforms. Anal. Bioanal. Chem. **402**: 209-230.

Sutton, T., et al. (2007). Boron-toxicity tolerance in barley arising from efflux transporter amplification. Science **318**: 1446-1449.

Takano, J., et al. (2002). Arabidopsis boron transporter for xylem loading. Nature **420**: 337-340.

Takano, J., et al. (2010). Polar localization and degradation of Arabidopsis boron transporters through distinct trafficking pathways. Proc. Natl. Acad. Sci. USA **107**: 5220-5225.

Virkki, L.V., Murer, H., and Forster. I.C. (2006). Voltage clamp fluorometric measurements on a type II Na^+-coupled Pi cotransporter: shedding light on substrate binding order. J. Gen. Phys. **127**: 539-555.

Wagner, M., Adamczak, R., Porollo, A., and Meller, J. (2005). Linear regression models for solvent accessibility prediction in proteins. J. Comp. Biol. **12**: 355-369.

White, S.H., and von Heijne, G. (2004). The machinery of membrane protein assembly. Curr. Opin. Struct. Biol. **14**: 397-404.

Zhang, Y. (2008). I-TASSER server for protein 3D structure prediction. BMC Bioinformatics **9**: 40-48.

Zhao, R., and Reithmeier, R.A.F. (2001). Expression and characterization of the anion transporter homologue YNL275w in Saccharomyces cerevisiae. Am. J. Physiol. Cell Physiol. **281**: C33-C45.

Figure Legends

Figure 1. *In silico* 3D model of HvBot1 and its trimeric assembly.

(A) The HvBot1 model viewed from the membrane plane and **(B)** from the cell interior revealing 13 membrane α-helices (pink and green) and five short α-helices (blue); views in panels A and B are related by 90^o about the horizontal axis. **(C)** The structure of HvBot1 embedded in a DOPC bilayer. DOPC lipids surrounding HvBot1 are within 8 Å distance. The lipid bilayer thickness is between 28-29 Å. **(D)** Details of a Na^+-binding site with six residues N63 (carbonyl O, OD1), T68 (carbonyl O, OG1), E70 (OE1 and OE2), T71 (OG1), Q113 (OE1) and G117 (carbonyl O). **(E)** Predicted trimeric assembly of HvBot1 with the lowest total energy (Supplemental Table 1) viewed from the cell interior (left) or from the membrane plane (90^o rotation of the left panel to the viewer) (right). The top right-hand side protomer is

coloured as in panel A. Two remaining protomers are in cyan and yellow with intracellular α-helices coloured blue.

Figure 2. Motion of Na^+ and associated oxygen atoms near the pore-forming region of HvBot1.

Top panels 1-3. A side view of the atomistic model of HvBot1 with a Na^+ ion trapped by six residues (N63, T68, E70, T71, Q113 and G117). Separations of five oxygen-bonding atoms of N63 (OD1), T68 (OG1), E70 (OE1 and OE2) and T71 (OG1) and Na^+ ion were identified at distances of 2.5 Å to 3.5 Å for most of 84 ns MD simulation, while four other oxygen-bonding partners N63 (carbonyl O), T71 (carbonyl O), Q113 (OE1), G117 (carbonyl O) were at distances of 4.1 Å to 5.2 Å for more than half of the simulation time. The cyan sphere denotes the Na^+ ion, and small red spheres represent nine oxygen-bonding atoms. The size of the Na^+ ion is enhanced for clarity.

Bottom panels 1-3. A top view of the atomistic model of HvBot1 with a Na^+ ion trapped by six residues (N63, T68, E70, T71, Q113 and G117).

Figure 3. WG-CFPS of HvBot1 and expression of HvBot1 in *P. pastoris*.

(A) Left (SDS-PAGE) and middle (WIB) of translation reactions with mRNA of HvBot1 and DMPC (lanes 2), or asolectin (lanes 3) liposomes. Lanes 1 contain the reaction lacking HvBot1 mRNA. The black arrows indicate mono- (1-mer), di- (2-mer) and tri-mers (3-mer). Right bottom: Yields of 1- to 3-mers were quantified by ImageJ (Schneider et al., 2012). The values of standard error of the mean (SEM, n=3) were calculated using GraphPad Prism 6 (La Jolla, California, USA). Right top: Asolectin liposomes with HvBot1 (large white arrow) separated by blue native PAGE. 1- to 3-mers (small white arrows) were detected by WIB after excision of HvBot1 (molecular mass of around 1,200 kDa). **(B)** WIB of HvBot1 solubilized and purified from the mixed-membrane fraction of methanol-induced *P. pastoris* (lane 1). The black arrows indicate 1- to 3-mers. Monomeric HvBot1 migrates to a 65-70 kDa region on SDS-PAGE gels. St. in kDa indicates molecular masses.

Figure 4. SAXS global analysis of HvBot1 liposomes bilayer profiles.

Fits of modelled bilayer electron density profiles to experimental SAXS data for empty (open circles) and HvBot1-inserted (full circles) **(A)** DMPC liposomes, and **(B)** asolectin liposomes. I(q) represents the scattering intensity and q is the magnitude of the reciprocal space momentum transfer vector. Insets show the corresponding bilayer electron density profiles of empty (solid lines) and HvBot1-inserted (dashed lines) liposomes, where the bilayer electron density, $\boldsymbol{\rho}$ is plotted on the vertical axis against the distance from the centre of the bilayer, $\boldsymbol{z}$ on the horizontal axis.

Figure 5. AFM imaging of HvBot1 liposomes.

AFM images (0.8 x 0.8 μm) of **(A)** DMPC liposomes, **(B)** DMPC liposomes from WG-CFPS lacking HvBot1 mRNA, and **(C)** DMPC liposomes from WG-CFPS with HvBot1 mRNA, fused on mica. The HvBot1 protein is observed only in panel C (white arrows); insert shows a representative bilayer protrusion. **(D)** Frequency histogram of the heights of bilayer protrusions. The majority of protrusions are between 1.5 to 1.9 nm in height. Scale bars (A-C) and insert scale bar (C) represent 200 nm. Z scales are 5 nm (A, B) and 7.2 nm (C). Minimum pixel resolution was (≤1 μm x ≤1 μm; 512 x 512) for all images. Cross-sections were drawn across the center point of each protrusion (n=95) using the DP software (JPK Instruments AG, Berlin, Germany) and the maximum height values relative to the bilayer surface were recorded. Individual height values were allocated within the predefined bin ranges using Microsoft Excel 2010.

Figure 6. Inward borate anion currents mediated by HvBot1 expressed in *X. laevis* oocytes.

Voltage-dependent ion currents in *X. laevis* oocytes injected with HvBot1 cRNA in solutions buffered to **(A)** pH 7.0 (circles), **(B)** pH 8.0 (triangles) and **(C)** pH 9.0 (squares) in the presence of 25 mM external boric acid, or **(D)** in water-injected oocytes. The solutions had the same osmotic pressure as the control bath solution (no boric acid added). Subtracted data for currents in the presence of boric acid less currents in the absence of boric acid for each oocyte (n=4 for water-injected, n=5 for Hv*Bot1*-gene-injected oocytes) were fitted to the 3rd order polynomial functions.

Figure 7. Transport properties of HvBot1 using patch-clamped proteo-liposomes**.**

(A) Membrane potential dependence on unitary current fluctuations of HvBot1 with 25 mM boric acid and holding potentials between +100 mV and -60 mV. The data below the horizontal line show inhibition of permeation by 80 µM 4'-diisothiocyano-2,2'-stilbenedisulfonic acid (DIDS). **(B)** and **(C)**, Dependence of conductance on boric acid (external side with 0.085-1.275 mM) at holding potentials between +100 mV and -100 mV. The reversal potentials are indicated. K_m and G_{max} were derived from conductance dependences on 0.085-1.275 mM borate concentrations. **(D)** Dependence of conductance on symmetric (25 mM) concentrations of chloride, phosphate, nitrate and sulphate anions. **(E)** Dependence of conductance on symmetric (25 mM) concentrations of boric acid and sodium glutamate (2.5-25 mM). The values of the standard error of the mean (SEM, n=3) shown in panels B, C, D and E are 9%, 1%, 8% and 20%, respectively, and were calculated using GraphPad Prism 6.

Supplemental Data

Supplemental Figure 1. A Time *versus* distance (in Å) profile of nine oxygen atoms that coordinate Na^+ during 84 ns MD simulation of HvBot1. The separations of oxygen-bonding atoms of six residues N63 (carbonyl O and OD1), T68 (carbonyl O and OG1), E70 (OE1 and OE2), T71 (OG1), Q113 (OE1) and G117 (carbonyl O) with Na^+ are at distances between 2.5 Å and 6.3 Å during MD simulation. The length of running average values represents 40 points.

Supplemental Figure 2. Properties and conservation of HvBot1. **(A)** The 3D model of HvBot1 viewed from the membrane plane with a predicted permeation pore determined with MOLE 2.0 (Berka et al., 2012). **(B)** Molecular surface morphologies of HvBot1 coded by electrostatic potentials in two orientations (left panel-front side, right panel-back side; views are related by 180^o about the horizontal axis). Blue and red patches denote electropositive and electronegative patches contoured at ±3 kTe^{-1}, respectively. **(C)** Conservation of the HvBot1 structure and **(D)** the Na^+-binding site with six amino acid (AA) residues N63, T68, E70, T71, Q113 and G117. **(E)** Conservation scores are expressed as the Confidence Interval Colour parameters (CIC), where scales represent the lower and upper bounds of the intervals

(Celniker et al., 2013). Burgundy and turquois colours are the extremes of conservation on the scale 9=conserved and 1=variable, respectively. The Figure was created in PyMOL.

Supplemental Figure 3. WG-CFPS of HvBot1 in the presence of liposomes and surfactants. SDS-PAGE of translation reactions with HvBot1 mRNA supplemented with **(A)** liposomes prepared from POPC, POPE, DMPC, POPC:POPE:POPG:cholesterol=6:3:1:0.1 and asolectin, and **(B)** sufactants and surfactant peptides. Arrows indicate monomeric HvBot1. **(C)** Yields of mono-, di- and trimeric forms HvBot1 with lipids or **(D)** surfactants and surfactant peptides were quantified with ImageJ (Schneider et al., 2012). The values of SEM are based on triplicates.

Supplemental Figure 4. Subcellular localisation of chimeric HvBot1-GFP in *P. pastoris* and after transient expression in onion cells, evaluated by confocal imaging. **(A)** Live bio-imaging of *P. pastoris* expressing HvBot1-GFP: (left) cells stained with DAPI (4',6-diamidino-2-phenylindole), (middle) GFP fluorescence of cells, (right) a phase contrast image of cells. The scale bar indicates 0.5 µm. **(B)** Confocal image of an onion epidermal cell transiently expressing HvBot1-GFP. Plasma membrane localisation was confirmed after partial plasmolysis showing a retracting plasma membrane and Hechtian strands (black arrow).

Supplemental Figure 5. Predicted spatial dispositions of protomers in quaternary assemblies of HvBot1. **(A)** Predicted dimeric (D1-D3) and **(B)** predicted trimeric (T1-T3) assemblies of HvBot1 with the lowest total energies (Supplemental Table 1) viewed from the cell interior (left panels) or from the membrane plane (right panels); left and right views are related by 90^{o} about the horizontal axis. One of the protomers is coloured as specified in Figure 1A, and remaining protomers in dimers and trimers are in cyan, and cyan and yellow, respectively, with intracellular α-helices coloured blue.

Supplemental Figure 6. Transport of borate anions by HvBot1 proteo-liposomes analyzed by stopped-flow light scattering. A pH-sensitive dye biscarboxyfluorescein (BCECF) incorporated in liposomes serves as an indicator of transport function. Stopped-flow light scattering measurements with 100 mM boric acid, recorded in fluorescence units with proteo-liposomes (circles) and liposomes lacking HvBot1 (triangles).

Supplemental Figure 7. Multiple sequence alignment of HvBot1 with nine closely related putative plant transport proteins belonging to the AE 2.A.31 family. Sequences were aligned with ProMals3D (http://prodata.swmed.edu/promals3d/promals3d.php) to illustrate their structural conservation. UniProt or GenBank (Ta*Bot-B5b*) accession numbers for entries in the consecutive order are A9XTK3, I1NKR0, KF148625, B9RB14, H2KX48, M5XLJ9, Q8VYR7, A5JUZ5, K4AVY8 and G7IKZ7. HvBot1 (*Hordeum vulgare*), related TaBot-B5b (*Triticum aestivum*) and AtBor1 (*Arabidopsis thaliana*) are marked in bold fonts. Conservation of residues on a scale of 9-5 is shown above the sequences (Supplemental Figure 2). Absolutely conserved and similar residues are indicated in brown and black, respectively. The position of the Na^+-binding site is marked. Burgundy and light burgundy box shading denotes absolutely conserved (E70) and moderately conserved (T68 and T71) residues, while light cyan and cyan box shading denotes less conserved (Q113 and G117) and the least conserved (N63) residues. Positions and conservation of seven membrane pore-forming (pink) and other membrane (green) α-helices, and five intracellular α-helices (blue) are indicated and marked by "h" lettering shaded in pink underneath the sequences.

Supplemental Figure 8. Schematic representation of a bilayer observable by AFM. **(A)** HvBot1 (drawn for simplicity as a monomer), embedded in a liposome, is illustrated by a filled blue rectangle (transmembrane α-helices) with a circle (sombrero of five intracellular α-helices; Fig. 1A), and C- and N-termini facing luminal and surface orientations, respectively. After a liposome with HvBot1 opens, HvBot1 is detectable predominantly in a single orientation by AFM, where large protrusions of 1.7 nm in height (corresponding to a sombrero component and a C-terminus) extend beyond the surface of the bilayer. A cartoon of the HvBot1 model (coloured as described in Fig. 1A) accommodated in a bilayer is also shown. **(B)** Primary structure of N-terminally 6xHis-tagged HvBot1 synthesized *via* WG-CFPS, and topology of HvBot1 in DMPC liposomes investigated by proteolytic cleavage with TEV. A WIB profile, using a mouse anti 6xHis monoclonal antibody (His) or a crude serum raised against a peptide derived from HvBot1 (HvBot1). Lanes 1 and 2 indicate incubation mixtures without or with TEV protease, respectively. Arrow indicates monomeric HvBot1. TEV protease of molecular mass of around 27 kDa is also detectable. St. in kDa indicates molecular masses.

Supplemental Table 1. Total energies of simulated dimeric D1-D3 and trimeric T1-T3 supra-molecular assemblies of HvBot1. The data comprise bonding, angular, dihedral angular and solvation energies, and van der Waals and electrostatic terms)**.**

Supplemental Table 2. Bilayer phospholipid head-group distances determined from a global fit of the SAXS data using ULV and MCT (asolectin) and MCT (DMPC) models.

Supplemental Table 3. Primers used for cloning of HvBot1.

Supplemental Table 1. Total energies of simulated dimeric D1-D3 and trimeric T1-T3 supra-molecular assemblies of HvBot1**.**

	Total energy of oligomers (kcal/mole)[a]		
	1	**2**	**3**
Dimer	-34,277	-34,194	-34,320
Trimer	-51,352	-51,288	-51,320

[a] Data comprise bonding, angular, dihedral angular and solvation energies, and van der Waals and electrostatic terms.

Supplemental Table 2. Bilayer phospholipid head-group distances determined from a global fit of the SAXS data using ULV and MCT (asolectin) and MCT (DMPC) models.

Sample	Distances[a]				
	z_H nm	σ_H nm	σ_C nm	ρ_C arbitrary units	d_{HH} nm
Asolectin	2.01 ± 0.01	0.30 ± 0.01	0.44 ± 0.04	-1.06 ± 0.08	4.02 ± 0.01
	1.99 ± 0.01	0.30 ± 0.01	0.60 ± 0.05	-0.77 ± 0.01	3.98 ± 0.01
Asolectin with HvBot1	1.82 ± 0.01	0.30 ± 0.01	1.19 ± 0.02	-0.55 ± 0.01	3.64 ± 0.01
	1.83 ± 0.01	0.30 ± 0.01	1.19 ± 0.01	-0.55 ± 0.01	3.66 ± 0.01
DMPC	1.78 ± 0.02	0.30 ± 0.01	0.40 ± 0.01	-1.20 ± 0.01	3.56 ± 0.02
DMPC with HvBot1	1.60 ± 0.01	0.30 ± 0.01	0.62 ± 0.01	-1.20 ± 0.01	3.20 ± 0.01

[a] The z_H, σ_H, σ_C, and ρ_C parameters denote the positions of the head-group Gaussian of the electron density profile, the width of the head-group Gaussian, the width of the Gaussian describing the hydrocarbon tails, and the amplitude of the tail Gaussian relative to that of the head-group Gaussian, respectively. $d_{HH}=2\times z_H$ is the phospholipid head-group distance taken to be the approximate bilayer thickness.

Supplemental Table 3. Primers used for cloning of HvBot1.

Task	**Plasmid**[a]	**Primers**
WG-CFPS	6xHis-TEV-HvBot1-pEU	F:AA*CTCGAG*AAAATGTCTGATCTACTGAGGAACCCCTTC restriction endonuclease: Xho1 R:AA*GCGGCCGC*TCACACGCTTGGCTGAACGGCATTTG restriction endonuclease: Not1
P. pastoris	6xHis-HvBot1-pPICZ-B	F:AA*CTCGAG*AAAATGTCTCATCATCATCATCATCATGAGAATCTCTATTTCCAAGGAATGGATCTACTGAGGAACCCCTTC restriction endonuclease: Xho1 R:AA*GCGGCC*GCTCACACGCTTGGCTGAACGGCATTTG restriction endonuclease: Not1
P. pastoris - confocal imaging	1. Step: cloning of GFP-10xHis-pPICZ-B 2. Step: cloning of HvBot1-TEV-GFP-10xHis-pPICZ-B	F:TGA*GCGGCCGC*GAAAATTTATATTTTCAAGGT restriction endonuclease: Not1 R:AA*GCGGCC*GCTCACACGCTTGGCTGAACGGCATTTG restriction endonuclease: Not1 F:TAC*CTCGAGA*AAATGTCTGATCTACTGAGGAACCCC restriction endonuclease: Xho1 R:GTA*GCGGCCGC*ACACGCTTGGCTGAACGGCAT restriction endonuclease: Not1
X. laevis - oocytes and onion cells	pCR8-HvBot1	F: ATGGATCTACTGAGGAACCCCTTCAR R: TCACACGCTTGGCTGAACGGCATTT

[a]All DNA fusions were sequenced in both directions and were found to be correct

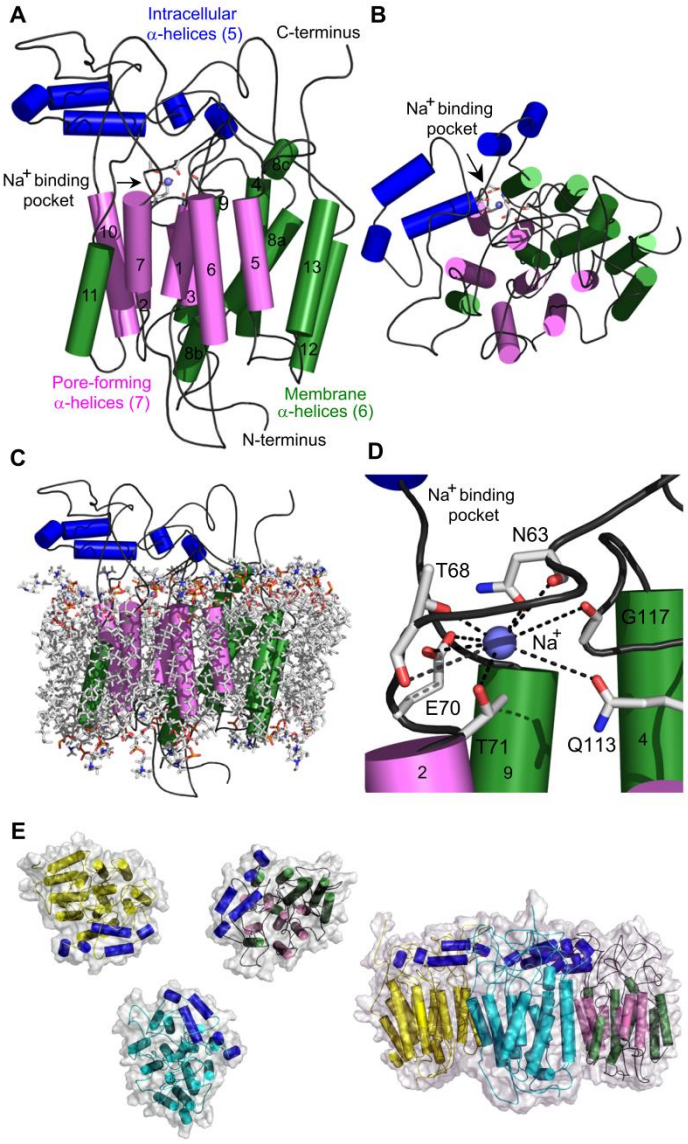

Figure 1. *In silico* 3D model of HvBot1 and its trimeric assembly.

(A) The HvBot1 model viewed from the membrane plane and **(B)** from the cell interior revealing 13 membrane α-helices (pink and green) and five short α-helices (blue); views in panels a and b are related by 90o about the horizontal axis. **(C)** The structure of HvBot1 embedded in a DOPC bilayer. DOPC lipids surrounding HvBot1 are within 8 Å distance. The lipid bilayer thickness is between 28-29 Å. **(D)** Details of a Na^+-binding site with six residues N63 (carbonyl O, OD1), T68 (carbonyl O, OG1), E70 (OE1 and OE2), T71 (OG1), Q113 (OE1) and G117 (carbonyl O). **(E)** Predicted trimeric assembly of HvBot1 with the lowest total energy (Supplemental Table 1) viewed from the cell interior (left) or from the membrane plane (90o rotation of the left panel to the viewer) (right). The top right-hand side protomer is coloured as in panel A. Two remaining protomers are in cyan and yellow with intracellular α-helices coloured blue.

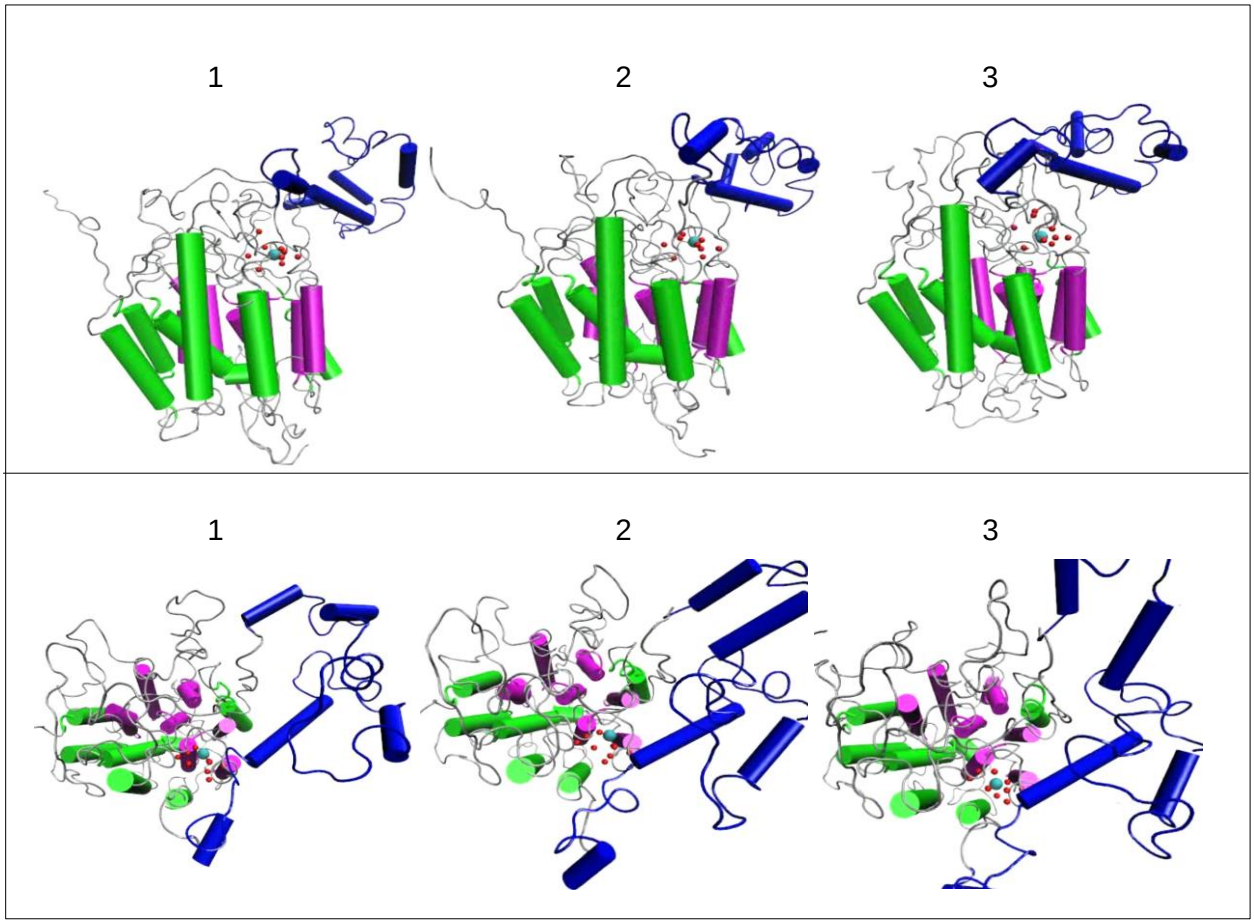

Figure 2. Motions of Na+ and associated oxygen atoms near the pore-forming region of HvBot1.

Top panels 1-3. A side view of the atomistic model of HvBot1 with a Na+ ion trapped by six residues (N63, T68, E70, T71, Q113 and G117). Separations of five oxygen-bonding atoms of N63 (OD1), T68 (OG1), E70 (OE1 and OE2) and T71 (OG1) and Na+ ion were identified at distances of 2.5 Å to 3.5 Å for most of 84 ns MD simulation, while four other oxygen-bonding partners N63 (carbonyl O), T71 (carbonyl O), Q113 (OE1), G117 (carbonyl O) were at distances of 4.1 Å to 5.2 Å for more than half of the simulation time. The cyan sphere denotes the Na+ ion, and small red spheres represent nine oxygen-bonding atoms. The size of the Na+ ion is enhanced for clarity.

Bottom panels 1-3. A top view of the atomistic model of HvBot1 with a Na+ ion trapped by six residues (N63, T68, E70, T71, Q113 and G117).

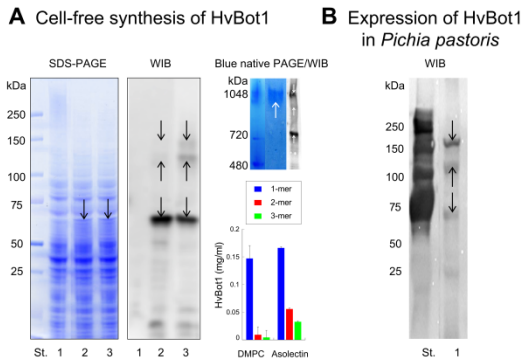

Figure 3. WG-CFPS of HvBot1 and expression of HvBot1 in *P. pastoris*.

(A) Left (SDS-PAGE) and middle (WIB) of translation reactions with mRNA of HvBot1 and DMPC (lanes 2), or asolectin (lanes 3) liposomes. Lanes 1 contain the reaction lacking HvBot1 mRNA. The black arrows indicate mono- (1-mer), di- (2-mer) and tri-mers (3-mer). Right bottom: Yields of 1- to 3-mers were quantified by ImageJ (Schneider et al., 2012). The values of standard error of the mean (SEM, n=3) were calculated using GraphPad Prism 6 (La Jolla, California, USA). Right top: Asolectin liposomes with HvBot1 (large white arrow) separated by blue native PAGE. 1- to 3-mers (small white arrows) were detected by WIB after excision of HvBot1 (molecular mass of around 1,200 kDa). **(B)** WIB of HvBot1 solubilized and purified from the mixed-membrane fraction of methanol-induced *P. pastoris* (lane 1). The black arrows indicate 1- to 3-mers. Monomeric HvBot1 migrates to a 65-70 kDa region on SDS-PAGE gels. St. in kDa indicates molecular masses.

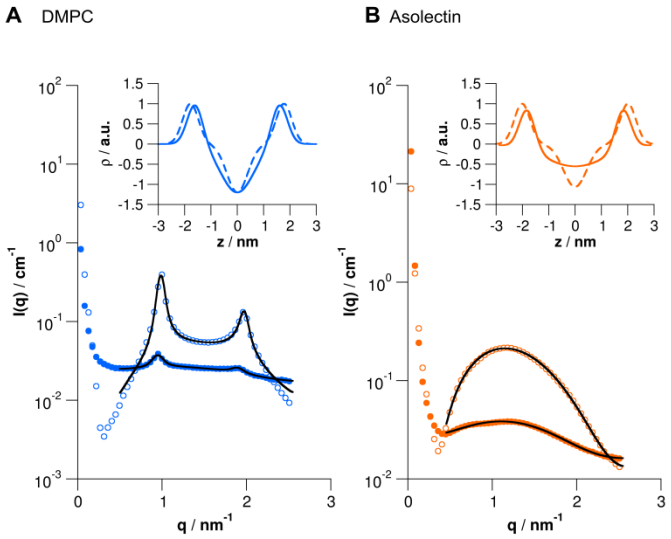

Figure 4. SAXS global analysis of HvBot1 liposomes bilayer profiles.

Fits of modelled bilayer electron density profiles to experimental SAXS data for empty (open circles) and HvBot1-inserted (full circles) **(A)** DMPC liposomes, and **(B)** asolectin liposomes. I(q) represents the scattering intensity and q is the magnitude of the reciprocal space momentum transfer vector. Insets show the corresponding bilayer electron density profiles of empty (solid lines) and HvBot1-inserted (dashed lines) liposomes, where the bilayer electron density, ρ is plotted on the vertical axis against the distance from the centre of the bilayer, z on the horizontal axis.

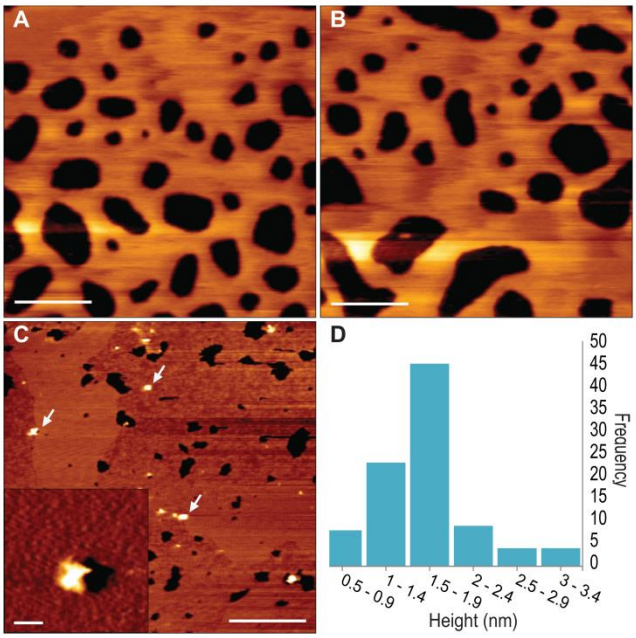

Figure 5. AFM imaging of HvBot1 liposomes.

AFM images (0.8 x 0.8 µm) of **(A)** DMPC liposomes, **(B)** DMPC liposomes from WG-CFPS lacking HvBot1 mRNA, and **(C)** DMPC liposomes from WG-CFPS with HvBot1 mRNA, fused on mica. The HvBot1 protein is observed only in panel c (white arrows); insert shows a representative bilayer protrusion. **(D)** Frequency histogram of the heights of bilayer protrusions. The majority of protrusions are between 1.5 to 1.9 nm in height. Scale bars (A-C) and insert scale bar (C) represent 200 nm. Z scales are 5 nm (A, B) and 7.2 nm (C). Minimum pixel resolution was (≤1 µm x ≤1 µm; 512 x 512) for all images. Cross-sections were drawn across the center point of each protrusion (n=95) using the DP software (JPK Instruments AG, Berlin, Germany) and the maximum height values relative to the bilayer surface were recorded. Individual height values were allocated within the predefined bin ranges using Microsoft Excel 2010.

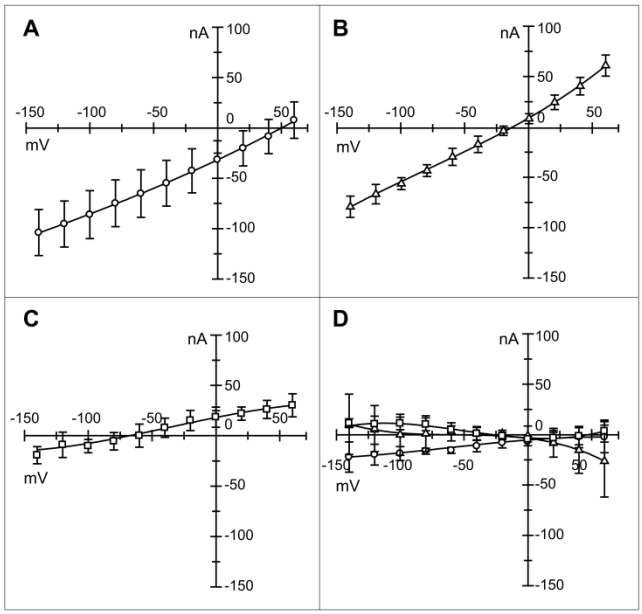

Figure 6. Inward borate anion currents mediated by HvBot1 expressed in *X. laevis* oocytes.

Voltage-dependent ion currents in *X. laevis* oocytes injected with HvBot1 cRNA in solutions buffered to **(A)** pH 7.0 (circles), **(B)** pH 8.0 (triangles) and **(C)** pH 9.0 (squares) in the presence of 25 mM external boric acid, or **(D)** in water-injected oocytes. The solutions had the same osmotic pressure as the control bath solution (no boric acid added). Subtracted data for currents in the presence of boric acid less currents in the absence of boric acid for each oocyte (n=4 for water-injected, n=5 for Hv*Bot1*-gene-injected oocytes) were fitted to the 3rd order polynomial functions.

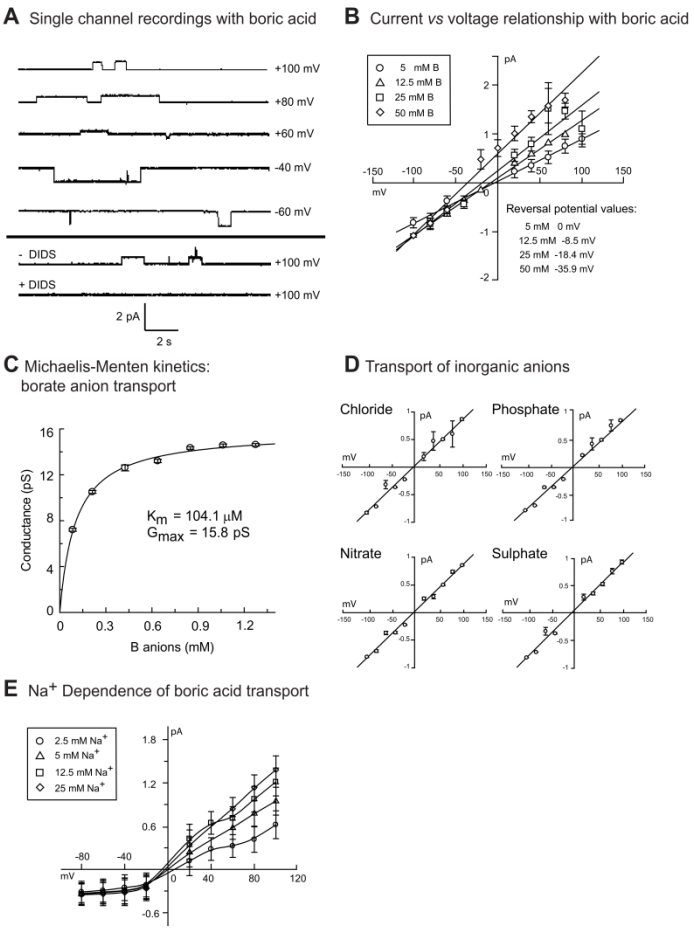

Figure 7. Transport properties of HvBot1 using patch-clamped proteo-liposomes.

(A) Membrane potential dependence on unitary current fluctuations of HvBot1 with 25 mM boric acid and holding potentials between +100 mV and -60 mV. The data below the horizontal line show inhibition of permeation by 80 µM 4'-diisothiocyano-2,2'-stilbenedisulfonic acid (DIDS). **(B)** and **(C)**, Dependence of conductance on boric acid (external side with 0.085-1.275 mM) at holding potentials between +100 mV and -100 mV. The reversal potentials are indicated. Km and Gmax were derived from conductance dependences on 0.085-1.275 mM borate concentrations. **(D)** Dependence of conductance on symmetric (25 mM) concentrations of chloride, phosphate, nitrate and sulphate anions. **(E)** Dependence of conductance on symmetric (25 mM) concentrations of boric acid and sodium glutamate (2.5-25 mM). The values of the standard error of the mean (SEM, n=3) shown in panels B, C, D and E are 9%, 1%, 8% and 20%, respectively, and were calculated using GraphPad Prism 6.

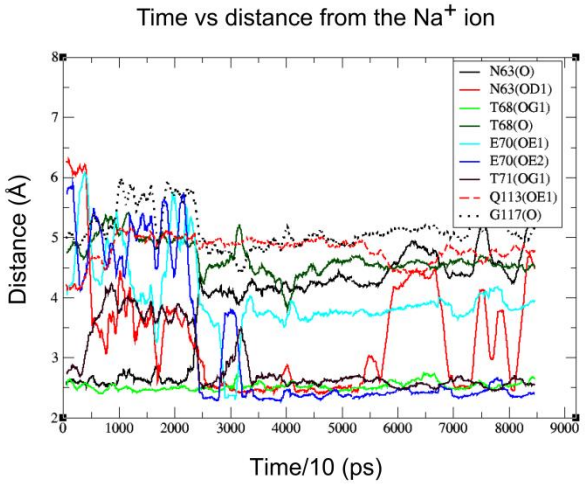

Supplemental Figure 1. A Time versus distance (in Å) profile of nine oxygen atoms that coordinate Na^+ during 84 ns MD simulation of HvBot1. The separations of oxygen-bonding atoms of six residues N63 (carbonyl O and OD1), T68 (carbonyl O and OG1), E70 (OE1 and OE2), T71 (OG1), Q113 (OE1) and G117 (carbonyl O) with Na^+ are at distances between 2.5 Å and 6.3 Å during MD simulation. The length of running average values represents 40 points.

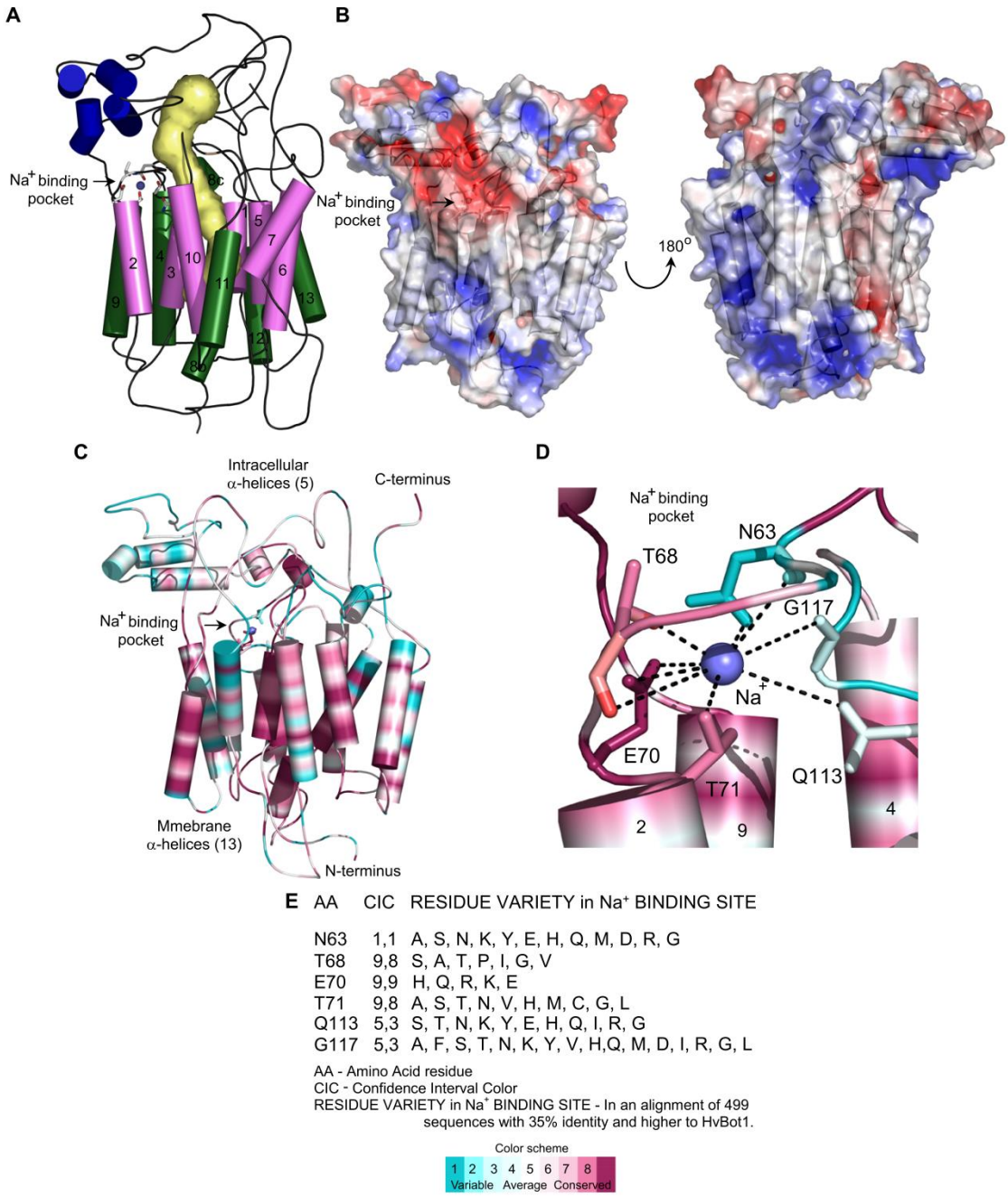

E AA CIC RESIDUE VARIETY in Na^+ BINDING SITE

N63	1,1	A, S, N, K, Y, E, H, Q, M, D, R, G
T68	9,8	S, A, T, P, I, G, V
E70	9,9	H, Q, R, K, E
T71	9,8	A, S, T, N, V, H, M, C, G, L
Q113	5,3	S, T, N, K, Y, E, H, Q, I, R, G
G117	5,3	A, F, S, T, N, K, Y, V, H,Q, M, D, I, R, G, L

AA - Amino Acid residue
CIC - Confidence Interval Color
RESIDUE VARIETY in Na^+ BINDING SITE - In an alignment of 499 sequences with 35% identity and higher to HvBot1.

Color scheme
1 2 3 4 5 6 7 8
Variable Average Conserved

Supplemental Figure 2. Properties and conservation of HvBot1. **(A)** The 3D model of HvBot1 viewed from the membrane plane with a predicted permeation pore determined with MOLE 2.0 (Berka et al., 2012). **(B)** Molecular surface morphologies of HvBot1 coded by electrostatic potentials in two orientations (left panel-front side, right panel-back side; views are related by 180º about the horizontal axis). Blue and red patches denote electropositive and electronegative patches contoured at ±3 kT/e, respectively. **(C)** Conservation of the HvBot1 structure and **(D)** the Na^+-binding site with six amino acid (AA) residues N63, T68, E70, T71, Q113 and G117. **(E)** Conservation scores are expressed as the Confidence Interval Colour parameters (CIC), where scales represent the lower and upper bounds of the intervals. (Celniker et al., 2013) Burgundy and turquois colours are the extremes of conservation on the scale 9=conserved and 1=variable, respectively. The Figure was created in PyMOL.

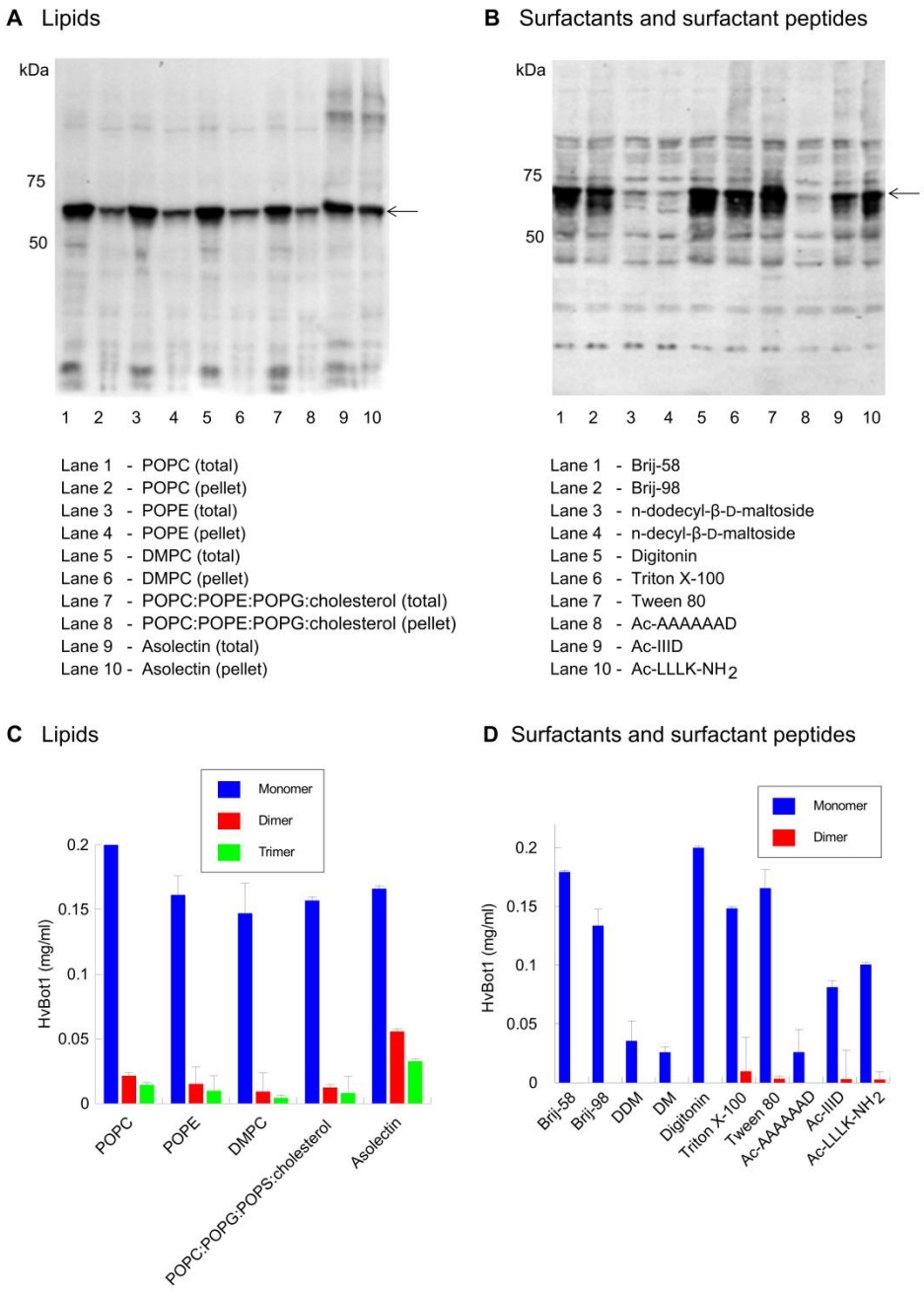

Supplemental Figure 3. WG-CFPS of HvBot1 in the presence of liposomes and surfactants. SDS-PAGE of translation reactions with HvBot1 mRNA supplemented with **(A)** liposomes prepared from POPC, POPE, DMPC, POPC:POPE:POPG:cholesterol=6:3:1:0.1 and asolectin, and **(B)** sufactants and surfactant peptides. Arrows indicate monomeric HvBot1. **(C)** Yields of mono-, di- and trimeric forms HvBot1 with lipids or **(D)** surfactants and surfactant peptides were quantified with ImageJ (Schneider et al., 2012). The values of SEM are based on triplicates.

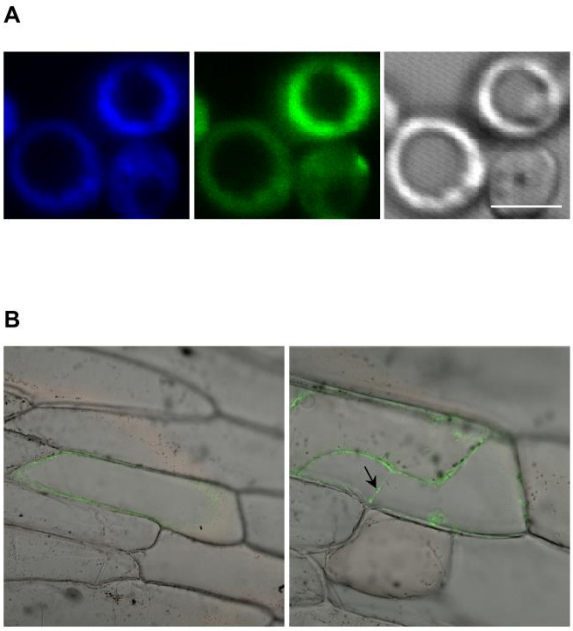

Supplemental Figure 4. Subcellular localization of chimeric HvBot1-GFP in *P. pastoris* and after transient expression in onion cells, evaluated by confocal imaging. **(A)** Live bio-imaging of *P. pastoris* expressing HvBot1-GFP: (left) cells stained with DAPI (4',6-diamidino-2-phenylindole), (middle) GFP fluorescence of cells, (right) a phase contrast image of cells. The scale bar indicates 0.5 µm. **(B)** Confocal image of an onion epidermal cell transiently expressing HvBot1-GFP. Plasma membrane localization was confirmed after partial plasmolysis showing a retracting plasma membrane and Hechtian strands (black arrow).

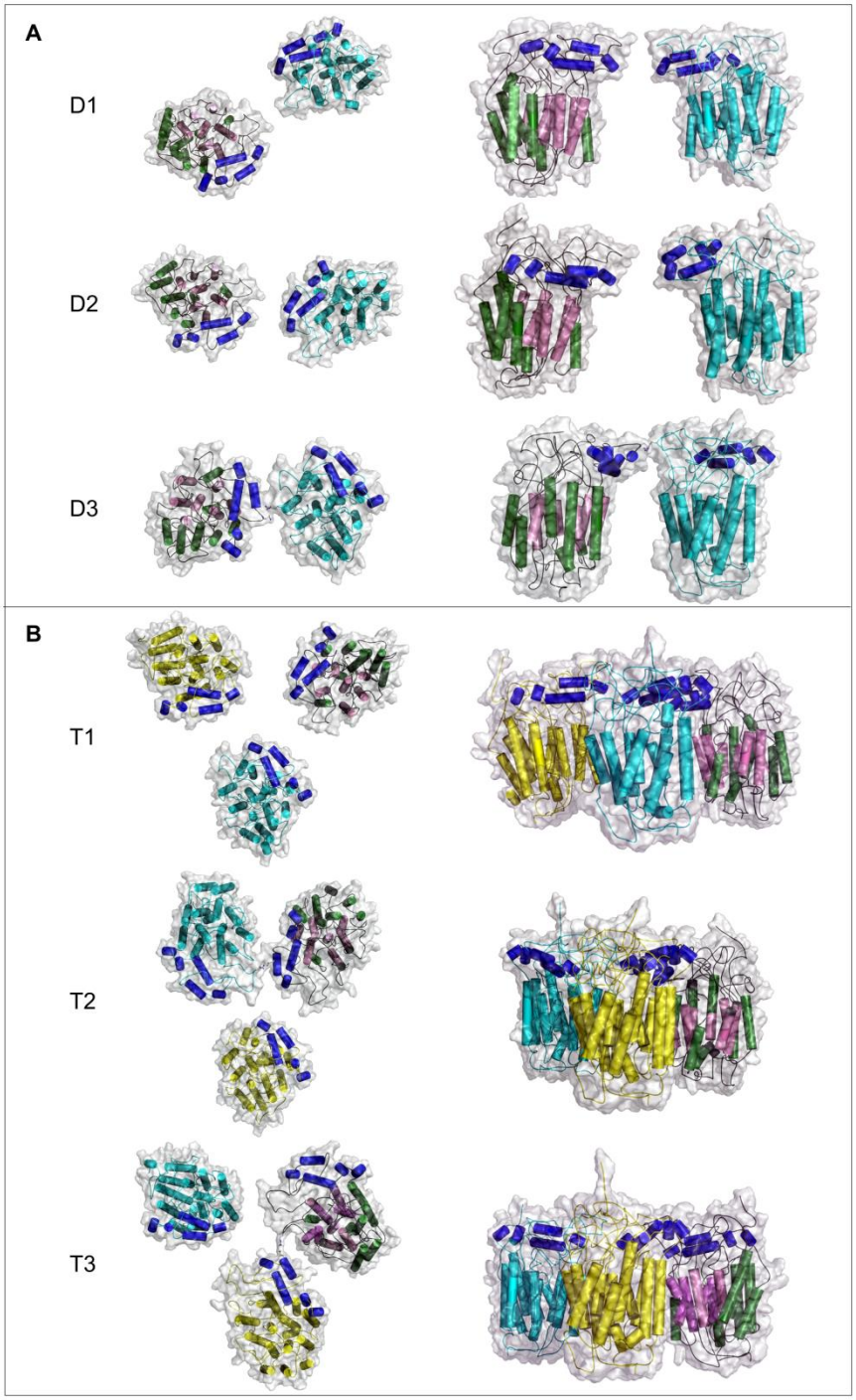

Supplemental Figure 5. Predicted spatial dispositions of protomers in quaternary assemblies of HvBot1. **(A)** Predicted dimeric (D1-D3) and **(B)** predicted trimeric (T1-T3) assemblies of HvBot1 with the lowest total energies (Supplemental Table 1) viewed from the cell interior (left panels) or from the membrane plane (right panels); left and right views are related by 90º about the horizontal axis. One of the protomers is coloured as specified in Figure 1A, and remaining protomers indimers and trimers are in cyan, and cyan and yellow, respectively, with intracellular α-helices coloured blue.

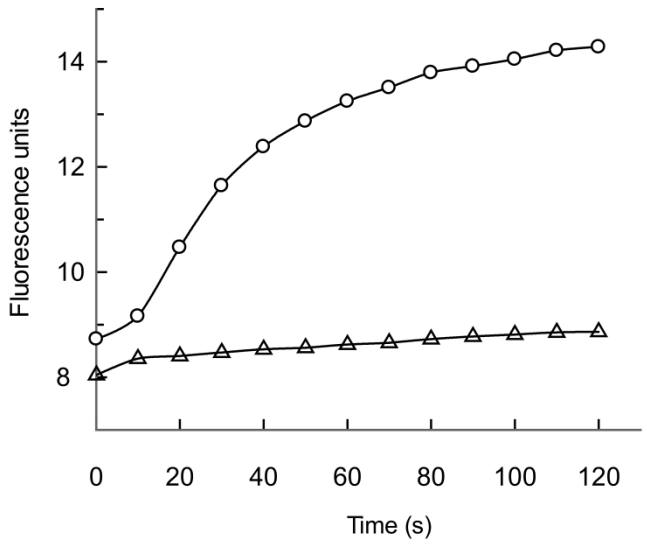

Supplemental Figure 6. Transport of borate anions by HvBot1 proteo-liposomes analyzed by stopped-flow light scattering. A pH-sensitive dye biscarboxyfluorescein (BCECF) incorporated in liposomes serves as an indicator of transport function. Stopped-flow light scattering measurements with 100 mM boric acid, recorded in fluorescence units with proteo-liposomes (circles) and liposomes lacking HvBot1 (triangles).

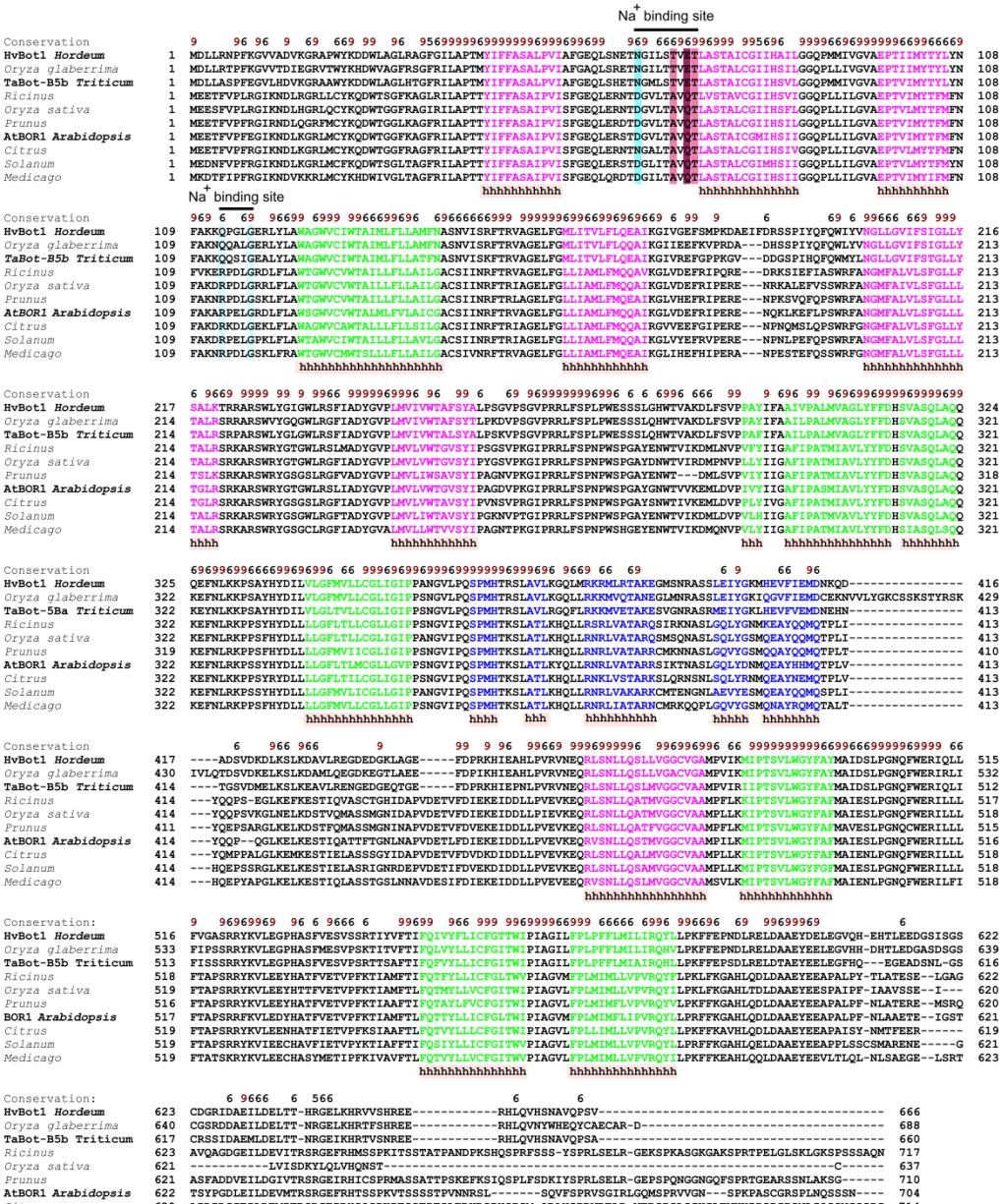

Supplemental Figure 7. Multiple sequence alignment of HvBot1 with nine closely related putative plant transport proteins belonging to the AE 2.A.31 family. Sequences were aligned with ProMals3D (http://prodata.swmed.edu/promals3d/promals3d.php) to illustrate their structural conservation. UniProt or GenBank (Ta*Bot-B5b*) accession numbers for entries in the consecutive order are A9XTK3, I1NKR0, KF148625, B9RB14, H2KX48, M5XLJ9, Q8VYR7, A5JUZ5, K4AVY8 and G7IKZ7. HvBot1 (*Hordeum vulgare*), related TaBot-B5b (*Triticum aestivum*) and AtBor1 (*Arabidopsis thaliana*) are marked in bold fonts. Conservation of residues on a scale of 9-5 is shown above the sequences (Supplemental Figure 2). Absolutely conserved and similar residues are indicated in brown and black, respectively. The position of the Na^+-binding site is marked. Burgundy and light burgundy box shading denotes absolutely conserved (E70) and moderately conserved (T68 and T71) residues, while light cyan and cyan box shading denotes less conserved (Q113 and G117) and the least conserved (N63) residues. Positions and conservation of seven membrane pore-forming (pink) and other membrane (green) α-helices, and five intracellular α-helices (blue) are indicated and marked by "h" lettering shaded in pink underneath the sequences.

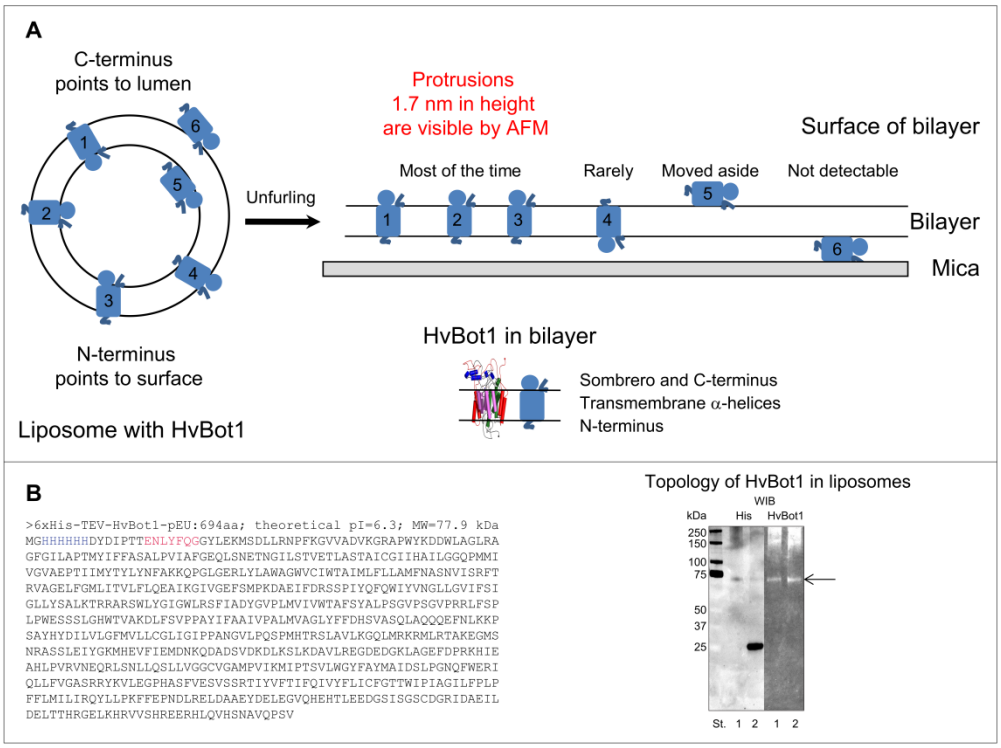

Supplemental Figure 8. Schematic representation of a bilayer observable by AFM. **(A)** HvBot1 (drawn for simplicity as a monomer), embedded in a liposome, is illustrated by a filled blue rectangle (transmembrane α-helices) with a circle (sombrero of five intracellular α-helices; Figure 1A), and C- and N-termini facing luminal and surface orientations, respectively. After a liposome with HvBot1 opens, HvBot1 is detectable predominantly in a single orientation by AFM, where large protrusions of 1.7 nm in height (corresponding to a sombrero component and a C-terminus) extend beyond the surface of the bilayer. A cartoon of the HvBot1 model (coloured as described in Figure 1A) accommodated in a bilayer is also shown. **(B)** Primary structure of N-terminally 6xHis-tagged HvBot1 synthesized *via* WG-CFPS, and topology of HvBot1 in DMPC liposomes investigated by proteolytic cleavage with TEV. A WIB profile, using a mouse anti 6xHis monoclonal antibody (His) or a crude serum raised against a peptide derived from HvBot1 (HvBot1). Lanes 1 and 2 indicate incubation mixtures without or with TEV protease, respectively. Arrow indicates monomeric HvBot1. TEV protease of molecular mass of around 27 kDa is also detectable. St. in kDa indicates molecular masses.

SIGNIFICANCE OF THE FINDINGS:

B toxicity is a major problem in southern and south-western regions of Australia, and has been identified as a problem in other important semi-arid regions such as Anatolia in Turkey. The likely future increases in cropping under irrigation using desalinated seawater or high B ground water potentially will see extension of the areas affected by B toxicity. Therefore it is of great importance to understand the roles of transporters that play a key role under low and high B conditions. This study gives a detailed understanding on the function of borate transporter HvBot1 at a molecular level and also describes its structural properties.

Chapter 4

CLOSE ALLIES IN MEMBRANE PROTEIN RESEARCH: CELL-FREE SYNTHESIS AND NANOTECHNOLOGY

Authors: Nadim Shadiac, Yagnesh Nagarajan, Shane Waters, Maria Hrmova

NUMBER OF CITATIONS: 4 (as of 19/12/14)

ABSTRACT

Membrane proteins control fundamental processes that are inherent to nearly all forms of life such as transport of molecules, catalysis, signaling, vesicle fusion, sensing of chemical and physical stimuli from the environment, and cell-cell interactions. Membrane proteins are harbored within a non-equilibrium fluid-like environment of biological membranes that separate cellular and non-cellular environments, as well as in compartmentalized cellular organelles. One of the classes of membrane proteins that will be specifically treated in this article are transport proteins of plant origin, that facilitate material and energy transfer at the membrane boundaries. These proteins import essential nutrients, export cellular metabolites, maintain ionic and osmotic equilibriums and mediate signal transduction. The aim of this article is to report on the progress of membrane protein functional and structural relationships, with a focus on producing stable and functional proteins suitable for structural and biophysical studies. We interlink membrane protein production primarily through wheat-germ cell-free protein synthesis (WG-CFPS) with the growing repertoire of membrane mimicking environments in the form of lipids, surfactants, amphipathic surfactant polymers, liposomes and nanodiscs that keep membrane proteins soluble. It is hoped that the advancements in these fields could increase the number of elucidated structures, in particular those of plant membrane proteins, and contribute to bridging of the gap between structures of soluble and membrane proteins, the latter being comparatively low.

SIGNIFICANCE OF THE FINDINGS

This article offers a comprehensive review of research in the field of plant membrane transport proteins, and membrane proteins (MP) in general. The paper details the importance of such research and the challenges associated with the production and characterisation of MP in the context of their structure and function relationships. Further, the paper focuses on the versatility of CF systems of protein synthesis and how they are uniquely beneficial for

MP research, when used in conjugation with membrane mimicking nanoparticles such as liposomes, nanodiscs, lipodiscs, *etc*., to define the structural and functional properties of MPs.

Statement of Authorship

Title of the paper	Close allies in membrane protein research: cell-free synthesis and nanotechnology
Publication status	Published
Publication Details	Shadiac, N., Nagarajan, Y., Waters, S., and Hrmova, M. (2013). Close allies in membrane protein research: Cell-free synthesis and nanotechnology. Molecular Membrane Biology 0, 1-17.

Authors Contribution

By signing the Statement of Authorship, each author certifies that their stated contribution to the publication is accurate and that permission is granted for the publication to be included in the candidate's thesis

Name of Principal Author (Candidate)	Nadim Shadiac		
Contribution to the paper	Designed and wrote paper		
Signature		Date	18/12/14

Name of Co-Author	Yagnesh Nagarajan		
Contribution to the paper	Designed and wrote paper		
Signature		Date	18/12/14

Name of Co-Author	Shane Waters		
Contribution to the paper	Designed and wrote paper		
Signature		Date	18-12-14

Name of Co-Author	Maria Hrmova		
Contribution to the paper	Designed and wrote paper		
Signature		Date	18-12-2014

Shadiac, N., Nagarajan, Y., Waters, S. & Hrmova, M. (2013) Close allies in membrane protein research: cell-free synthesis and nanotechnology. *Molecular Membrane Biology*, *30*(3), 229-245.

Statement of Authorship

Title of the paper	*In situ* functional incorporation of a plant membrane transporter into a tethered bilayer lipid membrane
Publication status	Publication style

Authors Contribution

By signing the Statement of Authorship, each author certifies that their stated contribution to the publication is accurate and that permission is granted for the publication to be included in the candidate's thesis

Name of Principal Author (Candidate)	Julius L. Zieleniecki
Contribution to the paper	Designed ,performed experiments, analysed data and wrote paper
Signature	Date 18th Dec 2014

Name of Co-Author	Yagnesh Nagarajan
Contribution to the paper	Designed ,performed experiments, analysed data and wrote paper
Signature	Date 18/12/14

Name of Co-Author	Jay Rongala
Contribution to the paper	Performed experiments
Signature	Date 18/12/2014

Name of Co-Author	Shane Waters
Contribution to the paper	Performed experiments
Signature	Date 18/12/14

Name of Co-Author	Maria Hrmova
Contribution to the paper	Designed ,analysed data and wrote paper
Signature	Date 18/12/2014

Name of Co-Author	Ingo Koeper
Contribution to the paper	Designed ,analysed data and wrote paper
Signature	Date 18/12/14

Chapter 5

IN SITU FUNCTIONAL INCORPORATION OF A PLANT MEMBRANE TRANSPORTER INTO A TETHERED BILAYER LIPID MEMBRANE

Julius L. Zieleniecki, Yagnesh Nagarajan, Jay Rongala, Shane Waters, Maria Hrmova and Ingo Köper

Introduction

Membrane proteins (MP) traditionally represent a difficult target to express, purify and investigate. One of the approaches to study MPs is to use tethered bilayer lipid membranes (tBLM), which represent a robust and electrically insulating bilayer membrane. Attachment to a surface allows for the use of a variety of surface analytical techniques, such as Atomic Force Microscopy (AFM) or Electrochemical Impedance Spectroscopy (EIS).

Functional incorporation of complex MP into a preformed bilayer is a challenging task. Two alternative approaches have been used so far: (i) when a protein can be purified and when it is stable and specific conditions are found to make it soluble in aqueous media, MP can be added directly to a preformed membrane bilayer. However, this is limited to rather simple protein structures. In addition, it is difficult to preserve function of MP after incorporation into the bilayer. (ii) A second approach involves expression of a membrane protein in bilayer mimetics such as liposomes, lipodiscs or nanodiscs to form the lipid bilayer. There have been examples of successfully using this approach, but again in most cases these approaches are limited to less complex protein structures.

A third alternative is a co-translational insertion of a MP directly into tBLM using a cell-free synthesis approach (He, 2008; Periasamy et al., 2013; Shadiac et al., 2013). WG-based cell free system (WG-CFS) enables rapid production of proteins and is a versatile method to express complex membrane proteins (Periasamy et al., 2013; Shadiac et al., 2013). It is an open system and allows supplementation of any component at any time of the CF reaction. It was originally developed to study transcription and translation processes but now it is used in a variety of studies stretching from basic research to large scale experiments (He, 2008). With rapid advancements in technology, the CF system can be used as a linking tool between biologist and nanotechnologist to address fundamental problems in basic science.

In this work, we have used CF synthesis to embed a plant membrane transport protein, HvBot1 into tBLM. This protein is expressed in plant roots and mediates tolerance to high boric acid (BA) in soils (Sutton et al., 2007; Pallotta et al., 2014). The predicted structure of the protein contains 13 membrane-spanning and five cytoplasmic α-helices. HvBot1 mediates transport of borate in a Na^+-dependant manner and shows channel-like characteristics (Nagarajan et al., unpublished).

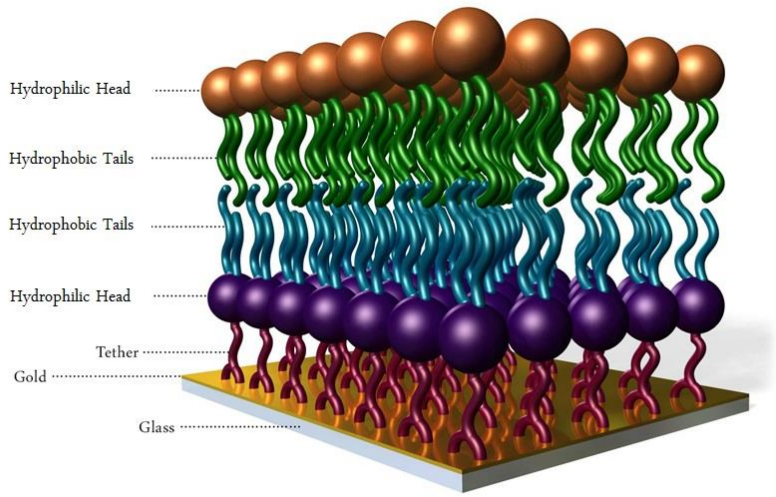

Figure 1: Schematic of tBLM produced for this work by Julius Zieleniecki.

Methods

The anchor lipid DPhyTL (2,3-di-O-phytanyl-sn-glycerol-1-tetraethylene glycol-d,L-α-lipoic acid ester) was synthesised as described (Vockenroth et al., 2008). DPhyTL was purified using column chromatography and its identity confirmed using NMR and thin-layer chromatography (TLC). DPhyPC was obtained from Avanti Polar Lipids (Alabaster, AL). Ultra-pure water filtered with a Millipore device (18.2 MΩ cm^2) was used throughout the experiments. EIS measurements were performed in either 0.1 M NaCl (Sigma-Aldrich, Australia 99.5%) or in the HEPES buffer containing 95 mM HEPES, 5 mM NaCl, and finally in the HEPES-borate buffer containing 10 mM HEPES, 85 mM BA and 5 mM NaCl, adjusted to pH 7.5 with NaOH.

Substrates

The heterogeneous substrates were prepared using a multistep procedure based on a template-stripping process. First, a silicon wafer was cleaned with basic piranha solution, followed by slow gold evaporation (50 nm).

Membrane assembly

DPhyTL monolayers were self-assembled on the gold films by immersion of the substrate in a lipid solution (0.2 mg/mL in ethanol) for 24 h. Before use, samples were cleaned with ethanol (Sigma-Aldrich, Munich, Germany) and dried under nitrogen. Monolayers were completed to bilayers by fusion with small unilamellar vesicles (50 nm by extrusion, 2 mg lipid per mL of 1 mM NaCl). The volume of 25 µL of 50 nm extruded vesicles was added to the pre-formed monolayers and each bilayer was left to form overnight (approximately 16 to 18 h).

Electrochemical Impedance Spectroscopy (EIS) measurements

Measurements were conducted using an AUTOLAB PGSTAT 30 impedance spectrometer. Three electrode measurements were performed in custom made Teflon cells, where the substrates were the working electrodes, a coiled platinum wire was the counter electrode, and ET072 leakless miniature Ag/AgCl electrode was the reference electrode (eDAQ Pty Ltd). Spectra were recorded for frequencies between 0.5 mHz and 1 MHz at a controlled potential with an AC modulation amplitude of 2 mV. Raw data was analysed using the ZVIEW software package (version 3.3B Scribner Associates). The chamber in the Teflon cells has a solution volume of 1 mL and an electrochemically active area on the substrates of 0.72 cm^2. The data fit was obtained using an equivalent circuit of capacitors and resistances. The final values are normalised to the electrode surface area. The electrochemical properties have been obtained by fitting the experimental data to an $R_{sol}(R_{bilayer}C_{bilayer})(R_{tether}CPE_{tether})$ equivalent circuit (Vockenroth et al., 2008).

Plasmid construction

The HvBot1 cDNA was amplified from the Sahara cultivar (Sutton et al., 2007) and cloned into the cell free pEU (frame N2) expression vector (Cell Free Sciences, Tsurumi-ku, Yokohama, Japan) containing a N-terminal 6xHis tag and a Tobacco-Etch Virus (TEV) proteolytic site.

Wheat-Germ Cell-Free Protein Synthesis (WG-CFPS) of HvBot1

WG-CFS of HvBot1 was performed in a decoupled system according to protocol described previously (Periasamy et al., 2013). Briefly, a transcription reaction was set up at 42^oC and transcribed mRNA was added to a Teflon impedance spectroscopy cell. HvBot1 protein synthesis was carried out for 24 h at room temperature.

Western Immuno-Blot (WIB) Analysis

After transport measurements were completed, an impedance spectroscopy cell was dismantled to remove the gold plate. The volume of 15 µl of 10% (w/v) sodium dodecyl sulphate (SDS) buffer was added to the gold plate until all lipids dissolved. Western Immuno-Blot (WIB) was performed as described (Periasamy et al., 2013) using a crude serum of HvBot1 raised in rabbit (Nagarajan et al., Plant Cell, 2014, submitted) and detected using Novex® ECL HRP Chemi-Luminescent substrate Reagent Kit (Invitrogen, Carlsbad, CA, USA) according to manufacturer's protocol.

Results and Discussion

A tBLM-based on a DPhyTL monolayer was built in 100 mM NaCl as described in the Methods section. Before commencing EIS measurements with incorporated HvBot1, the lipid bilayer was tested for its stability in HEPES and HEPES-borate buffers at pH 7.5. As observed in Figure 2, the bilayer showed little sensitivity towards the presence of borate in the solution indicating that the bilayer was stable and could be used for *in situ* CF synthesis of HvBot1. The electrical properties in HEPES and HEPES-borate were almost identical (Table 1).

Table 1: Electrical properties of a tBLM before HvBot1 incorporation

Solution	**$R_{(sol)}$ (Ωcm^2)**	**$R_{(bilayer)}$ ($M\Omega cm^2$)**	**$C_{(bilayer)}$ ($\mu F.cm^2$)**	**$R_{(tether)}$ ($M\Omega cm^2$)**	**$C_{(tether)}$ ($\mu F.cm^2$)**	**$\alpha_{(tether)}$**
HEPES-Borate	2503±89.48	0.501±0.0630	0.342±0.0251	115±0.939	0.939±0.0544	0.968±0.00168
HEPES	2720±129.2	0.844±0.0148	0.371±0.040	82.3±0.0928	0.928±0.0801	0.956±0.00240

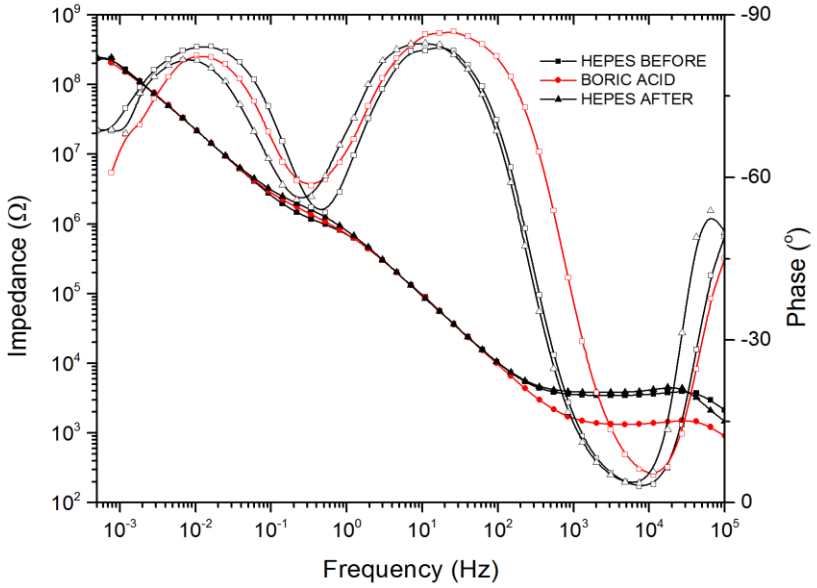

Figure 2. Bode plot of a DPhyTL bilayer in HEPES, HEPES-BA, and HEPES at 0 V potential; closed symbols show the impedance, open symbols are the phase shift, and solid lines direct the eye. The impedance between the two solutions changes insignificantly and in fact HEPES impedance only slightly increases between testing it before and after the measurements.

After confirming the stability of the bilayer, CF reaction of the HvBot1 protein was set up as described in the Methods section. Transport measurements by the HvBot1 transporter were performed sequentially as follows: the addition of the HEPES buffer was followed by the addition of the HEPES-BA buffer and then back to the HEPES buffer without BA. As observed in Figure 3, the membrane resistance decreased due to the addition of borate solution and the resistance went back to its starting value, when the BA solution was replaced by HEPES indicating that any change in resistance was due to transport of borate ions by HvBot1, while the membrane capacitance served as an indicator for membrane integrity. The bilayer resistance decreased from 7.54 MΩcm^2 to 0.562 MΩcm^2 (Table 2). At the same time, the membrane capacitance remained unchanged, indicating that the membrane itself still remained intact.

Table 2: Electrical properties of a tBLM containing HvBot1 incorporation

Solution	**$R_{(sol)}$ (Ωcm^2)**	**$R_{(bilayer)}$ ($M\Omega cm^2$)**	**$C_{(bilayer)}$ ($\mu F.cm^2$)**	**$R_{(tether)}$ ($M\Omega cm^2$)**	**$C_{(tether)}$ ($\mu F.cm^2$)**	**$\alpha_{(tether)}$**
HEPES	2725±92.398	7.54±0.980	0.420±0.0378	441±8.93	0.871±0.0769	0.950±0.0188
HEPES-Borate	2508±87.127	0.562±0.112	0.547±0.0735	418±9.96	0.820±0.0489	0.923±0.0170
HEPES	4743±82.34	9.76±0.725	0.445±0.0235	585±8.37	0.858±0.0445	0.947±0.108

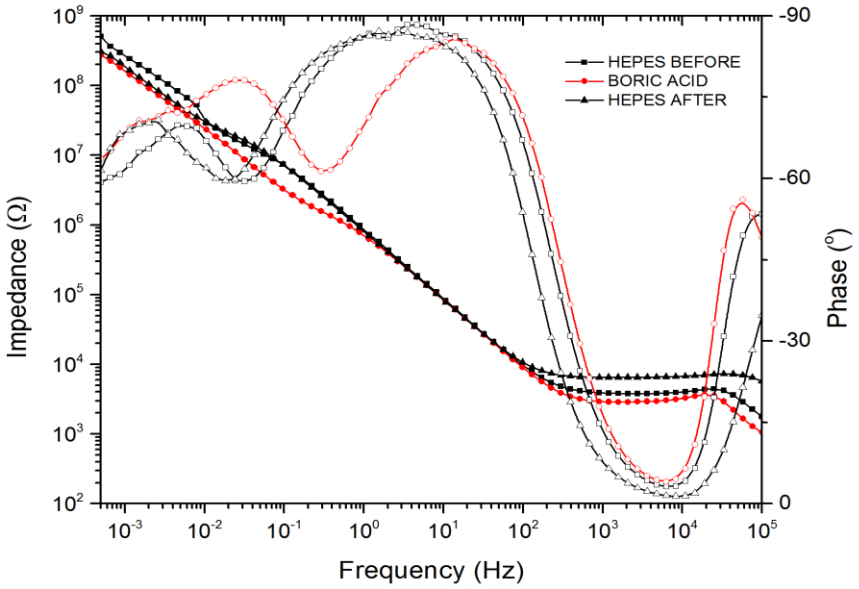

Figure 3. Bode plot of a DPhyTL bilayer after the inclusion of HvBot1 in HEPES, HEPES-BA, and HEPES at 0 V potential; closed symbols show the impedance, open symbols are the phase shift, and solid lines direct the eye. The HEPES buffer had high impedance as compared to the borate anion. Impedance was successfully recovered after re-introduction of the HEPES buffer.

After transport measurements were completed, the gold surface was stripped off with 10% (w/v) SDS to remove the lipid bilayer and the sample was subjected to WIB analysis as described in the Methods section. This was done to confirm that HvBot1 CF synthesis had occurred prior to measurements and that HvBot1 had been incorporated into the bilayer. Figure 4 shows the presence of HvBot1 that is observable as a protein band with molecular mass of approximately 65 kDa (lane 2). This protein was not observed in the control sample, not containing mRNA of HvBot1 during CF synthesis (lane 1).

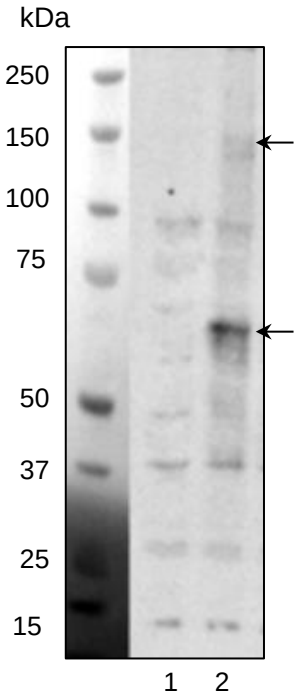

Figure 4. WIB of HvBot1 synthesised through WG-CFPS in an electroimpedance spectroscopy cell. Lane 1 and 2 represent translation reactions with no mRNA and with HvBot1 mRNA being added. Arrows represents monomeric and trimeric conformations of HvBot1. WIB was developed with a rabbit antibody raised against HvBot1 and the secondary antibody conjugated to HRP. The blots were detected using a Chemi-Luminescent substrate reagent. St. in kDa indicates molecular masses of proteins.

Conclusions

The presented data indicate the robustness of CF synthesis and serve as an example as to how nanotechnological methods can be applied effectively to answer biologically-relevant questions. The study has shown functional incorporation of HvBot1 into tBLM architecture and successful measurement of transport activity.

References

Periasamy, A., Shadiac, N., Amalraj, A., Garajová, S., Nagarajan, Y., Waters, S., Mertens, H.D.T., and Hrmova, M. (2013). Cell-free protein synthesis of membrane (1,3)-β-d-glucan (curdlan) synthase: Co-translational insertion in liposomes and reconstitution in nanodiscs. Biochimica et Biophysica Acta (BBA) - Biomembranes **1828,** 743-757.

Shadiac, N., Nagarajan, Y., Waters, S., and Hrmova, M. (2013). Close allies in membrane protein research: Cell-free synthesis and nanotechnology. Molecular Membrane Biology **0,** 1-17.

He, M. (2008). Cell-free protein synthesis: applications in proteomics and biotechnology. New Biotechnology **25,** 126-132.

Sutton, T., Baumann, U., Hayes, J., Collins, N.C., Shi, B.-J., Schnurbusch, T., Hay, A., Mayo, G., Pallotta, M., Tester, M., and Langridge, P. (2007). Boron-Toxicity Tolerance in Barley Arising from Efflux Transporter Amplification. Science **318,** 1446-1449.

Vockenroth, I.K., Ohm, C., Robertson, J.W.F., McGillivray, D.J., Loesche, M., and Koeper, I. (2008). Stable insulating tethered bilayer lipid membranes. Biointerphases **3,** FA68-FA73.

SIGNIFICANCE OF FINDINGS

This work explains a novel method to study membrane proteins in preformed bilayers. It opens the way for studying complicated membrane proteins by using CFS which was not possible before. This study also reflects the versatility of CFS and how it could be used in combination with other technologies.

General Discussion and Future Directions

Plants differ in their abilities to utilise BA and to tolerate excess BA. Physiological and molecular studies have confirmed that much of this variability can be explained by differences in uptake and distribution of BA in plants, which is primarily controlled by a group of membrane transporters. Both BA-deficiency and toxicity are major management issues in agriculture, and there is a need for in-depth investigation to understand how BA transport can be best manipulated to optimise crop production. Gaining a basic insight into the structure and function of borate transporters localised in cell plasma membranes would contribute significantly to our understanding how BA uptake and its distribution fits into the metabolic network of ion balance and homeostasis in plants.

The gene encoding a borate transporter in barley, designated *HvBot1*, was identified by Sutton and co-workers (2007). The authors found the increased copies of transcripts in the BA-tolerant barley variety Sahara 3771 (Sahara). High expression of this gene in the BA-tolerant barley variety (Sahara) compared to a sensitive variety (Clipper) resulted in the reduced amount of net borate ions being moved into the shoots from roots. Another gene *HvNIP2;1* identified in Sahara was found to be involved in the transport of neutral BA (Schnurbusch et al., 2010b). It was however found that under the high BA concentrations in soils there was reduced expression of this gene in tolerant varieties. Therefore the tolerance mechanism in Sahara was suggested to be mediated by a combination of reduced expression of HvNIP2;1 to limit BA uptake and high expression of HvBot1 to remove excess borate ions from roots (Schnurbusch et al., 2010a; Pallotta et al., 2014). Despite these findings, the exact molecular mechanisms underlying the transport of borate ions by HvBot1 have not been described so far.

The work presented here aimed to characterise the HvBot1 transport protein *in vitro* by applying a combination of techniques involving molecular biology, protein biochemistry and biophysics, nanotechnology and molecular modelling. Answers were sought to the following questions: What are the key transport properties that underlie transport of borate ions and what are the kinetic and mechanistic properties that are intrinsic to the function of HvBot1? For example, are there any caton-binding sites that are involved in the regulation of the transport process by HvBot1?

In the initial stages of this project, the expression of HvBot1 was investigated in a variety of heterologous hosts. Expression trials in *E.coli* and in the yeast *P. pastoris* led to low protein expression levels, which were not amenable for further biochemical and biophysical studies. Membrane proteins can be extremely challenging to work with as there are a number of significant bottlenecks associated with their production. These include determining an appropriate host for protein production, optimising expression levels and the further purification to obtain workable amounts of highly pure MP in the functional states (Bill et al., 2011; Shadiac et al., 2013). Therefore, in this study I have utilised a newly developed in-house CF system based on wheat germ (Periasamy et al., 2013) to synthesise HvBot1. This system has unique advantages over the cell-based expression systems, including easy manipulation of reaction conditions to favour protein folding, reduced sensitivity to cytotoxic products, suitability for high throughput strategies because of small reaction volumes and processing times, and a possibility of direct incorporation of proteins into membrane-mimicking environments such as micelles, bicelles, lipodiscs and liposomes (Shadiac et al., 2013).

The bacterial membrane enzyme curdlan synthase (CrdS) was used as a prototype protein to develop the techniques for production of MP through CF synthesis (Periasamy et al., 2013). The work of Periasamy et al. (2013) demonstrated co-translational incorporation of CrdS protein into artificial hydrophobic mimics, such as micelles, liposomes, bicelles and nanodiscs. A dialysis mode of CF reaction was also optimised to obtain high yields of MPs. One major advantage for our protein production approach was the ease of adding any synthetic or artificial hydrophobic mimics or environments directly into the translation reaction. After MP was reconstituted into liposomes during CF synthesis, the resultant nanoparticles could be purified through a single-purification step of density gradient ultra-centrifugation using Accudenz. After recovering highly purified proteo-liposomes with reconstituted MP, further functional and structural studies could be directly carried out.

Building on the results obtained from the CrdS study, I was able to define the most favourable environments for CF synthesis of HvBot1. The next step was to demonstrate that HvBot1 synthesised and directly incorporated into liposomes was functional. To perform these analyses, two different techniques were used. The first technique included a stopped-flow spectrophotometry assay using fluorescent Rayleigh scattering and a pH-sensitive dye biscarboxyfluorescein (BCECF). An increased fluorescent intensity was observed over time

due to an increase in pH caused by influx of borate ions into the proteo-liposomes, which was not seen in the control liposomes (no HvBot1 protein present), thus demonstrating that HvBot1 transported borate anions and thus was functional. Next, a voltage clamping technique was used by forming planar lipid bilayers to undertake detailed electrophysiological transport analyses, when single channel conductance of HvBot1 was measured in patched proteo-liposomes. Key findings of the patch clamping experiments were that HvBot1 exhibited channel-like characteristics and that HvBot1 transported predominantly borate anions, while also permeating a variety of anions such as chloride, sulphate, nitrate and phosphate at high concentrations. Michaelis-Menten kinetics showed tight affinity of HvBot1 for borate anions with a K_m of 104.1 ± 5.4 µM, which was consistent with a tight affinity observed for Bor1p from *S. cerevisiae* (Jennings et al., 2007). The transport of borate was also found to be Na^+-dependent as there was an increase in conductance observed with the increasing concentrations of Na^+ without a shift in reversal potential. This finding was in-line with the 3D quantum mechanical model of HvBot1, which identified a putative Na^+ binding site to be located on the intracellular protein region. This site included six amino acid residues participating in coordination of the Na^+ ion. This finding is of a significant importance as it demonstrates a potential link between BA toxicity and salinity. To this end, it is well-known those high concentrations of B in soils are typically associated with salinity in arid and semi-arid regions, and that often crops are exposed to both of these stresses simultaneously (Bennett, 2012).

To understand the biophysical properties of HvBot1, we performed SAXS and AFM measurements. Analysis of the SAXS data revealed a reduction of the thickness of lipid bilayer due to the incorporation of HvBot1, which was not observed in the control bilayers (no HvBot1 protein present). These data indicated that HvBot1 was incorporated in bilayers. Similar results have been obtained in a recent study of monomeric bacteriorhodopsin (Kynde et al., 2014). The AFM studies on the other hand showed consistent protrusion of HvBot1 by 1.7 nm (17 Å) above the lipid bilayer surface indicating that the protein has been inserted mostly unidirectionally in liposomes. Here, the hydrophobic membrane α-helical bundle was incorporated within the lipid bilayer and extra-membranous regions protruded above the bilayer surface with the N-terminus pointing to the surface of liposomes.

This study demonstrated that the CF synthesis system of MP production and the tools of nanotechnology represent an ideal amalgamation to study MP *in vitro*. Bridging the gap

between biology and nanotechnology to study biologically significant, yet complex MP, is of the utmost importance. Collaborative research between our laboratories with access to recent advancements in CF synthesis and nanotechnology has been important for the biochemical and biophysical study of a complex MP such as HvBot1. For example, tethered lipid bilayer membranes (tBLMs) have been excellent tools to study transport MPs, in particular ion channels and other transport proteins. MP incorporated in lipid bilayers that are directly supported on hydrophilic substrates suffer from non-physiological interactions with the solid support leading to a loss of protein dynamics and function. tBLMs circumvent this problem by separating the membrane from the MP-surface interactions and provide an additional space to allow for protein flexibility thus creating a more favourable environment. Until now, simpler model membrane systems, such as valinomycin or gramicidin have been used to study transport *via* EIS. In this work, the versatility of CF system was exploited and enabled optimisation of techniques for studying a real time permeation of borate by HvBot1; this technique can now be applied to study other ion channels. The formation of tBLM on the gold surface and *in situ* expression of HvBot1 on the bilayer represents a significant advancement in the field membrane transport in general and the knowledge acquired could be applicable not only to biology but also broader fields such as biosensor development (Ohno et al., 2013).

However, *in vitro* CF synthesis also has its limitations. These include the relatively short duration time of active protein synthesis and difficulties in re-supplying energy and substrates needed for protein synthesis without deleterious effects for chemical environments. With technical advancements in recent years some of these limitations have been addressed with the development of continuous or semi-continuous CF synthesis systems. These systems use ultrafiltration or dialysis membranes to supply energy and low-molecular mass substrates (such as NTP, amino acids, enzyme cofactors, *etc.*) continuously and also remove deleterious by-products of CF synthesis periodically during the course of synthesis (Klammt et al., 2007). With the CrdS enzyme, we reported a yield of up to 1-2 mg/ml using the modified CF synthesis system (Periasamy et al., 2013), which however has not lead to the same protein yields of HvBot1. We believe, that these protein yields are also achievable with the HvBot1 protein, however, the CF synthesis conditions and requirements would need to be significantly optimised.

Another challenge to understand the function of the HvBot1 transport protein lies in the availability of 3D structural information at the atomic level. Currently, this information is lacking for all transporters that are classified in the 2.A.31 Anion Exchanger (AE) family, together with the distant orthologs of mammalian and yeast carriers (Saier et al., 2014). A feasible approach to acquire the preliminary structural knowledge is to use *in silico* computational modelling, which allowed us to predict the overall structural fold of HvBot1 and its structural features that relate to the transport function, such as the presence of a Na^+-binding site. We discovered through *in silico* modelling the existence of a Na^+-binding site that we later confirmed *via* electrophysiological measurements. Last but not least, based on our *in silico* modelling, we could identify the presence of a specific structural region that we designated the 'sombrero' region. We predicted that this region might be involved in HvBot1 oligomerisation.

Future research should include studies of functionality of the predicted Na^+- binding site by site-directed mutagenesis to gain a general understanding of the role of Na^+-binding site in the gating mechanism of the HvBot1 channel. This study may also provide an insight as to how the presence of Na^+ ions may relate to boron toxicity. Another interesting research topic would be to investigate the role of post-translational modifications, such as phosphorylation, glycosylation, *etc.* of the HvBot1 channel activity through the supplementation of kinases or phosphatases during CF synthesis.

Obtaining a high-resolution 3D structure of HvBot1 would also provide clear insights into the mechanism of action of this borate transport protein. To achieve this goal, it will be feasible to explore the suitability of other heterologous expression systems such as the Baculovirus Expression Vector System. The Baculovirus system has been widely used for expressing eukaryotic membrane proteins, where one of the nonessential viral genes is replaced with the target protein through homologous recombination. The resulting recombinant baculovirus is used to infect cultured insect cells and the heterologous gene is expressed under the control of a strong promoter. To this end, plant transport proteins, which were not-functional in a traditional *X. laevis* oocytes system have been expressed and characterised through the Baculovirus system. Examples include various *A. thaliana* K^+ channel proteins namely, AKT1 (Gaymard et al., 1996; Urbach et al., 2000), KAT1 (Marten et al., 1996; Urbach et al., 2000) and KCO1 (Czempinski et al., 1997).

The primary aim of plant breeding is to improve yields of crops by identification and propagation of useful genotypic and phenotypic variants. Plants, by their intrinsic nature respond to environmental stresses and evolve tolerance mechanisms to sustain growth and reproduction under a variety of adverse environmental conditions. However, with a rapidly changing climate there is now not only a need to adopt conventional breeding techniques, but also to carry out more direct genetic manipulations to meet global challenges caused by temperature extremes, ion imbalance and water deficiency. Merging collaborative cross-disciplinary research involving plant molecular and cellular biology, protein biochemistry, biophysics, structural biology with breeding and agronomy has the potential to facilitate the development of the next generation crops through a generalised concept of "breeding by design" (Peleman and van der Voort, 2003). To envision this concept, it is of a paramount importance to gather knowledge regarding metabolic processes and transport mechanisms in plants and use this information to engineer crops that can thrive under current and future environmental scenarios.

References

Allen, G.J., Jones, R.G.W., and Leigh, R.A. (1995). Sodium-transport measured in plasma-membrane vesicles isolated from wheat genotypes with differing K^+/Na^+ discrimination traits. Plant Cell and Environment **18,** 105-115.

Barbier-Brygoo, H., Vinauger, M., Colcombet, J., Ephritikhine, G., Frachisse, J.M., and Maurel, C. (2000). Anion channels in higher plants: functional characterization, molecular structure and physiological role. Biochimica Et Biophysica Acta-Biomembranes **1465,** 199-218.

Bill, R.M., Henderson, P.J.F., Iwata, S., Kunji, E.R.S., Michel, H., Neutze, R., Newstead, S., Poolman, B., Tate, C.G., and Vogel, H. (2011). Overcoming barriers to membrane protein structure determination. Nature Biotechnology **29,** 335-340.

Blasergrill, J., Knoppik, D., Amberger, A., and Goldbach, H. (1989). Influence of boron on the membrane-potential in *Elodea-densa* and *Helianthus-annuus* roots and H^+ extrusion of suspension cultured *Daucus carota* cells. Plant Physiology **90,** 280-284.

Blumwald, E. (2000). Sodium transport and salt tolerance in plants. Current Opinion in Cell Biology **12,** 431-434.

Bonilla, I., Garciagonzalez, M., and Mateo, P. (1990). Boron requirement in cyanobacteria - its possible role in the early evolution of photosynthetic organisms. Plant Physiology **94,** 1554-1560.

Brennan, R.F., and Adcock, K.G. (2004). Incidence of boron toxicity in spring barley in Southwestern Australia. Journal of Plant Nutrition **27,** 411-425.

Briskin, D.P., Basu, S., and Assmann, S.M. (1995). Characterization of the red beet plasma-membrane H^+-ATPase reconstituted in a planar bilayer system. Plant Physiology **108,** 393-398.

Bustamante, J.O., Hanover, J.A., and Liepins, A. (1995). The ion-channel behavior of the nuclear-pore complex. Journal of Membrane Biology **146,** 239-251.

Camacho-Cristobal, J.J., and Gonzalez-Fontes, A. (1999). Boron deficiency causes a drastic decrease in nitrate content and nitrate reductase activity, and increases the content of carbohydrates in leaves from tobacco plants. Planta **209,** 528-536.

Camacho-Cristobal, J.J., and Gonzalez-Fontes, A. (2007). Boron deficiency decreases plasmalemma H^+-ATPase expression and nitrate uptake, and promotes ammonium assimilation into asparagine in tobacco roots. Planta **226,** 443-451.

Camacho-Cristobal, J.J., Maldonado, J.M., and Gonzalez-Fontes, A. (2005). Boron deficiency increases putrescine levels in tobacco plants. Journal of Plant Physiology **162,** 921-928.

Camacho-Cristobal, J.J., Lunar, L., Lafont, F., Baumert, A., and Gonzalez-Fontes, A. (2004). Boron deficiency causes accumulation of chlorogenic acid and caffeoyl polyamine conjugates in tobacco leaves. Journal of Plant Physiology **161,** 879-881.

Cannon, B., Hermansson, M., Gyorke, S., Somerharju, P., Virtanen, J.A., and Cheng, K.H. (2003). Regulation of calcium channel activity by lipid domain formation in planar lipid bilayers. Biophysical Journal **85,** 933-942.

Cartwright, B., Zarcinas, B., and Mayfield, A. (1984). Toxic concentrations of boron in a red-brown earth at Gladstone, South Australia. Soil Research **22,** 261-272.

Chiba, Y., Mitani, N., Yamaji, N., and Ma, J.F. (2009). HvLsi1 is a silicon influx transporter in barley. The Plant Journal **57,** 810-818.

Chu, B.S., Dopico, A.M., Lemos, J.R., and Treistman, S.N. (1998). Ethanol potentiation of calcium-activated potassium channels reconstituted into planar lipid bilayers. Molecular Pharmacology **54,** 397-406.

Czempinski, K., Zimmermann, S., Ehrhardt, T., and MullerRober, B. (1997). New structure and function in plant K+ channels: KCO1, an outward rectifier with a steep $Ca2^{+}$ dependency. Embo Journal **16,** 2565-2575.

Dannel, F., Pfeffer, H., and Romheld, V. (2000). Characterization of root boron pools, boron uptake and boron translocation in sunflower using the stable isotopes B-10 and B-11. Australian Journal of Plant Physiology **27,** 397-405.

Dannel, F., Pfeffer, H., and Romheld, V. (2002). Update on boron in higher plants - Uptake, primary translocation and compartmentation. Plant Biology **4,** 193-204.

Dean, John A. (1979) Lange's Handbook of Chemistry, 12th ed.; McGraw-Hill Book Company: New York, NY,p 9:4-9:94

Dordas, C., and Brown, P.H. (2001). Evidence for channel mediated transport of boric acid in squash (*Cucurbita pepo*). Plant and Soil **235,** 95-103.

Dordas, C., Chrispeels, M.J., and Brown, P.H. (2000). Permeability and channel-mediated transport of boric acid across membrane vesicles isolated from squash roots. Plant Physiology **124,** 1349-1361.

Dutzler, R., Campbell, E.B., Cadene, M., Chait, B.T., and MacKinnon, R. (2002). X-ray structure of a CIC chloride channel at 3.0 angstrom reveals the molecular basis of anion selectivity. Nature **415,** 287-294.

Farrokhi, N., Hrmova, M., Burton, R.A., and Fincher, G.B. (2009). Heterologous and Cell-free protein expression systems. In Plant Genomics, J.P. Gustafson, P. Langridge, and D.J. Somers, eds (Humana Press), pp. 175-198.

Gassmann, O., Kreir, M., Ambrosi, C., Pranskevich, J., Oshima, A., Roeling, C., Sosinsky, G., Fertig, N., and Steinem, C. (2009). The M34A mutant of Connexin26 reveals active conductance states in pore-suspending membranes. Journal of Structural Biology **168,** 168-176.

Gaymard, F., Cerutti, M., Horeau, C., Lemaillet, G., Urbach, S., Ravallec, M., Devauchelle, G., Sentenac, H., and Thibaud, J.B. (1996). The baculovirus/insect cell system as an alternative to *Xenopus* oocytes - First characterization of the AKT1 K^+ channel from Arabidopsis thaliana. Journal of Biological Chemistry **271,** 22863-22870.

Goldbach, H.E., and Wimmer, M.A. (2007). Boron in plants and animals: Is there a role beyond cell-wall structure? Journal of Plant Nutrition and Soil Science-Zeitschrift Fur Pflanzenernahrung Und Bodenkunde **170,** 39-48.

Hayes, J.E., and Reid, R.J. (2004). Boron tolerance in barley is mediated by efflux of boron from the roots. Plant Physiology **136,** 3376-3382.

Hayes, J.E., Pallotta, M., Baumann, U., Berger, B., Langridge, P., and Sutton, T. (2013). Germanium as a tool to dissect boron toxicity effects in barley and wheat. Functional Plant Biology**, 345,** 234-240.

He, M. (2008). Cell-free protein synthesis: applications in proteomics and biotechnology. New Biotechnology **25,** 126-132.

Hovijitra, N.T., Wuu, J.J., Peaker, B., and Swartz, J.R. (2009). Cell-free synthesis of functional aquaporin Z in synthetic liposomes. Biotechnology and Bioengineering **104,** 40-49.

Hrmova, M., and Fincher, G.B. (2009). Functional genomics and structural biology in the definition of gene function. In Plant Genomics, J.P. Gustafson, P. Langridge, and D.J. Somers, eds (Humana Press), pp. 199-227.

Huang, J.W.W., Grunes, D.L., and Kochian, L.V. (1994). Voltage-dependent ca2+ influx into right-side-out plasma-membrane vesicles isolated from wheat roots - characterization of a putative Ca^{2+} channel. Proceedings of the National Academy of Sciences of the United States of America **91,** 3473-3477.

Jefferies, S.P., Barr, A.R., Karakousis, A., Kretschmer, J.M., Manning, S., Chalmers, K.J., Nelson, J.C., Islam, A.K.M.R., and Langridge, P. (1999). Mapping of chromosome regions conferring boron toxicity tolerance in barley (*Hordeum vulgare L.*). Theoretical and Applied Genetics **98,** 1293-1303.

Jennings, M.L., Howren, T.R., Cui, J., Winters, M., and Hannigan, R. (2007). Transport and regulatory characteristics of the yeast bicarbonate transporter homolog Bor1p. American Journal of Physiology-Cell Physiology **293,** C468-C476.

Junge, F., Haberstock, S., Roos, C., Stefer, S., Proverbio, D., Doetsch, V., and Bernhard, F. (2011). Advances in cell-free protein synthesis for the functional and structural analysis of membrane proteins. New Biotechnology **28,** 262-271.

Katzen, F., Fletcher, J.E., Yang, J.-P., Kang, D., Peterson, T.C., Cappuccio, J.A., Blanchette, C.D., Sulchek, T., Chromy, B.A., Hoeprich, P.D., Coleman, M.A., and Kudlicki, W. (2008). Insertion of membrane proteins into discoidal membranes using a cell-free protein expression Approach. Journal of Proteome Research **7,** 3535-3542.

Klammt, C., Schwarz, D., Dötsch, V., and Bernhard, F. (2007). Cell-Free Production of Integral Membrane Proteins on a Preparative Scale. In In Vitro Transcription and Translation Protocols, G. Grandi, ed (Humana Press), pp. 57-78.

Kreir, M., Farre, C., Beckler, M., George, M., and Fertig, N. (2008). Rapid screening of membrane protein activity: electrophysiological analysis of OmpF reconstituted in proteoliposomes. Lab on a Chip **8,** 587-595.

Kumar, K., Mosa, K., Chhikara, S., Musante, C., White, J., and Dhankher, O. (2014). Two rice plasma membrane intrinsic proteins, OsPIP2;4 and OsPIP2;7, are involved in transport and providing tolerance to boron toxicity. Planta **239**, 187-198.

Kynde, S.A.R., Skar-Gislinge, N., Pedersen, M.C., Midtgaard, S.R., Simonsen, J.B., Schweins, R., Mortensen, K., and Arleth, L. (2014). Small-angle scattering gives direct structural information about a membrane protein inside a lipid environment. Acta Crystallographica Section D-Biological Crystallography **70,** 371-383.

Loomis, W.D., and Durst, R.W. (1992). Chemistry and biology of boron. BioFactors **3,** 229-239.

Marten, I., Gaymard, F., Lemaillet, G., Thibaud, J.B., Sentenac, H., and Hedrich, R. (1996). Functional expression of the plant K+ channel KAT1 in insect cells. FEBS Letters **380,** 229-232.

Meyer, S., Mumm, P., Imes, D., Endler, A., Weder, B., Al-Rasheid, K.A.S., Geiger, D., Marten, I., Martinoia, E., and Hedrich, R. (2010). AtALMT12 represents an R-type anion channel required for stomatal movement in Arabidopsis guard cells. Plant Journal **63,** 1054-1062.

Miwa, K., Takano, J., and Fujiwara, T. (2005). Roles of BOR1 paralogs in boron transport in *Arabidopsis thaliana*. In: Li CJ (ed) Plant nutrition for food security, human health and environmental protection. Tsinghua University Press, Beijing, pp 124–125.

Miwa, K., Takano, J., Omori, H., Seki, M., Shinozaki, K., and Fujiwara, T. (2007). Plants tolerant of high boron levels. Science **318**, 1417.

Miwa, K., and Fujiwara, T. (2010). Boron transport in plants: co-ordinated regulation of transporters. Annals of Botany **105,** 1103-1108.

Miwa, K., Wakuta, S., Takada, S., Ide, K., Takano, J., Naito, S., Omori, H., Matsunaga, T., and Fujiwara, T. (2013**).** Roles of BOR2, a boron exporter, in cross linking of Rhamnogalacturonan II and root elongation under boron limitation in *Arabidopsis*. Plant Physiology **163**, 1699-1709.

Moody, D.B., Rathjen, A.J., and Cartwright, B. (1993). Yield evaluation of a gene for boron tolerance using backcross-derived lines. Genetic Aspects of Plant Mineral Nutrition **97,** 363-366

Nable, R., Bañuelos, G., and Paull, J. (1997). Boron toxicity. Plant and Soil **193,** 181-198.

Nakagawa, Y., Hanaoka, H., Kobayashi, M., Miyoshi, K., Miwa, K., and Fujiwara, T. (2007). Cell-type specificity of the expression of OsBOR1, a rice efflux boron transporter gene, is regulated in response to boron availability for efficient boron uptake and xylem loading. Plant Cell **19**, 2624-2635.

Neher, E., and Sakmann, B. (1976). Single channel currents recorded from membrane of denervated frog muscle fibres. Nature **260**, 799-802.

Nielsen, F.H. (2000). The emergence of boron as nutritionally important throughout the life cycle. Nutrition **16,** 512-514.

Nozawa, A., Takano, J., Kobayashi, M., von Wiren, N., and Fujiwara, T. (2006). Roles of BOR1, DUR3, and FPS1 in boron transport and tolerance in *Saccharomyces cerevisiae*. FEMS Microbiology Letters **262,** 216-222.

Ohno, R., Ohnuki, H., Wang, H., Yokoyama, T., Endo, H., Tsuya, D., and Izumi, M. (2013). Electrochemical impedance spectroscopy biosensor with interdigitated electrode for detection of human immunoglobulin A. Biosensors & Bioelectronics **40,** 422-426.

Pallotta, M., Schnurbusch, T., Hayes, J., Hay, A., Baumann, U., Paull, J., Langridge, P., and Sutton, T. (2014). Molecular basis of adaptation to high soil boron in wheat landraces and elite cultivars. Nature **514,** 88-91.

Park, M., Li, Q., Shcheynikov, N., Zeng, W.Z., and Muallem, S. (2004). NaBC1 is a ubiquitous electrogenic Na^+-coupled borate transporter essential for cellular boron homeostasis and cell growth and proliferation. Molecular Cell **16,** 331-341.

Peleman, J.D., and van der Voort, J.R. (2003). Breeding by design. Trends in Plant Science **8,** 330-334.

Pang, Y., Li, L., Ren, F., Lu, P., Wei, P., Cai, J., Xin, L., Zhang, J., Chen, J., and Wang, X. (2010). Overexpression of the tonoplast aquaporin AtTIP5;1 conferred tolerance to boron toxicity in Arabidopsis. Journal of Genetics and Genomics **37**, 389–397.

Periasamy, A., Shadiac, N., Amalraj, A., Garajová, S., Nagarajan, Y., Waters, S., Mertens, H.D.T., and Hrmova, M. (2013). Cell-free protein synthesis of membrane (1,3)-β-d-glucan (curdlan) synthase: Co-translational insertion in liposomes and reconstitution in nanodiscs. Biochimica et Biophysica Acta (BBA) - Biomembranes **1828,** 743-757.

Power, P.P., and Woods, W.G. (1997). The chemistry of boron and its speciation in plants. Plant and Soil **193,** 1-13.

Raven, J.A. (1980). Short-distance and long-distance transport of boric-acid in plants. New Phytologist **84,** 231-249.

Reid, R. (2007). Identification of boron transporter genes likely to be responsible for tolerance to boron toxicity in wheat and barley. Plant and Cell Physiology **48,** 1673-1678.

Reid, R., and Fitzpatrick, K. (2009). Influence of leaf tolerance mechanisms and rain on boron toxicity in barley and wheat. Plant Physiology **151,** 413-420.

Roberts, S.K. (2006). Plasma membrane anion channels in higher plants and their putative functions in roots. New Phytologist **169,** 647-666.

Roessner, U., Patterson, J.H., Forbes, M.G., Fincher, G.B., Langridge, P., and Bacic, A. (2006). An Investigation of boron toxicity in barley using metabolomics. Plant Physiology **142,** 1087-1101.

Sawasaki, T., Ogasawara, T., Morishita, R., and Endo, Y. (2002). A cell-free protein synthesis system for high-throughput proteomics. Proceedings of the National Academy of Sciences of the United States of America **99,** 14652-14657.

Schnurbusch, T., Collins, N., Eastwood, R., Sutton, T., Jefferies, S., and Langridge, P. (2007). Fine mapping and targeted SNP survey using rice-wheat gene colinearity in the region of the *Bo1* boron toxicity tolerance locus of bread wheat. Theoretical and Applied Genetics **115,** 451-461.

Schnurbusch, T., Hayes, J., and Sutton, T. (2010a). Boron toxicity tolerance in wheat and barley: Australian perspectives. Breeding Science **60,** 297-304.

Schnurbusch, T., Hayes, J., Hrmova, M., Baumann, U., Ramesh, S.A., Tyerman, S.D., Langridge, P., and Sutton, T. (2010b). Boron Toxicity Tolerance in Barley through Reduced Expression of the Multifunctional Aquaporin HvNIP2;1. Plant Physiology 153, 1706-1715.

Schroeder, J.I., and Keller, B.U. (1992). 2 types of anion channel currents in guard-cells with distinct voltage regulation. Proceedings of the National Academy of Sciences of the United States of America **89,** 5025-5029.

Schwarz, D., Dötsch, V., and Bernhard, F. (2008). Production of membrane proteins using cell-free expression systems. Proteomics **8,** 3933-3946.

Shadiac, N., Nagarajan, Y., Waters, S., and Hrmova, M. (2013). Close allies in membrane protein research: Cell-free synthesis and nanotechnology. Molecular Membrane Biology **0,** 1-17.

Sutton, T., Baumann, U., Hayes, J., Collins, N.C., Shi, B.-J., Schnurbusch, T., Hay, A., Mayo, G., Pallotta, M., Tester, M., and Langridge, P. (2007). Boron-toxicity tolerance in barley arising from efflux transporter amplification. Science **318,** 1446-1449.

Takano, J., Noguchi, K., Yasumori, M., Kobayashi, M., Gajdos, Z., Miwa, K., Hayashi, H., Yoneyama, T., and Fujiwara, T. (2002). *Arabidopsis* boron transporter for xylem loading. Nature **420**, 337-340.

Takano, J., Kobayashi, M., Noda, Y., and Fujiwara, T. (2007). *Saccharomyces cerevisiae* Bor1p is a boron exporter and a key determinant of boron tolerance. FEMS Microbiology Letters **267,** 230-235.

Takano, J., Wada, M., Ludewig, U., Schaaf, G., von Wirén, N., and Fujiwara, T. (2006). The *Arabidopsis* major intrinsic protein nip5;1 is essential for efficient boron uptake and plant development under boron limitation. The Plant Cell Online **18,** 1498-1509.

Tanaka, M., Wallace, I.S., Takano, J., Roberts D.M., and Fujiwara, T. (2008). NIP6;1 is a boric acid channel for preferential transport of boron to growing shoot tissues in *Arabidopsis*. Plant Cell **20**, 2860-2875.

Tanaka, N., Uraguchi, S., Saito, A., Kajikawa, M., Kasai, K., Sato, Y., Nagamura, Y., and Fujiwara, T. (2013). Roles of pollen-specific boron efflux transporter, OsBOR4, in the rice fertilization process. Plant Cell Physiology **54**, 2011-2019.

Tyerman, S.D., Skerrett, M., Garrill, A., Findlay, G.P., and Leigh, R.A. (1997). Pathways for the permeation of Na^+ and Cl^- into protoplasts derived from the cortex of wheat roots. Journal of Experimental Botany **48,** 459-480.

Urbach, S., Cherel, I., Sentenac, H., and Gaymard, F. (2000). Biochemical characterization of the *Arabidopsis* K^+ channels KAT1 and AKT1 expressed or co-expressed in insect cells. Plant Journal **23,** 527-538.

Vockenroth, I.K., Ohm, C., Robertson, J.W.F., McGillivray, D.J., Loesche, M., and Koeper, I. (2008). Stable insulating tethered bilayer lipid membranes. Biointerphases **3,** 68-73.

Warington, K. (1923). The effect of boric acid and borax on the broad bean and certain other plants. Annals of Botany **37,** 629-623.

White, P.J., and Ridout, M. (1995). The K^+ channel in the plasma-membrane of rye roots has a multiple ion residency pore. Journal of Membrane Biology **143,** 37-49.

Whittaker, J.W. (2013). Cell-free protein synthesis: the state of the art. Biotechnology Letters **35,** 143-152.

Yu, Q., Wingender, R., Schulz, M., Baluska, F., and Goldbach, H.E. (2001). Short-term boron deprivation induces increased levels of cytoskeletal proteins in *Arabidopsis* roots. Plant Biology **3,** 335-340.

Yu, Q., Hlavacka, A., Matoh, T., Volkmann, D., Menzel, D., Goldbach, H.E., and Baluska, F. (2002). Short-term boron deprivation inhibits endocytosis of cell wall pectins in meristematic cells of maize and wheat root apices. Plant Physiology **130,** 415-421.

Zhao, R.M., and Reithmeier, R.A.F. (2001). Expression and characterization of the anion transporter homologue YNL275w in *Saccharomyces cerevisiae*. American Journal of Physiology-Cell Physiology **281,** 33-45.